



**HAL**  
open science

# SiGe photonic integrated circuits for mid-infrared sensing applications

Qiankun Liu

► **To cite this version:**

Qiankun Liu. SiGe photonic integrated circuits for mid-infrared sensing applications. Optics [physics.optics]. Université Paris Saclay (COmUE), 2019. English. NNT : 2019SACLS166 . tel-02194433

**HAL Id: tel-02194433**

**<https://theses.hal.science/tel-02194433>**

Submitted on 25 Jul 2019

**HAL** is a multi-disciplinary open access archive for the deposit and dissemination of scientific research documents, whether they are published or not. The documents may come from teaching and research institutions in France or abroad, or from public or private research centers.

L'archive ouverte pluridisciplinaire **HAL**, est destinée au dépôt et à la diffusion de documents scientifiques de niveau recherche, publiés ou non, émanant des établissements d'enseignement et de recherche français ou étrangers, des laboratoires publics ou privés.

# SiGe photonic integrated circuits for mid-infrared sensing applications

Thèse de doctorat de l'Université Paris-Saclay  
préparée à l'Université Paris-Sud

École doctorale n°575 electrical, optical bio: physics and engineering  
(EOBE)  
Spécialité de doctorat: Physique

Thèse présentée et soutenue à Palaiseau, le 16 Juillet 2019, par

**Qiankun Liu**

Composition du Jury :

Günther Roelkens Professeur, Ghent University	Rapporteur
Roland Teissier Directeur de recherches, CNRS (IES)	Rapporteur
Maria Tchernycheva Directeur de recherches, CNRS (C2N)	Président
Sergio Nicoletti Ingénieur, CEA Leti	Examineur
Joan Manel Ramirez Ingénieur, III-V Lab	Examineur
Delphine Marris-Morini Professeur, Université Paris Sud (C2N)	Directrice de thèse



**Titre :** Circuits photoniques intégrés SiGe pour des applications capteurs dans le moyen-infrarouge

**Mots clés :** Photonique silicium, Moyen-infrarouge, SiGe, Capteurs optiques intégrés

**Résumé :** La spectroscopie dans le moyen-infrarouge est une méthode universelle pour identifier les substances chimiques et biologiques, car la plupart des molécules ont leurs résonances de vibration et de rotation dans cette plage de longueurs d'onde. Les systèmes moyen infrarouge disponibles dans le commerce reposent sur des équipements volumineux et coûteux, tandis que de nombreux efforts sont maintenant consacrés à la réduction de leur taille et leur intégration sur circuits intégrés. L'utilisation de la technologie silicium pour la réalisation de circuits photoniques dans le moyen-infrarouge présente de nombreux avantages: fabrication fiable, à grand volume, et réalisation de circuits photoniques à hautes performances, compacts, légers et à faible consommation énergétique. Ces avantages sont particulièrement intéressants pour les systèmes de détection spectroscopique moyen infrarouge, qui besoin d'être portable et à faible coût. Parmi les différents matériaux disponibles en photonique silicium, les alliages silicium-germanium (SiGe) à forte concentration en Ge sont particulièrement intéressants en raison de la grande fenêtre de transparence du Ge, pouvant atteindre 15  $\mu\text{m}$ .

Dans ce contexte, l'objectif de cette thèse est d'étudier une nouvelle plate-forme SiGe à forte concentration en Ge, pour la démonstration de circuits photoniques moyen infra rouge. Cette nouvelle plate-forme devrait bénéficier d'une large gamme de transparence en longueurs d'onde de transparence et de la possibilité d'ajuster les propriétés des guides optiques (indice effectif, dispersion,...).

Au cours de cette thèse, différentes plates-formes basées sur différents profils graduels du guide d'onde ont été étudiées. Tout d'abord, il a été démontré qu'il était possible d'obtenir des guides présentant de faibles pertes optiques inférieures à 3 dB/cm dans une large plage de longueurs d'onde, de 5,5 à 8,5  $\mu\text{m}$ . Une preuve de concept de détection de molécules, basée sur l'absorption de la partie évanescent du mode optique a ensuite été démontrée. Ensuite, les composants formant les briques de base classiques de la photonique intégrée ont été étudiés. Les premières cavités intégrées ont été réalisées à 8  $\mu\text{m}$ . Deux configurations ont été étudiées : des cavités Fabry-Perot utilisant des miroirs de Bragg intégrés dans les guides d'onde et des résonateurs en anneau. Un spectromètre à transformée de Fourier fonctionnant sur une large bande spectrale, et pour les deux polarisations de la lumière a également été démontré. Tous ces résultats reposent sur la conception des matériaux et des composants, la fabrication en salle blanche et la caractérisation expérimentale. Ce travail a été effectué dans le cadre du projet européen INSPIRE en collaboration avec le Pr. Giovanni Isella de Politecnico Di Milano.



**Title :** SiGe photonic integrated circuits for mid-infrared sensing applications

**Keywords:** Silicon Photonics, Mid-infrared, SiGe, integrated optical sensors

**Abstract:** Mid-infrared (mid-IR) spectroscopy is a nearly universal way to identify chemical and biological substances, as most of the molecules have their vibrational and rotational resonances in the mid-IR wavelength range. Commercially available mid-IR systems are based on bulky and expensive equipment, while lots of efforts are now devoted to the reduction of their size down to chip-scale dimensions. The use of silicon photonics for the demonstration of mid-IR photonic circuits will benefit from reliable and high-volume fabrication to offer high performance, low cost, compact, lightweight and power consumption photonic circuits, which is particularly interesting for mid-IR spectroscopic sensing systems that need to be portable and low cost. Among the different materials available in silicon photonics, Germanium (Ge) and Silicon-Germanium (SiGe) alloys with a high Ge concentration are particularly interesting because of the wide transparency window of Ge up to 15  $\mu\text{m}$ .

In this context, the objective of this thesis is to investigate a new Ge-rich graded SiGe platform for mid-IR photonic circuits. Such new platform was expected to benefit from a wide transparency wavelength range and a high versatility in terms of optical engineering (effective index, dispersion, ...).

During this thesis, different waveguides platforms based on different graded profiles have been investigated. First it has been shown that waveguides with low optical losses of less than 3 dB/cm can be obtained in a wide wavelength range, from 5.5 to 8.5  $\mu\text{m}$ . A proof of concept of sensing based on the absorption of the evanescent component of the optical mode has then been demonstrated. Finally, elementary building blocs have been investigated. The first Bragg mirror-based Fabry Perot cavities and racetrack resonators have been demonstrated around 8  $\mu\text{m}$  wavelength. A broadband dual-polarization MIR integrated spatial heterodyne Fourier-Transform spectrometer has also been obtained. All these results rely on material and device design, clean-room fabrication and experimental characterization. This work was done in the Framework of EU project INsPIRE in collaboration with Pr. Giovanni Isella from Politecnico Di Milano.

## Acknowledgements

The work of this thesis is realized in the Centre de Nanosciences et de Nanotechnologies (C2N), in the research group of Silicon Photonics (MINAPHOT). The last 3 years of this thesis is a truly memorable experience for me and clearly it will not be feasible without supports from a lot of people.

First and foremost, I would like to express my deep gratitude to my PhD supervisor Prof. Delphine Marris-Morini for the fascinating scientific journey she took me on. I am eternally grateful for all that she brought me during my thesis but also during my master. From simulations to publications, I am truly appreciate all advices and guidance and also tremendous scientific and technological knowledge that she shared with me. She has been extremely supportive beyond scientific research, also on other issues that I faced as an international student in France. It contributes significantly to the progress of my work and life.

During 3 years working in the European project INsPIRE, I worked a lot with Dr. Joan Manel Ramirez, Dr. Vladyslav Vakarin and Miguel Montesinos Ballester, postdoctoral, previous and current doctoral student in our group. Joan has been like a big brother, with patience and knowledge to help me out. I thank Joan a lot for spending hours on the device characterization and for building a free-space mid-infrared experimental set-up that works so well. I also thank Vladyslav for his help on device simulation and fabrication. He guided me into the world of nanofabrication. Miguel is an active PhD student working in the INsPIRE project since end of 2018. He always aim to do his work effectively and has new ideas. It's my pleasure to work with them.

Concerning device fabrication, I would like to thank the nanotechnology specialist in our team, Xavier Le Roux. The device fabrication is a complex task and main challenge of my PhD work, which requires a significant investment in the development of new technological processes. With tight collaboration, his advice and expertise allowed me to improve and develop the nanofabrication process for our SiGe devices in order to properly fabricate the designed samples.

It's my honor to have the opportunity to work with Dr. Laurent Vivien, Prof. Eric Cassan, Dr. Carlos Alonso Ramos and Dr. Daniel Benedikovic. I appreciate the fruitful discussion for the issues on device simulation and characterization. I would like to thank Eric for his help in handling the connection between my computer and clusters for simulation, and also for his help on all administrative issues. I also want to specially thank Carlos and Daniel for the invaluable discussion on theoretical modeling of periodic waveguide structures, and Fourier Transform spectroscopy. In particular, besides of the scientific research, I thank a lot Carlos to help me on the preparation of presentation and traveling for international conferences.

This thesis would not be possible without the in-depth work on the growth of epitaxial materials. I thus want to thank Prof. Giovanni Isella, Dr. Jacopo Frigerio and Dr. Andrea Ballabio from L-NESS, Politecnico Di Milano. They are clearly the fundamental persons of graded-index SiGe materials. All the epitaxial materials leading to the results in this thesis were grown by Giovanni, Jacopo and Andrea. I also want to thank them for the invaluable discussion and comments for publications.

I am thankful to several engineers for their patience and kind help in the cleanroom. I like to thank David Bouville for helping me to dice the devices with high quality and reliable facets. I also like to thank Jean-Ren éCoudevylle for all the training on cleanroom equipment and kind suggestion on ebeam lithography. I would like thank Etienne Hertz for spending hours with me to develop the deep-etch process of the SiGe devices. I would never forget the feeling that the first time I observed a smooth deep etched facet in front of SEM. I would also like to thank Fabien Bayle for the training and kind help on SEM observation.

I would like to acknowledge every PhD student and Postdoctoral researcher at our Silicon Photonic team, I am happy to be a MINAPHOTers. Firstly, I am glad to share the office with Joan Manel Ramirez, Carlos Alonso-Ramos, Thi Hong Cam Hoang, Thi-Phuong Do and Daniel Benedikovic. Cam was already a PhD student when I firstly joined the group as an internship student in 2016. Her research passion is admirable to me, and motivates me to keep doing my jobs well. Elena Dur án Valdeiglesias is a very friendly and energetic person, she is always willing to help us for any issues, scientific or daily life. Weiwei Zhang and Jianhao Zhang are always very kind for discussion with their wealth of knowledge on

integrated resonant structures. It is my pleasure to be friend with every current PhD student at Silicon Photonics team: Dorian Oser, Alicia Ruiz Caridad, Christian Lafforgue, Lucas Deniel, Dinh Thi Thuy Duong and Zhengrui Tu. Dorian and I began the PhD at almost the same time, so we had a lot of scientific and non-scientific discussions. I am happy and grateful to have had the opportunity to work with previous doctoral researchers in the team: Samuel Serna Otávaro, Guillaume Marcaud, Mathias Berciano, Pedro Damas, Diego Perez-Galacho, Papichaya Chaisakul.

I also want to thank my friends: Ngoc-Linh Tran, Sokhna M'ry Ngom, Duan Jianan, Xin Cui, Yulong Fan, Nan Guan, Hongyue Wang and Cheng Zhang, for their support and all the good moment we had together.

Finally, I deeply appreciate the constant helps and supports from my parents, Guijiao Jin and Chunhong Liu. Their constant selfless support gave me enough strength to accomplish this thesis. I am truly grateful to my girlfriend, Jadis Yi, for her loving support and patience despite the long distance between us. She always tries to understand me and helps me with her working experience and tremendous knowledge in English. There is no way to translate into words my appreciation and thankfulness.

## Résumé en Français

La spectroscopie dans le moyen-infrarouge (MIR) est une méthode universelle pour identifier les substances chimiques et biologiques. Les systèmes moyen infrarouge disponibles dans le commerce reposent sur des équipements volumineux et coûteux, tandis que de nombreux efforts sont maintenant consacrés à la réduction de leur taille et leur intégration sur circuits intégrés. L'utilisation de la technologie silicium pour la réalisation de circuits photoniques dans le moyen-infrarouge présente de nombreux avantages : fabrication fiable, à grand volume, et réalisation de circuits photoniques à hautes performances, compacts, légers et à faible consommation énergétique. Ces avantages sont particulièrement intéressants pour les systèmes de détection spectroscopique moyen infrarouge, qui ont besoin d'être portables et à faible coût.

La région spectrale du MIR est définie typiquement pour des longueurs d'onde allant de 2 à 20  $\mu\text{m}$  (500 à 5000  $\text{cm}^{-1}$  en nombre d'onde). Dans cette zone se situe la "fingerprint région", de 6.6 à 20  $\mu\text{m}$ , où se situent les résonances vibrationnelles et rotationnelles fondamentales de la plupart des espèces chimiques, comme représenté sur la figure 1. Ces résonances créent des lignes d'absorption uniques, véritables signatures des différentes molécules. Un capteur basé sur la détection de ces lignes d'absorption présente ainsi une très grande sélectivité, par rapport à un capteur fonctionnant dans d'autres gammes de longueurs d'onde, où une fonctionnalisation de surface ou une identification complémentaire est typiquement requise.

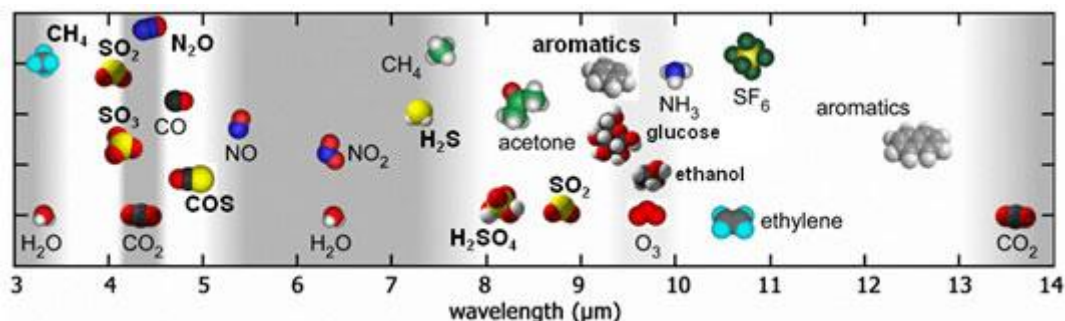


Fig.1. Illustration des raies d'absorption dans le moyen infra-rouge des différentes molécules, issu de [http://www.daylightsolutions.com.]

Parmi les différents matériaux disponibles en photonique silicium, le Germanium (Ge) et les alliages silicium-germanium (SiGe) à forte concentration en Ge sont particulièrement intéressants en raison de la grande fenêtre de transparence du Ge, pouvant atteindre 15  $\mu\text{m}$ .

Dans ce contexte, l'objectif de cette thèse est d'étudier une nouvelle plate-forme SiGe à forte concentration en Ge, pour la démonstration de circuits photoniques MIR. Cette nouvelle plate-forme devrait bénéficier d'une large gamme de transparence en longueurs d'onde de transparence et de la possibilité d'ajuster les propriétés des guides optiques (indice effectif, dispersion,...). Au cours de cette thèse, différentes plates-formes basées sur différents profils graduels du guide d'onde ont été étudiées. Tout d'abord, il a été démontré qu'il était possible d'obtenir des guides présentant de faibles pertes optiques d'environ 2 dB / cm dans une large plage de longueurs d'onde, de 5,5 à 8,5  $\mu\text{m}$ . Une preuve de concept de détection de molécules, basée sur l'absorption de la partie évanescent du mode optique a ensuite été démontrée. Ensuite, les composants formant les briques de base classiques de la photonique intégrée ont été étudiés. Les premières cavités intégrées ont été réalisées à 8  $\mu\text{m}$ . Deux configurations ont été étudiées : des cavités Fabry-Perot utilisant des miroirs de Bragg intégrés dans les guides d'onde et des résonateurs en anneau. Un spectromètre à transformée de Fourier fonctionnant sur une large bande spectrale, et pour les deux polarisations de la lumière a également été démontré. Tous ces résultats reposent sur la conception des matériaux et des composants, la fabrication en salle blanche et la caractérisation expérimentale. Ce travail a été effectué dans le cadre du projet européen INSPIRE en collaboration avec le Pr. Giovanni Isella de Politecnico Di Milano.

La croissance des structures graduelles SiGe est réalisée par Low-Energy Plasma Enhanced Chemical Vapor Deposition (LEPECVD) au laboratoire L-Ness /Politecnico Di Milano. J'ai ensuite fabriqué l'ensemble des composants dans la salle blanche du laboratoire (CTU/IEF Minerve), en collaboration avec Xavier Le Roux pour le développement des nouveaux procédés de fabrication. Enfin j'ai caractérisé l'ensemble des échantillons sur le banc de caractérisation expérimental développé dans le groupe, en collaboration avec Joan-Manel Ramirez alors post-doctorant au laboratoire. Les principaux résultats obtenus sont résumés ci-dessous.

## Guide d'onde graduels SiGe riches en Ge dans le MIR

Trois différents plateformes graduelles SiGe ont été étudiées. La section transverse des guides d'ondes et le profil de l'indice de réfraction de chaque plate-forme sont illustrés sur la Fig.2. La plateforme A est composée d'une couche graduelle de 11  $\mu\text{m}$  d'épaisseur avec une augmentation linéaire de la concentration en Ge de 0 à 79%, suivie d'une couche homogène, de composition constante, de  $\text{Si}_{0.2}\text{Ge}_{0.8}$  formant le cœur du guide d'onde. Cette conception provient d'études antérieures dans les longueurs d'onde du proche infra-rouge et forme le point de départ de ces études. Les deux autres plateformes ont été conçues pour augmenter le confinement optique en diminuant l'épaisseur totale et en augmentant le gradient d'indice. La plateforme B est ainsi formée d'une couche graduelle de 6  $\mu\text{m}$  d'épaisseur dans laquelle la concentration en Ge augmente linéairement de 0 (Si pur) à 100% (Ge pur). Enfin, une troisième plate-forme C est composée de deux couches graduelles d'une épaisseur totale de 4  $\mu\text{m}$ . Une couche de 3  $\mu\text{m}$  d'épaisseur est d'abord utilisée, avec une concentration en Ge passant de 0 (Si pur) à 50% ( $\text{Si}_{0.5}\text{Ge}_{0.5}$ ). Une seconde couche graduelle de 1  $\mu\text{m}$  d'épaisseur avec une concentration en Ge allant de 50% à 100% (Ge pur) est placée sur le dessus.

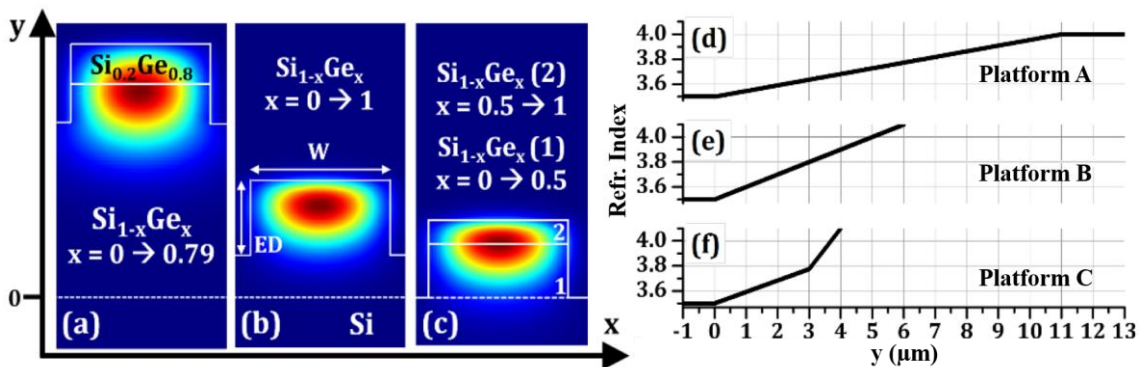


Fig.2. Vue en coupe des guides d'onde et profils d'indice correspondant le long de la direction verticale.

Pour étudier les pertes de propagation des guides d'ondes, des guides d'ondes en spirale de différentes longueurs ont été fabriqués. En utilisant la méthode du cutt-back, comme illustré sur la figure 3, des pertes de propagation inférieures à 3 dB / cm ont été obtenues pour des guides d'onde des plates-formes A et B, pour une longueur d'onde allant de 5.5 à

8.5  $\mu\text{m}$ , limitée seulement par notre système de caractérisation. Des pertes plus élevées sont obtenues pour la plate-forme C.

Les guides en spirale fabriqués sur la plateforme A ont ensuite été utilisés pour la première preuve de concept concernant la possibilité de détecter la présence de molécules, par l'absorption de la partie évanescente du mode optique. Pour cela les pertes de propagation des guides d'onde ont été mesurés à nouveau après dépôt d'une couche de résine sur les guides. Une forte augmentation des pertes est obtenue, pour les longueurs d'onde correspondant à l'absorption de la résine (Fig4), ce qui démontre de manière expérimentale la possibilité d'utiliser ces guides pour la détection de molécules. Une étude détaillée des capacités de détection est présentée dans le chapitre 2.

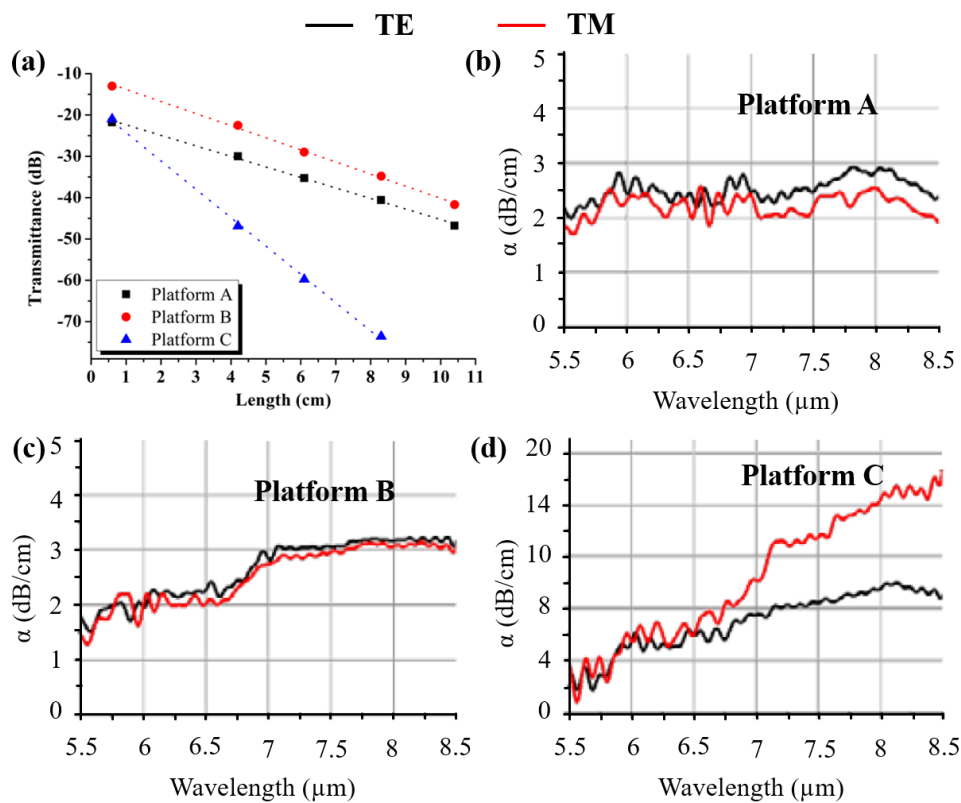


Fig.3. (a) Transmission en fonction de la longueur de guide en polarisation quasi-TE, à la longueur d'onde de 7.5  $\mu\text{m}$ ; (b)-(d) Pertes de propagation mesurées expérimentalement de 5.5 à 8.5  $\mu\text{m}$  sur les différentes plateformes.

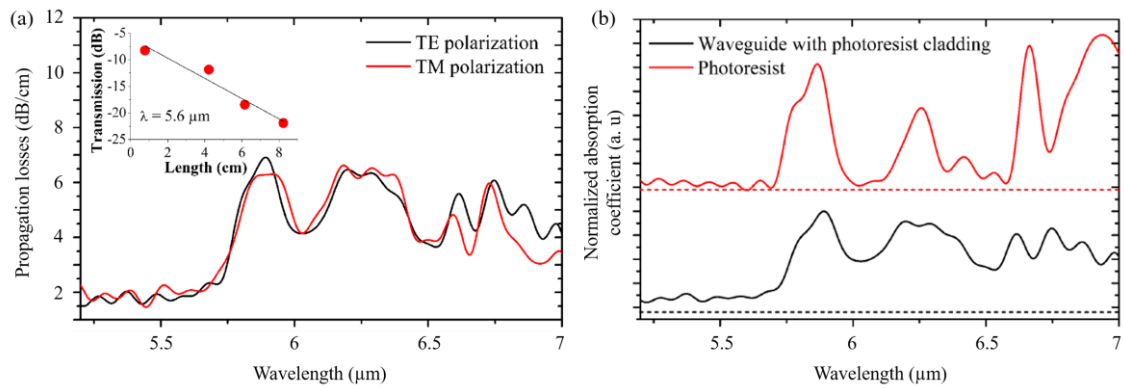


Fig.4. (a) Pertes de propagation des guides d'onde SiGe recouvert par la résine S1818, en polarisation TE et TM ; (b) Coefficient d'absorption normalisé de la résine, compare aux pertes des guides d'onde couverts par la résine. Un bon accord est obtenu concernant la position des pics d'absorption.

## Guides d'onde périodiques

Après les premières preuves de concept concernant la possibilité de guider la lumière à faibles pertes, j'ai étudié les guides d'onde périodiques pour 2 applications principales : la réalisation de coupleurs verticaux et de miroirs de Bragg intégrés. Ces travaux ont été menés sur la plateforme B, présentant de faibles pertes et un bon confinement optique.

Un réseau de couplage circuit intégré vers fibre optique a été conçu, pour les polarisations TE et TM. Des efficacités de couplage de -12 dB en polarisation TE et -9.6 dB en polarisation TM sont obtenues. La bande passante à -1 dB est de plus de 300 nm.

Ensuite des guides d'onde à réseau de Bragg ont été conçus, fabriqués et caractérisés. Le réseau est obtenu par corrugation de la surface du guide d'onde. Une bande interdite a été démontrée à différentes longueurs d'onde allant de 5.4 à 8.4 μm, comme illustré sur la figure 5. Une rejection maximale atteignant 21.6 dB a été mesurée, pour un réseau de 280 périodes, à la longueur d'onde de 6.4 μm.

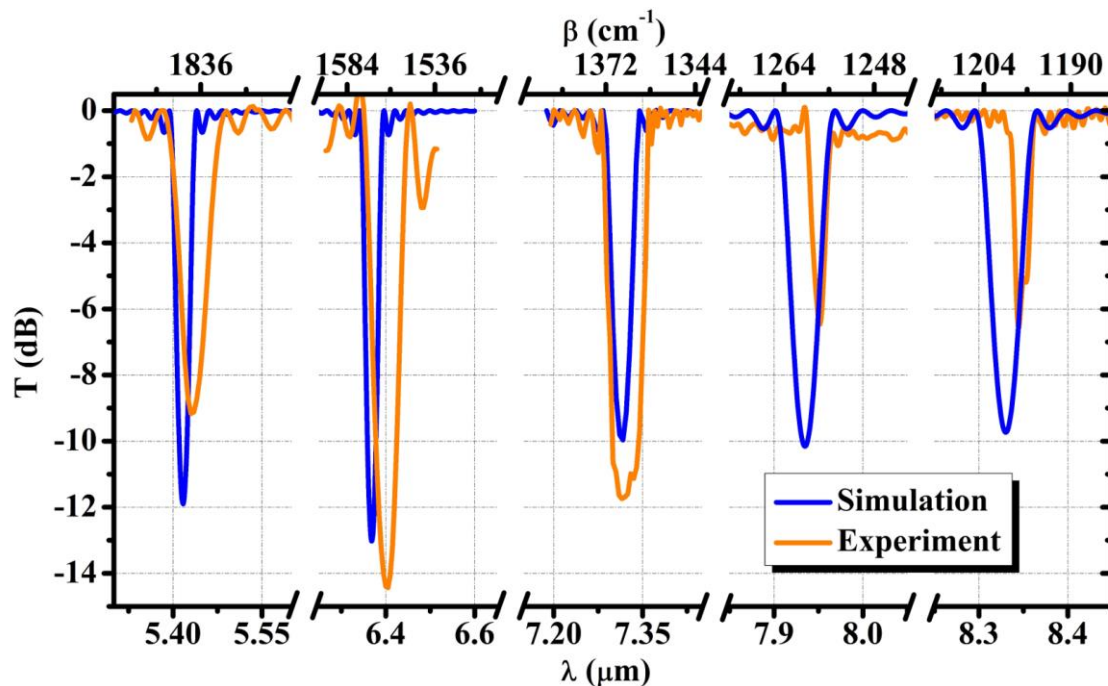


Fig.5. Spectre de transmission simulé (courbe bleue) et mesuré (courbe orange) des guides d'onde SiGe à réseaux de Bragg . Les réseaux comprennent 250 périodes, et les périodes sont de 0.74, 0.88, 1.02, 1.10, 1.16  $\mu\text{m}$ , correspondant à une bande interdite à 5.4, 6.4, 7.3, 7.95 and 8.35  $\mu\text{m}$ , respectivement.

## Résonateurs MIR intégrés

A partir de la démonstration des réseaux de Bragg intégrés en guide d'onde, des cavités Fabry-Perot (FP) utilisant ces réseaux de Bragg comme miroirs réfléchissants ont été conçues, fabriquées et caractérisées. Un fonctionnement à une longueur d'onde de 8  $\mu\text{m}$  environ était visé. Les résonances des cavités Fabry Perot sont clairement visibles sur la figure 6 (a), au centre de la bande interdite des miroirs. Des facteurs de qualité de 1514 et 1272 ont pu être estimés sur les mesures expérimentales.

La transmission d'une cavité utilisant des miroirs de Bragg à 500 périodes est reportée sur la Fig.6 (b). Le facteur de qualité atteint alors 2200 à la longueur d'onde de 7,95  $\mu\text{m}$ . Les performances des cavités FP et de leurs facteurs de qualité sont traités en détail dans le manuscrit. Il est possible que les facteurs de qualité mesurés soient limités par le banc de caractérisation expérimental.

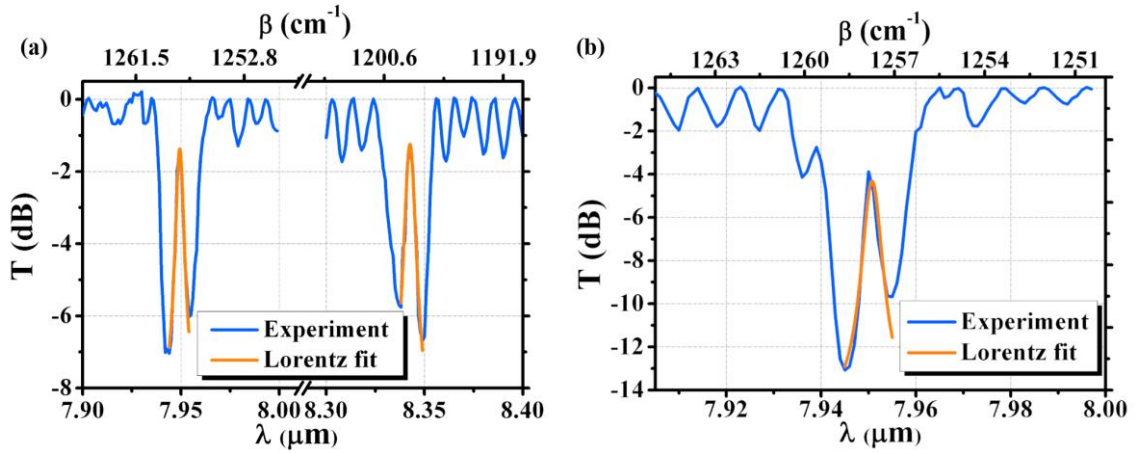


Fig.6. (a) Spectres de transmission expérimentaux pour des cavités Fabry-Perot de longueur de cavité 70  $\mu\text{m}$ . Les miroirs de Bragg comprennent 280 périodes, la période étant de  $\Lambda = 1.1 \mu\text{m}$  à gauche (résonance à 7.95  $\mu\text{m}$ ) et  $\Lambda = 1.16 \mu\text{m}$  à droite (résonance à 8.34  $\mu\text{m}$ ). (b) Spectre de transmission expérimental pour une cavité de longueur 70  $\mu\text{m}$ , les miroirs de Bragg comprennent 500 périodes, la période étant  $\Lambda = 1.1 \mu\text{m}$ .

Outre les cavités FP, nous avons démontré la possibilité d'intégrer des résonateurs de type « ractrack » fonctionnant à la longueur d'onde de 8  $\mu\text{m}$ . On peut observer sur la figure 7 que les résonateurs ayant un rayon de courbure supérieur à 50  $\mu\text{m}$  fonctionnent sur une large bande spectrale de 900 nm. Un facteur de qualité maximum de 3600 est obtenu à 8  $\mu\text{m}$  de longueur d'onde, avec un écart entre résonance (FSR) d'environ 8 nm.

Ces premières démonstrations de structures résonantes MIR intégrées utilisant les guides d'onde SiGe graduels ouvrent la voie au développement futur de circuits photoniques intégrés MIR, tels que des sources lumineuses utilisant des effets non linéaires, à savoir la génération de peignes de fréquence. En ce qui concerne l'amélioration de l'interaction lumière-matière, les structures résonantes MIR présentent également un fort potentiel pour le développement de systèmes de détection spectroscopiques ultra-compacts.

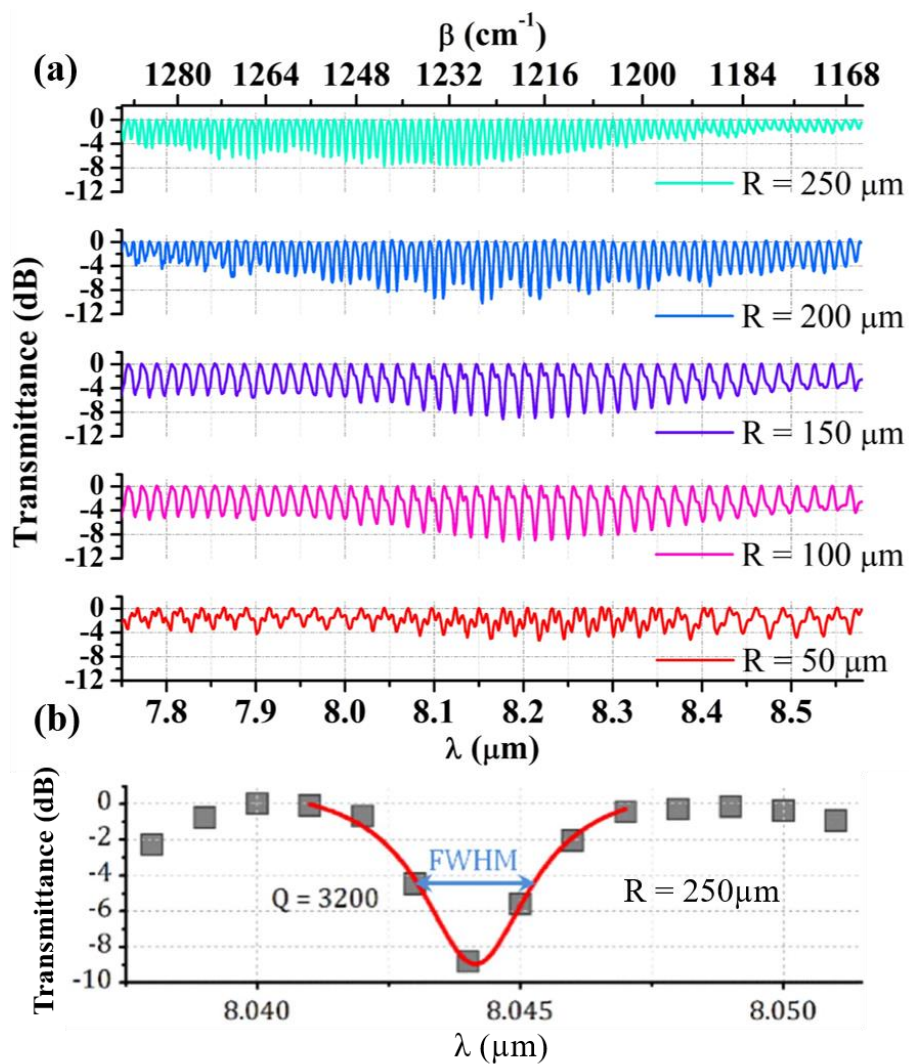


Fig.7. (a) Spectres de transmission expérimentaux des résonateurs “racetrack”, pour différentes rayons de courbure  $R$  allant de 50 à 250  $\mu\text{m}$ , en polarisation TM; (b) zoom sur une résonance, pour  $R = 250 \mu\text{m}$ , et fit Lorentzien (courbe rouge).

## Spectromètre à transformée de Fourier intégrée

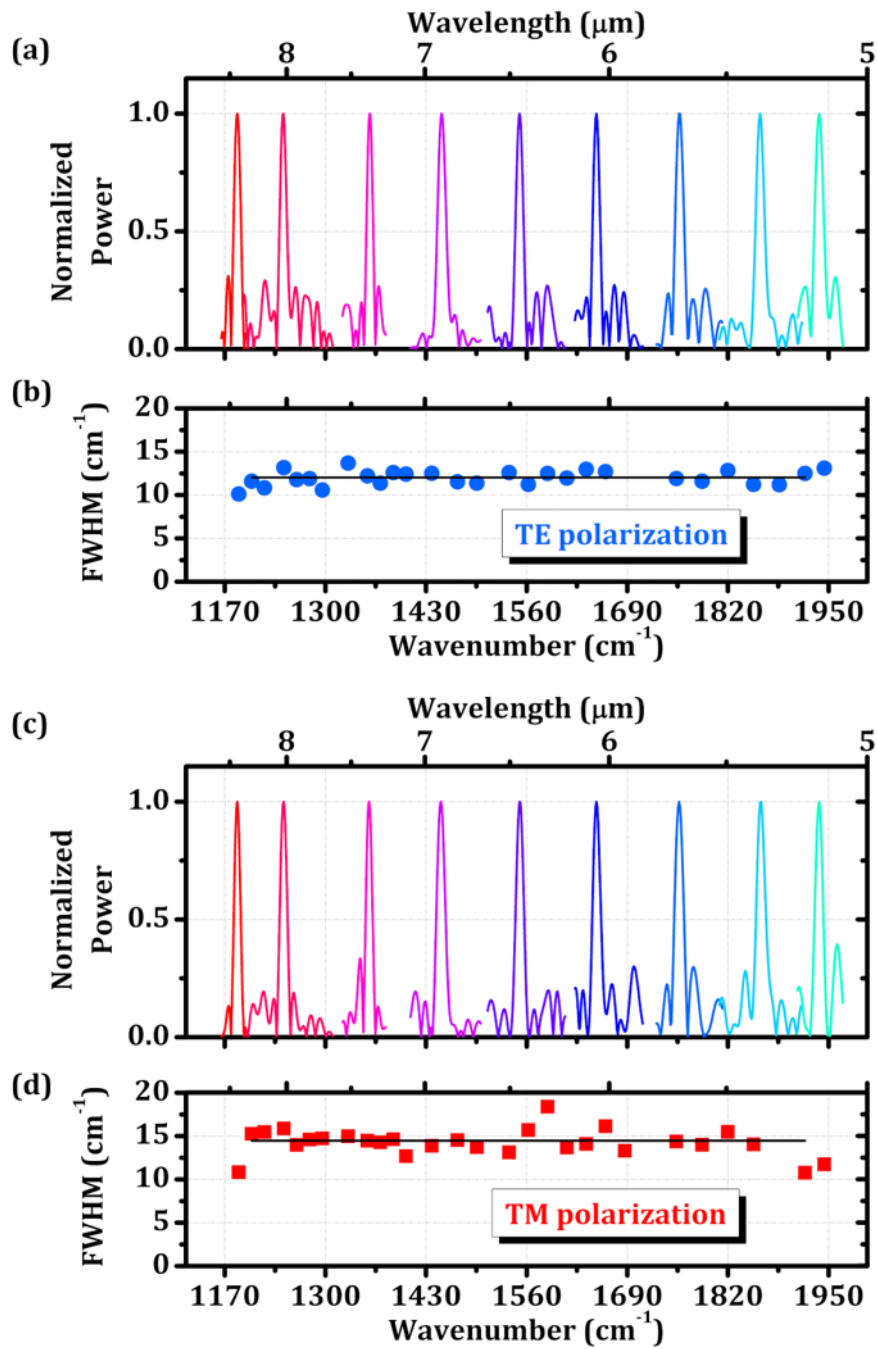


Fig.8. Spectres retrouvés expérimentalement à l'issue du traitement des données obtenues en sortie du spectromètre, pour différentes sources monochromatiques placées à l'entrée, allant de 1170 à 1950  $\text{cm}^{-1}$  en polarisation TE et TM. (a,c). Largeur à mi-hauteur (FWHM) des signaux retrouvés indiquant la résolution du spectromètre.

La réalisation d'un spectromètre intégré est un élément clef pour la détection spectroscopique. Le premier spectromètre intégré MIR fonctionnant à haute longueur

d'onde a été réalisé pendant la thèse. Il s'agit d'un spectromètre hétérodyne à transformé de Fourier utilisant la plateforme SiGe à gradient d'indice, dont la conception, fabrication et caractérisation expérimentale est discutée dans le chapitre 5. Des exemples de spectres de signaux retrouvés expérimentalement, à l'issue du traitement des données obtenues en sortie du spectromètre sont reportés sur la figure 8. De manière intéressante, le spectromètre fonctionne en polarisation TE et TM, sur une large bande spectrale de  $800\text{ cm}^{-1}$  (c'est-à-dire pour des longueurs d'onde allant de 5 à  $8.5\ \mu\text{m}$ ). Le FSR du spectromètre est de  $132,5\text{ cm}^{-1}$  et sa résolution spectrale est inférieure à  $15\text{ cm}^{-1}$  pour les deux polarisations.

## **Conclusion**

L'objectif à long terme de ces travaux concerne la démonstration d'un système spectroscopique sur circuit intégré photonique, fonctionnant dans la plage de longueurs d'onde du MIR et couvrant la région du « fingerprint ». Des résultats marquants ont été obtenus : guides d'onde à faibles pertes dans une grande gamme de longueur d'onde, preuve de concept de détection de molécules, premières démonstrations de résonateurs intégrés fonctionnant à  $8\ \mu\text{m}$  de longueur d'onde et de spectromètres intégrés fonctionnant dans une large bande spectrale de 5 à  $8.5\ \mu\text{m}$ . L'ensemble de ces résultats démontre le potentiel des structures à guides d'onde SiGe à gradient d'indice pour la réalisation de circuits photoniques intégrés MIR, et ouvre la voie à la réalisation de circuits complexes pour la réalisation de fonctions optiques.

# Table of Content

<b>Acknowledgements.....</b>	<b>5</b>
<b>Résumé en Français .....</b>	<b>8</b>
<b>Table of Content.....</b>	<b>18</b>
<b>1. Introduction.....</b>	<b>20</b>
1.1. <i>Integrated optical sensors .....</i>	20
1.2. <i>Mid-infrared Silicon photonics.....</i>	21
1.3. <i>State of the art.....</i>	23
1.4. <i>Outline of Thesis .....</i>	30
1.5. <i>Scientific achievement of thesis.....</i>	32
<b>2. Broadband mid-IR waveguides based on Ge-rich graded SiGe waveguides, and Mid-infrared sensing by Evanescent Field absorption.....</b>	<b>34</b>
2.1. <i>Design of mid-infrared waveguides.....</i>	34
2.2. <i>Waveguides fabrication .....</i>	40
2.3. <i>Characterization .....</i>	43
2.3.1. <i>Description of experimental set-up .....</i>	43
2.3.2. <i>Experimental results .....</i>	44
2.4. <i>Study of sensing capability of <math>Si_{1-x}Ge_x</math> waveguides.....</i>	46
2.5. <i>Conclusion.....</i>	52
<b>3. Periodic Waveguides.....</b>	<b>53</b>
3.1. <i>MIR broadband grating couplers.....</i>	54
3.1.1. <i>Phase matching condition.....</i>	56
3.1.2. <i>Simulations: evaluation of grating coupler performances.....</i>	58
3.2. <i>Waveguide Bragg grating.....</i>	65
3.2.1. <i>Waveguide Bragg grating modeling and design.....</i>	66

3.2.2.	Fabrication .....	73
3.2.3.	Characterization and results .....	78
3.3.	<i>Conclusion</i> .....	80
<b>4.</b>	<b>Mid-IR integrated resonators .....</b>	<b>82</b>
4.1.	<i>Fabry-Perot Cavities</i> .....	82
4.1.1.	Analytical model and Simulations.....	83
4.1.2.	Fabrication .....	87
4.1.3.	Characterization .....	88
4.1.4.	Cavities with lateral corrugations.....	90
4.2.	<i>Racetrack Resonators</i> .....	93
4.2.1.	Analytical model and Simulations.....	94
4.2.2.	Fabrication .....	97
4.2.3.	Characterization .....	98
4.3.	<i>Conclusion</i> .....	102
<b>5.</b>	<b>Integrated mid-infrared Fourier-Transform Spectrometer .....</b>	<b>104</b>
5.1.	<i>Introduction of Fourier-Transform infrared Spectroscopy</i> .....	104
5.2.	<i>Integrated broadband Si<sub>1-x</sub>Ge<sub>x</sub> Fourier Transform Spectrometer</i> .....	107
5.2.1.	Modal analysis and design .....	109
5.2.2.	Fabrication .....	112
5.2.3.	Characterization .....	113
5.3.	<i>Conclusion</i> .....	118
<b>6.</b>	<b>Conclusions and Future Directions .....</b>	<b>119</b>
6.1.1.	Conclusions .....	119
6.1.2.	Future Directions .....	121
	<b>References .....</b>	<b>123</b>

# 1. Introduction

Since the first demonstration of silicon waveguides using the silicon-on-insulator platform in the mid 1980's by Soref et al. [1,2], silicon photonic circuits have exhibited a truly remarkable development. Significant progress on silicon integration has been done for the last decades. Several important components containing the waveguides, modulators, switches, and detectors have been studied and impressively developed. Especially after the first investigation of silicon-based plasma dispersion modulation [3], a great number of demonstrations on silicon photonics have been done for applications in telecommunications and data centers. In the stream of the research for data communication and initially strongly inspired by the success of fiber sensors, silicon photonic circuits have also been proposed as a compelling solution to address several technical challenges in current chemical and biological sensing systems for the applications of medical diagnosis, metrology, and remote sensing. The on-chip integrated optical sensor is among the hot research topics in the optical society.

## 1.1. Integrated optical sensors

An optical sensor is a device that uses light to measure a physical quantity. A chemical or biological optical sensor allows to detect and quantify the presence of targeted molecules, by measuring light transmission, and translating it into a readable form, such as an electrical signal. It is a powerful tool, which can be used to measure a very large number of components, providing analyte information remotely. The research and development in optical sensor field is motivated by its significant advantages comparing to other sensors, such as a greater sensitivity, a wider bandwidth, an immunity to electromagnetic interference and multiplexing capabilities. Moreover, for the applications of chemical and biological sensing, optical sensors benefit also from the multi-analyte detection [4]. Furthermore, another important advantage of optical sensors is the selectivity. Selectivity can be understood as one-to-one correspondence of the optical response to a nature of the presented analyte.

In the research and development of optical sensors, miniaturization of optical sensors by integration is particularly interesting. Integrated optical (IO) system benefit from compactness, cost-effective, mechanical rigidity and multifunctionality. Thanks to the integrated waveguides, the optical path for an integrated optical sensor is well defined without necessity of positions (re-)adjustment of the bulky components that free space optics is notorious for. In comparison with fiber optics, on chip integration (many systems can be integrated simultaneously on one substrate), shows a great flexibility in material choice (see [section 1.3](#)) and structures which make possible for the development of multi-purpose and mobile in-situ analysis system. The real-time and in-situ aspects of IO sensors are particularly interesting, due to the complexity and time-consuming in the analysis progress in conventional sensing systems, in which the transport of samples to a laboratory is necessary for the analysis using an expensive bulky equipment.

The operation mechanism of IO sensors is related to changes of optical properties when the measurand is present. The most relevant optical properties are the refractive index, the absorption coefficient (the sensing mechanism used in this work), or the luminescence of the material. The change of refractive index is represented through a change of two parameters: the real part of effective index and the mode profile of the guided mode [5–7]. The change of absorption coefficient (sensing principle performed in this work) corresponds to the imaginary part of effective index, it affects thus the modal attenuation, in other words the detected transmission [8–12]. In terms of the luminescence sensing (fluorescence sensing), some materials may show luminescent property by emitting photons at different frequency while absorbing the incident light, allowing their detection [13–17].

## **1.2. Mid-infrared Silicon photonics**

The research towards IO sensors using silicon photonics technology is becoming increasingly attractive. Silicon photonics, known more accurately as group IV photonics, describes integrated optic and optoelectronic devices realized using silicon (Si), germanium (Ge) or other group IV materials. Since the first demonstration of silicon waveguide in the mid 1980's [2,18], silicon photonic circuits have been strongly studied motivated primary because of the potential attraction of integration with microelectronics in a cost-effective

manner. As a result, a continuously increasing number of research works, containing a diversity of integrated optical components for light generation, modulation, manipulation, detection and amplification, have been reported, especially for the application of telecommunication operating at near infrared (NIR) wavelengths. A large number of silicon-based refractive index sensing circuits with high performance have been also demonstrated in the near infrared wavelength range in the last decade [5,19–22]. However, the lack of selectivity to identify the exact analyte in the refractive index sensing limits its applications.

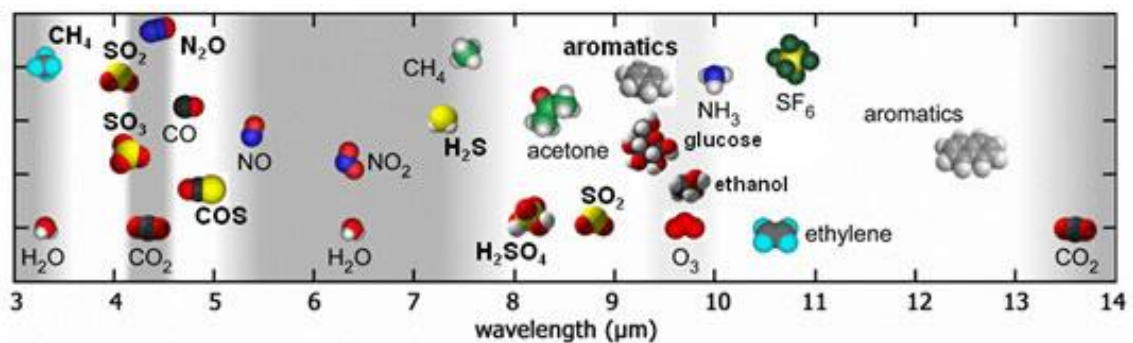


Fig.1.2.1. Example mid infrared molecular absorption wavelengths from [23].

Interestingly silicon photonics device can extend in the mid-infrared (MIR) range, which is particularly interesting for sensing applications [24]. The mid infrared is typically defined as wavelengths from 2 to 20  $\mu\text{m}$  ( $5000$  to  $500\text{ cm}^{-1}$  in wavenumbers). Among it is the so called “molecular fingerprint” region from 6.6 to 20  $\mu\text{m}$  where almost all chemical bonds present fundamental vibrational and rotational signatures as shown in Fig.1.2.1. The presence of this signature give rise to unique absorption lines for each molecule in the MIR fingerprint region. Although overtones of molecular vibrational signature extend into the NIR wavelengths ( $\lambda < 2\ \mu\text{m}$ ) which can also be detected, the absorption coefficient in the MIR are orders of magnitude higher than in the NIR, so by shifting the operational wavelength into MIR the detection sensitivity can be enhanced by several orders. Moreover, since each molecule presents unique absorption lines, none complementary identification process is needed for MIR absorption sensing. On another hand, it can be added that the development of photonic integrated devices in the two atmospheric transparency windows ( $\lambda = 3\text{-}5\ \mu\text{m}$  and  $\lambda = 8\text{-}12\ \mu\text{m}$ ) is also significant for applications of free-space telecommunication.

In this context, a growing number of research works are now devoted to mid-infrared silicon photonics. Many outstanding works on novel MIR silicon photonics passive and active devices have been reported and are summarized in recent review papers [25–31]. Furthermore it can be noted that some research works are also now focused on the integration of MIR QCL on Si-based platform [32]. More details on state of the art of MIR integrated photonics are discussed in the next section.

### 1.3. State of the art

In order to develop MIR photonics, it is essentially to find a waveguide platform that allows light propagation with low loss in the MIR wavelength range. The most prevalent platform in the field of silicon photonics in the near-IR is the silicon-on-insulator (SOI) platform which provides a high index contrast between the guiding core ( $n_{Si} = 3.5$ ) and the buried oxide ( $n_{SiO_2} = 1.5$ ) leading to high optical confinement. Interestingly, silicon is transparent up to 8  $\mu\text{m}$  wavelength [24], however, the strong absorption of SiO<sub>2</sub> at the wavelengths beyond 3.6  $\mu\text{m}$  could limit the use of classical SOI waveguides at longer wavelengths.

SOI waveguides have thus been demonstrated with propagation loss as low as 0.6-0.7 dB/cm at  $\lambda = 3.39 \mu\text{m}$  [33]. [Fig.1.3.1\(a,b\)](#) shows the demonstration of high efficiency grating couplers around 2  $\mu\text{m}$  [34]. An on-chip Fourier-Transform (FT) spectrometer with cascaded 42 Mach-Zehnder interferometers (MZI) has been demonstrated at a wavelength around 3.75  $\mu\text{m}$  [35] as shown in [Fig.1.3.1\(c\)](#).

Different approaches have then been reported to extend the operation of SOI platform to larger wavelength, such as a proper waveguide design to limit the mode overlap with the SiO<sub>2</sub> under cladding [36] ([Fig.1.3.1\(d\)](#)), or the use of suspended Si waveguides by under-etching the buried oxide with a subwavelength technology [37], as shown in [Fig.1.3.1\(e,f\)](#). Propagation losses of 3.1 dB/cm has achieved at a wavelength of 7.67  $\mu\text{m}$  using this suspended Si approach.

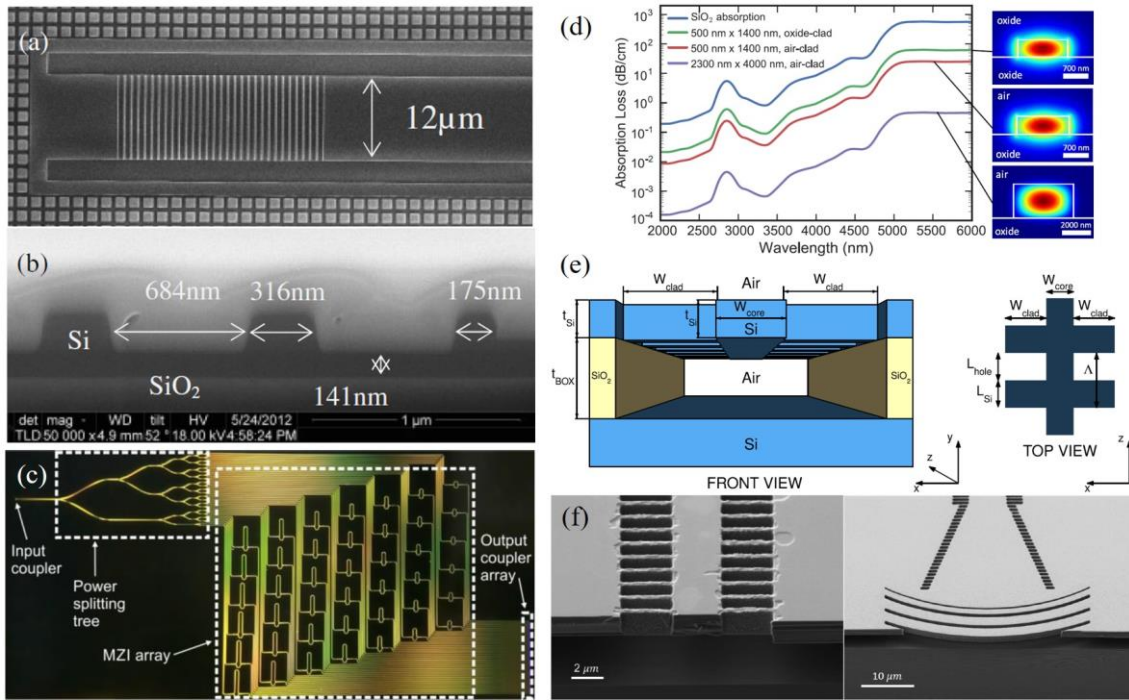


Fig.1.3.1. (a) and (b) Top view and cross section of scanning electronic microscope (SEM) images of fabricated grating coupler, from Ref. [34]; (c) Optical micrograph of Fourier Transform infrared (FTIR) spectrometer with 42 cascaded MZIs from Ref. [35]; (d) Simulated absorption losses for different waveguide cross-sectional geometries, from Ref. [36]; (e) and (f) Schematic representation and SEM images of suspended Si waveguide with subwavelength grating cladding from Ref. [37].

Besides of silicon and silicon dioxide, the transparency windows of different materials are reported and compared on [Fig.1.3.2](#) (Silicon Nitride ( $\text{Si}_3\text{N}_4$ ), sapphire ( $\text{Al}_2\text{O}_3$ ), germanium (Ge), gallium arsenide (GaAs), Chalcogenide glasses (ChG) [24,28,38]).

III-V materials, like GaAs show a wide transparency window from 1.6 up to 16  $\mu\text{m}$ . In the meantime, they benefit from a natural integration with QCL laser sources, making them a good material for the development of mid infrared silicon photonic devices. On-chip GaAs MZI for chemical sensing operating between 5.78 and 6.35  $\mu\text{m}$  have thus been demonstrated [39] ([Fig.1.3.3\(a\)](#)).

Chalcogenide glasses are also remarkable due to the large transparency in the MIR range. Recent achievements include MIR resonators with a quality factor of  $10^5$  at 5.2  $\mu\text{m}$  [40] ([Fig.1.3.3\(b\)](#)) and the supercontinuum generation from 2-10  $\mu\text{m}$  in a chalcogenide rib waveguide [41] ([Fig.1.3.3\(c\)](#)).

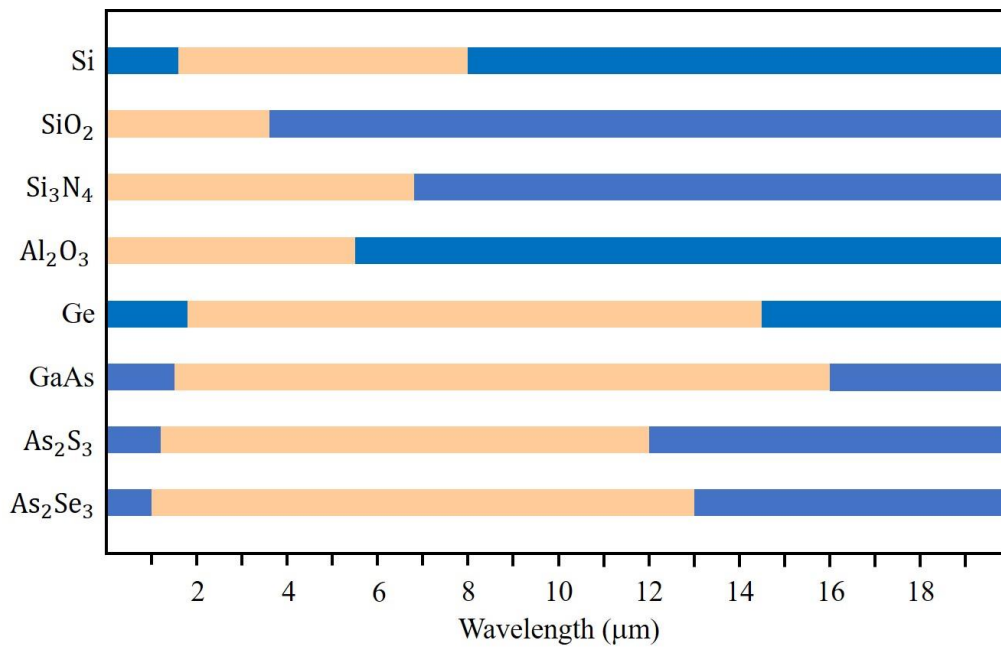


Fig.1.3.2. Materials transparency windows in near- and mid-infrared wavelengths. The blue areas represent high loss; the light orange areas represent optical transparency.

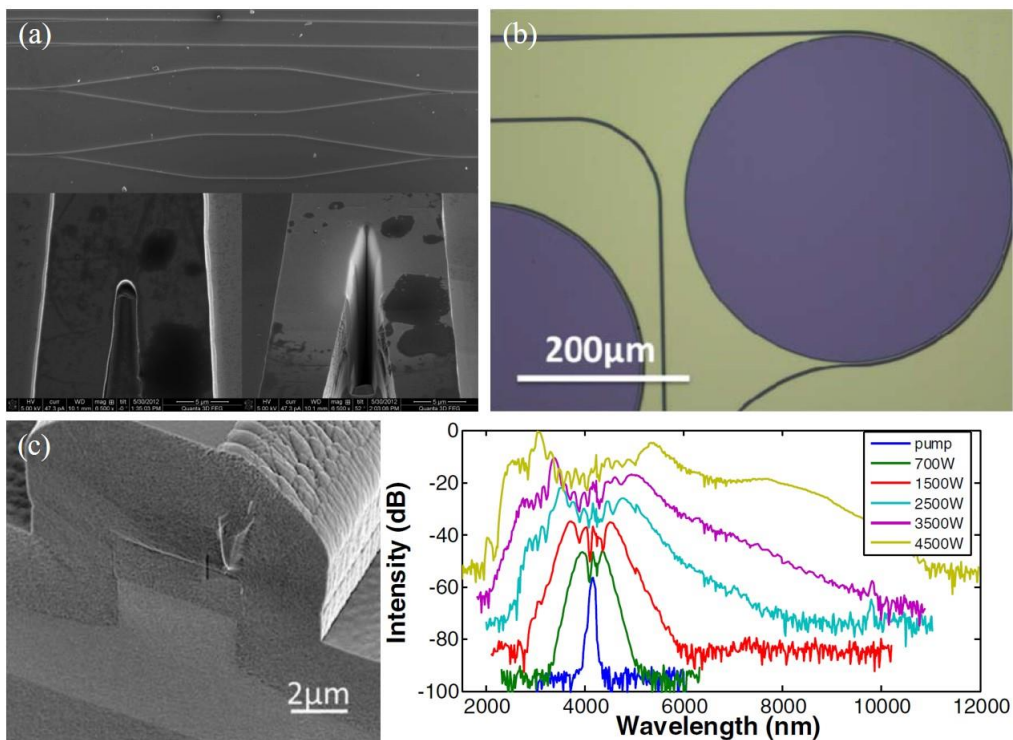


Fig.1.3.3. (a) SEM image of GaAs MZIs and Y-junction [39]; (b) Optical microscope top-view image of a MIR ChG resonator [40]; (c) SEM image of ChG waveguide and spectra of supercontinuum generated from the waveguide at different pump peak power levels [41].

Alternatively, different silicon-based platforms including silicon nitride and silicon-on-sapphire (SOS) also show good performance in the mid infrared operation. Low-loss waveguide [42] ([Fig.1.3.4\(a\)](#)), high efficiency strip-to-slot waveguide mode converter [43] ([Fig.1.3.4\(b\)](#)), supercontinuum generation within T-shaped waveguide [44] ([Fig.1.3.4\(c\)](#)) and high quality-factor ring resonators [45] ([Fig.1.3.4\(d\)](#)) have been demonstrated on the SOS platform at different wavelengths in the MIR range between 1.55  $\mu\text{m}$  and 6  $\mu\text{m}$ .

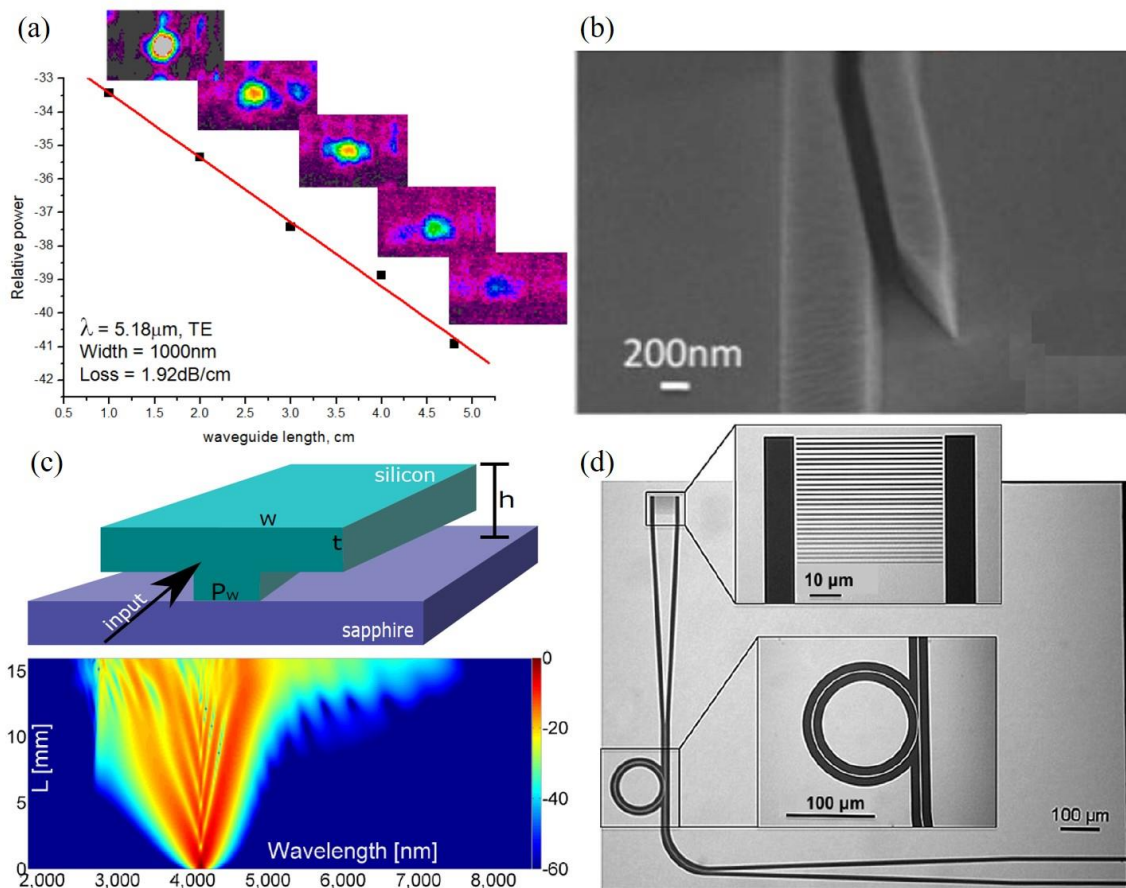


Fig.1.3.4. (a) Propagation loss of SOS strip waveguide at  $\lambda = 5.18 \mu\text{m}$  with imaged mode profile [42]; (b) SEM image of SOS strip-to-slot waveguide converter [43]; (c) Schematic view of T shape waveguide and the pulse evolution in the spectral domain [44]; (d) Optical image of SOS (top inset) grating coupler and (bottom inset) ring resonator [45].

In parallel, low-loss silicon-on-silicon-nitride (SON) strip waveguides have been investigated at 3.4  $\mu\text{m}$  [46] ([Fig.1.3.5\(a\)](#)). Moreover, active devices have also been developed in silicon nitride platforms based on the integration of quantum cascaded laser

[47,48] (Fig.1.3.5(b,c)) or on non-linear effect to achieve frequency comb generation [49] (Fig.1.3.5(d)).

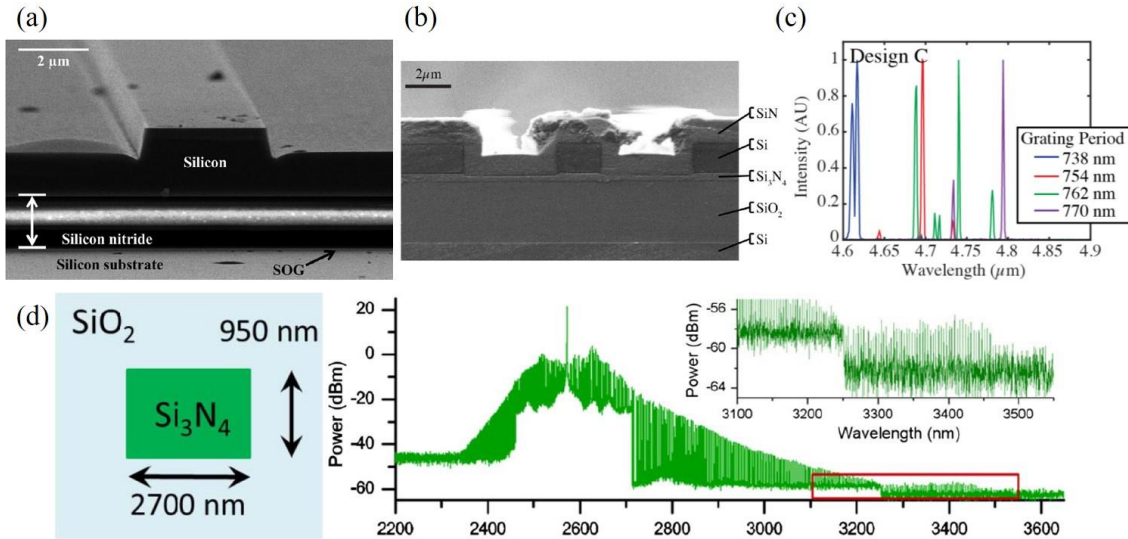


Fig.1.3.5. (a) SEM image of SON strip waveguide [46]; (b) SEM image of polished end-facet of integrated QCL [47]; (c) Normalized emission spectra of DFBs integrated on silicon [48]; (d) Schematic cross section of silicon nitride resonator, and experimentally generated frequency comb [49].

However, until now most of the reported works are in a limited wavelength range below 8  $\mu\text{m}$ , while long-wave MIR operation devices covering the wide fingerprint region are highly desirable. Unfortunately, multi-phonon absorption occurs in silicon for wavelengths beyond 8  $\mu\text{m}$ . Therefore, it is extremely challenging to develop long-wave infrared (LWIR) devices with silicon.

Interestingly Germanium is an alternative material which shows transparency up to about 15  $\mu\text{m}$ . Not only the wide transparency window, but also the high 3<sup>rd</sup> order nonlinearity [50] make Ge a good material for the demonstration of LWIR silicon photonic devices. Furthermore, Ge is already largely used in silicon photonics and is fully compatible with mature large volume Si photonics fabrication process.

In the last years, Ge-based photonic integrated circuits dedicated LWIR operation have witnessed a burst of research activities. Losses of 2.5 dB/cm have been obtained using Ge-on-Si strip waveguide at 5.8  $\mu\text{m}$  wavelength [51] (Fig.1.3.6(a)). Benefiting from the thermal/electrical isolation of silicon dioxide, thermo optics phase shifters and thermally tunable racetrack resonators have been investigated at 5  $\mu\text{m}$  on Ge-on-SOI (GOSOI)

platform [52,53] (Fig.1.3.6(b,c)). Then, taking advantage of high index contrast between Ge and SiO<sub>2</sub>, Ge-on-insulator (GOI) has also been proposed as a good material to develop LWIR photonic integrated devices. Nanocavity [54] (Fig.1.3.6(d)) and ring resonator [55] (Fig.1.3.6(e)) with quality-factor as high as 10<sup>5</sup> at 2.5 μm wavelength have been demonstrated on GOI membraned waveguides.

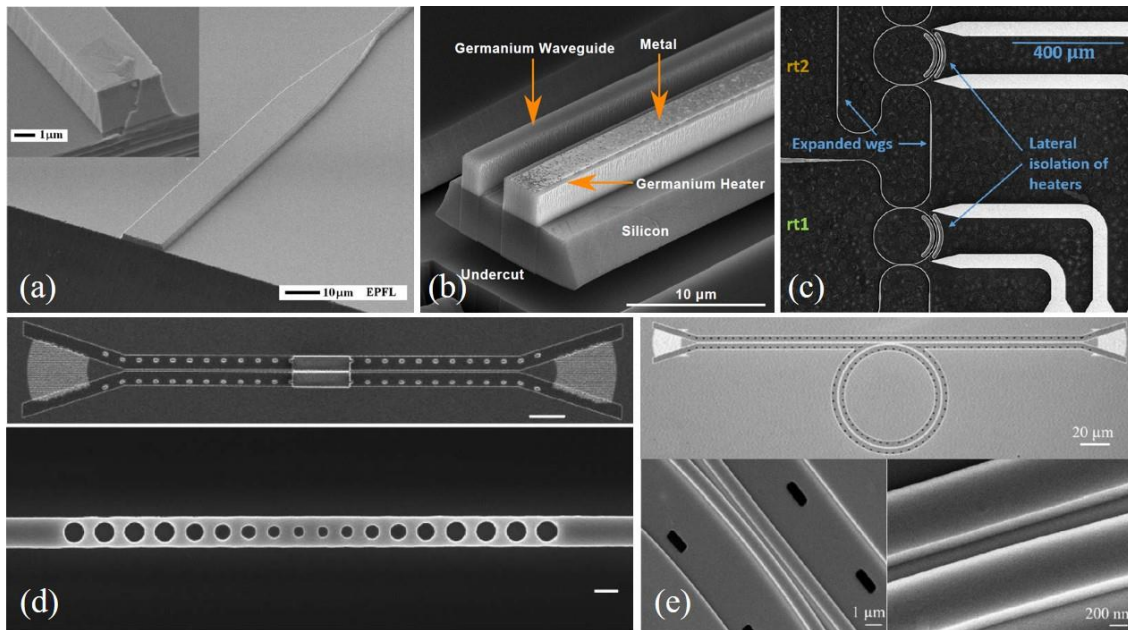


Fig.1.3.6. SEM images of (a) GOS strip waveguide [51]; (b) GOSOI thermal optics phase shifter [52]; (c) Vernier racetrack resonators [53]; (d) GOS nanocavity [54]; (e) GOS ring resonator [55].

In parallel with pure Ge-based waveguides, the use of SiGe alloys benefits from a low threshold dislocation density (TDD), especially when graded SiGe layers are used. Furthermore, the use of SiGe alloys allow a high versatility for engineering waveguide properties such as effective index and dispersion. Low-loss waveguides have been demonstrated, with 0.5 dB/cm propagation loss at 4.75 μm based on Si<sub>0.6</sub>Ge<sub>0.4</sub> waveguides [56] (Fig.1.3.7(a)). Graded-index SiGe waveguides has been firstly developed in 2014 [57]. The electromagnetic field is guided in the graded layer with Ge concentration from 0 to 40%, and propagation losses as low as 1 dB/cm at λ = 4.5 μm and 2 dB/cm at 7.4 μm have been obtained (Fig.1.3.7(b)). Based on this waveguide, arrayed waveguide gratings (AWG) operating at 4.5 μm and 7.6 μm have been investigated [58,59].

Another approach has also been proposed for MIR integrated photonics. Instead of implementing high Si concentration in the alloy, Ge-rich  $\text{Si}_{1-x}\text{Ge}_x$  alloys and graded  $\text{Si}_{1-x}\text{Ge}_x$  layers are expected to benefit from a wider transparency window, which could potentially extend up to  $15\ \mu\text{m}$  as the refractive index gradient pushes the optical mode far from the Si substrate (Fig.1.3.7(c)) [60].

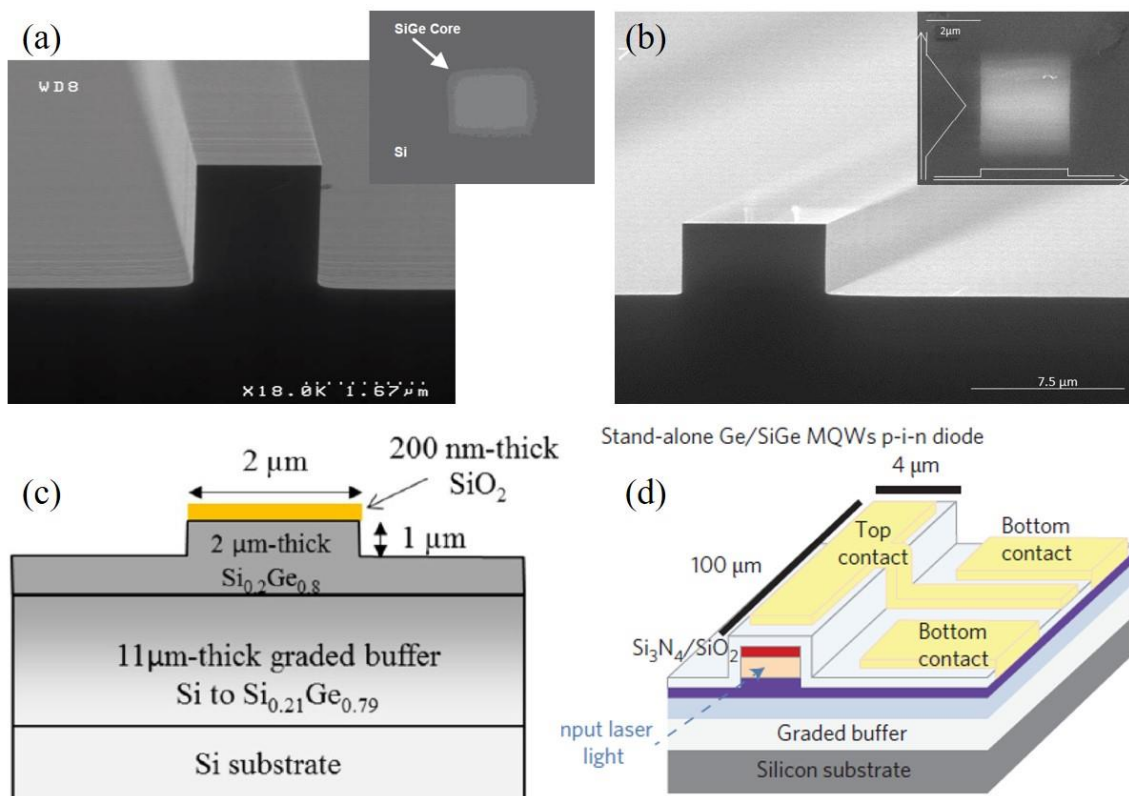


Fig.1.3.7. SEM images of (a)  $\text{Si}_{0.6}\text{Ge}_{0.4}$  waveguide [56] (b) graded SiGe waveguide [57]; (c) Schematic view of the cross-section of slightly etched SiGe waveguide [60]; (d) Schematic of a stand-alone Ge/SiGe MQWs p-i-n diode [61].

It can be noted that these waveguides have been proposed and developed first in the near infrared range, to integrate Ge/SiGe Quantum well structures for light modulation using quantum-confinement stark effect and for photodetection [61–63] (Fig.1.3.7(d)). The extension of these waveguides to the MIR is the starting point of the ERC project INSPIRE (2015-2020, Univ. Paris Sud, Politecnico Di Milano) in which I have been fully involved during these 3 years. Comparing to all pre-mentioned MIR platforms, the development of MIR photonic integrated devices using Ge-rich graded-index SiGe platform benefits from

i) a wide transparency window of material, potentially up to 15  $\mu\text{m}$ ; ii) a suspension-free technology; iii) a high versatility of optical engineering; iv) a high 3<sup>rd</sup> order nonlinearity which is advantageous to demonstrate nonlinear active devices; v) a high crystalline quality with low TDD thanks to the graded layer; vi) as working in MIR, two photon absorption (TPA) is negligible which is notorious for NIR nonlinear effect. Many potential applications are foreseen, such as chemical and biological sensing, but also free-space telecommunication, satellite instrumentation or medical diagnosis to name a few. The work performed during this PhD thesis is focused on the development of MIR photonic integrated devices using Ge-rich graded-index SiGe platform for the applications in chemical and biological sensing.

## 1.4. Outline of Thesis

In a long-term vision, the final objective of these works is aimed to develop a monolithically MIR on-chip integrated optical sensor to realize label-free in-situ sensing. As an example, a schematic representation is shown in [Fig.1.4.1](#). The sensor contains a broadband light source, a sensing circuit, an on-chip spectrometer and light detectors. The broadband light source, covering a wide part of the fingerprint region, can exploit non-linear optical effects to achieve supercontinuum generation. The source could be pumped by an external quantum cascade laser, or an on-chip implemented laser. Light propagates then into a sensing circuit where evanescent field absorption occurs. It could be a long waveguide or MIR on-chip resonators. Then an on-chip spectrometer is used to separate the different wavelengths, and finally, light is sent into integrated photodetectors. In this thesis, we will focus on how to realize the MIR photonic integrated devices for chemical sensing using the Ge-rich graded-index  $\text{Si}_{1-x}\text{Ge}_x$  platform.

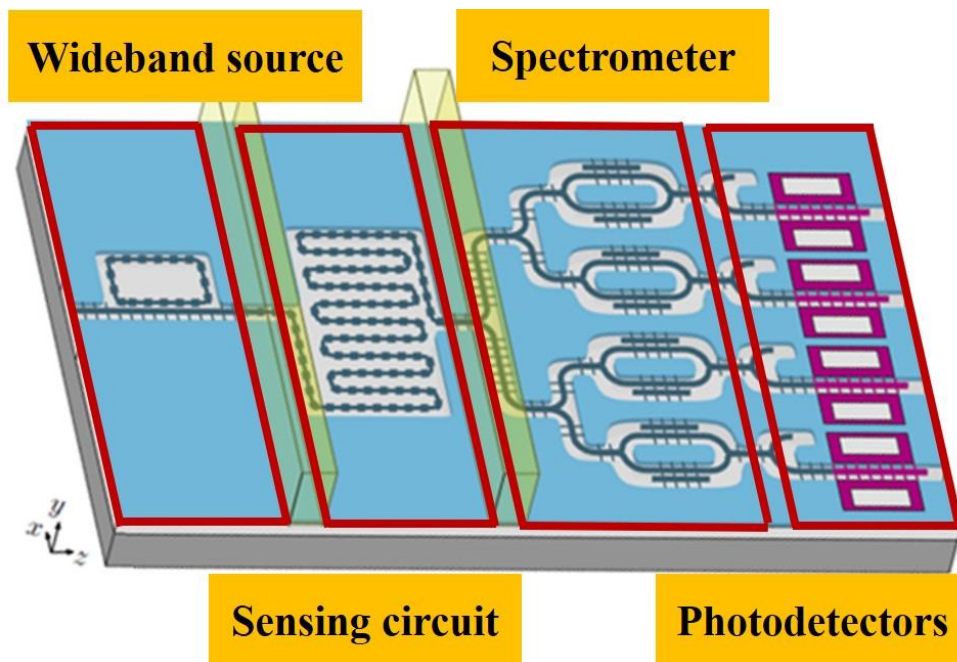


Fig 1.4.1. Schematic representation of the long-term monolithically integrated MIR sensor (Figure from C. Alonso Ramos).

To accomplish this task, the fundamental building blocks to guide light must be developed firstly. Then devices such as gratings, interferometers or resonators can be envisioned based on these waveguides. This thesis contains the discussion of different building blocks for the MIR photonic integrated circuits (PICs), such as broadband MIR waveguides, gratings, resonators and spectrometer. As mentioned in previous sections, mid infrared PICs using Ge-rich graded-index  $\text{Si}_{1-x}\text{Ge}_x$  platform show many advantages and potential for many applications. However, several challenges must be overcome:

- Development of low-loss broadband MIR waveguides. Conventional design of waveguides with dimensions in hundreds of nm, for example NIR waveguides are no longer available in this wavelength range. In order to guide long-wave, new waveguide design with larger guiding core is necessary. A specific attention must be paid on the achievable wavelength range, to target multi-detection systems. Since the waveguide dimensions are larger, efforts must be done for the lithography and etching process in order to achieve deep-etched waveguides while maintaining a smooth sidewall.

- Development of resonant structures. In order to enhance the light-matter interaction, MIR resonators are highly desirable. As working on the graded-index platform, low vertical index contrast makes the demonstration of MIR resonators challenging. Careful design is necessary for gratings and directional couplers in the case of Bragg grating Fabry-Perot cavities and ring resonators, respectively. For ring resonators, the minimal bend radius and the related tradeoff in terms of free spectral range are important parameters to be evaluated.
- Characterization methods. Specific characterization set-ups must be developed. For example, optical fibers are much less mature in MIR wavelength in comparison with near-IR wavelength. However, using free-space configurations light coupling into/out from the sample chip becomes more challenging.

## 1.5. Scientific achievement of thesis

Considering all those challenges, the manuscript presents the work that has been done during this PhD thesis. It contains 4 main chapters whose contents are detailed below:

- Chapter 2 presents the demonstration of low loss broadband waveguides in the mid infrared up to wavelengths beyond silicon absorption ( $>8 \mu\text{m}$ ). Different waveguide designs have been proposed based on three different  $\text{Si}_{1-x}\text{Ge}_x$  platforms ([section 2.1](#)). Fabrication process mainly related to lithography and waveguide etching ([section 2.2](#)) have been optimized. Fabricated samples were characterized using a free-space configuration set-up ([section 2.3.1](#)). Propagation losses for different waveguide platform have been measured from 5.5 to 8.5  $\mu\text{m}$  ([section 2.3.2](#)). Then, a proof of concept about the sensing capability of the SiGe waveguide by evanescent field have been evaluated.
- Chapter 3 discusses periodic waveguides such as grating couplers ([section 3.1](#)) for light coupling in the photonic circuit, and for waveguide Bragg gratings ([section 3.2](#)). Two designs of grating couplers have been proposed for TE and TM polarizations, and simulation results are presented. Then, waveguide Bragg gratings have been designed ([section 3.2.1](#)), fabricated ([section 3.2.2](#)) and characterized ([section 3.2.3](#)).

- Chapter 4 introduces the first demonstrations of MIR resonant structures on graded-index  $\text{Si}_{1-x}\text{Ge}_x$  waveguides in terms of simulation, fabrication and experiment. Two approaches, Fabry-Perot cavities using waveguide Bragg gratings ([section 4.1](#)) and racetrack resonators ([section 4.2](#)), have been demonstrated at LWIR wavelengths.
- Chapter 5 presents the first demonstration of on-chip integrated broadband dual-polarization Spatial Heterodyne Fourier-Transform Spectrometer (SHFTS) based on Ge-rich graded-index  $\text{Si}_{1-x}\text{Ge}_x$  waveguides. Design and device performances are firstly discussed by means of modal analysis ([section 5.2.1](#)). Then, fabricated device has been characterized to evaluate its resolution and free spectral range ([section 5.2.3](#)).

## **2. Broadband MIR waveguides based on Ge-rich graded SiGe waveguides, and MIR sensing by evanescent Field absorption**

As a main objective of demonstrating on-chip integrated optical sensor which covers a wide wavelength range in the MIR fingerprint region. The most fundamental work is to demonstrate a broadband MIR operational platform which is the waveguide. In this chapter, the optical properties of Ge-rich graded-index  $\text{Si}_{1-x}\text{Ge}_x$  waveguides will be discussed. Waveguide designs are proposed using 3 different  $\text{Si}_{1-x}\text{Ge}_x$  materials. Then, the waveguide fabrication and systematic characterization with a free-space configuration are described. Finally, as a proof of concept, the sensing capability of such  $\text{Si}_{1-x}\text{Ge}_x$  waveguide based on evanescent field absorption is demonstrated.

### **2.1. Design of MIR waveguides**

As already discussed in [section 1.3](#), researchers over the world are now studying the possibility of many different materials to extend the operation of silicon photonics in the MIR. Among them, Ge-rich graded-index  $\text{Si}_{1-x}\text{Ge}_x$  is a promising candidate to develop the MIR photonic circuits. As a first objective, we want to compare different waveguide platforms to evaluate light propagation properties in the MIR.

#### **Waveguide optical property**

In order to extend the operation in the MIR, we start using the Ge-rich graded-index  $\text{Si}_{1-x}\text{Ge}_x$  waveguides that have already been demonstrated in the NIR [60] and in the MIR at  $4.6\ \mu\text{m}$  [64]. We thus use an epitaxial layer composed by a  $11\text{-}\mu\text{m}$ -thick graded buffer layer with a linear increase of Ge concentration from 0 to 79%, followed by a  $2\text{-}\mu\text{m}$ -thick constant composition of  $\text{Si}_{0.2}\text{Ge}_{0.8}$  as guiding core on top. Such configuration provides a linear increase of the refractive index in the graded buffer, allowing light confinement in the top  $\text{Si}_{0.2}\text{Ge}_{0.8}$  waveguide core, with a tiny refractive index step at the interface between graded layer and guiding core (see [Fig.2.1.1](#)). This first platform, also called platform A in

the following, was previously optimized for operation at telecommunication wavelength where pure Ge has high absorption, which explain that the maximal Ge concentration in the SiGe alloy is limited to 80%.

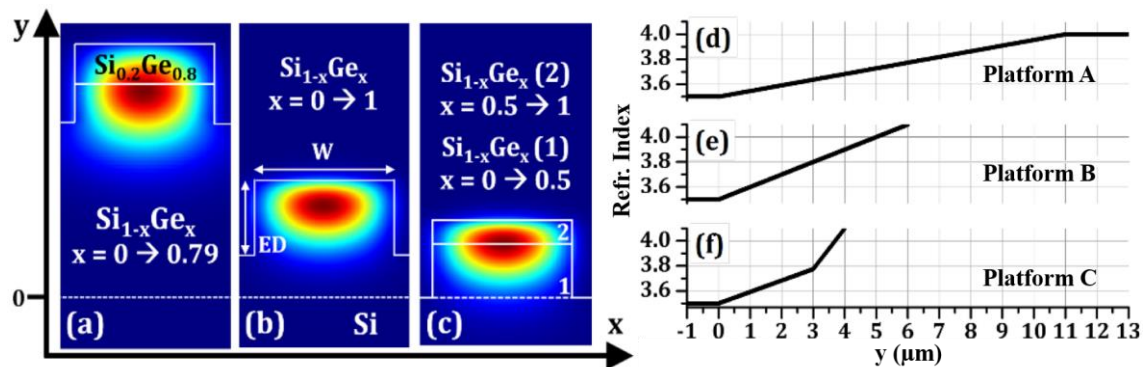


Fig.2.1.1. Waveguide cross-section with their corresponding refractive index profiles along the vertical direction for platform A (a,d), platform B (b,e) and platform C (c,f).

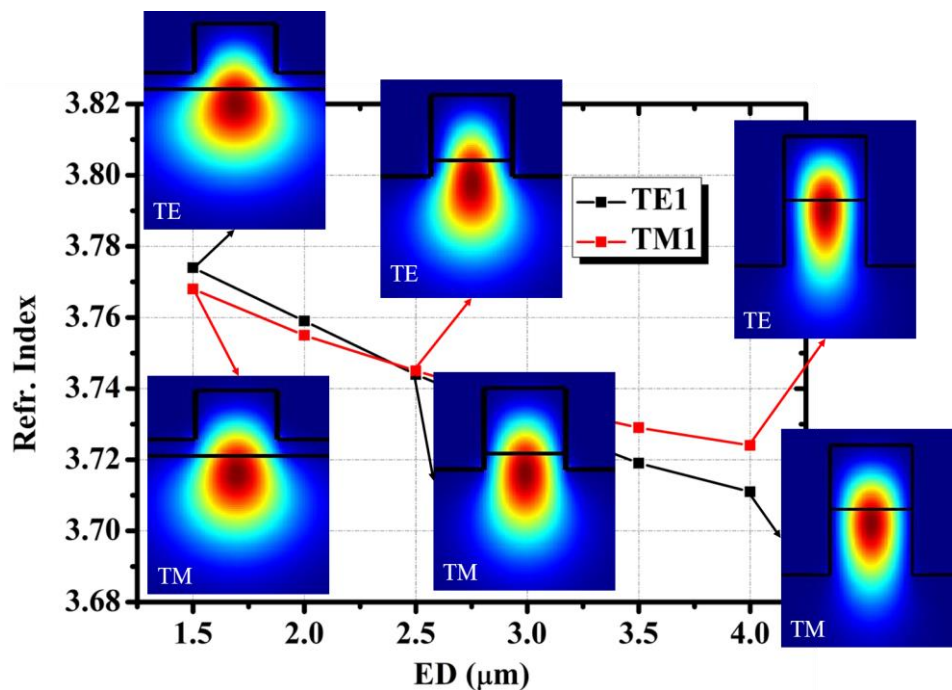


Fig.2.1.2. Effective index evolution as a function of etch depth for different modes guided in a 4- $\mu\text{m}$ -width waveguide at 7.5  $\mu\text{m}$  based on platform A.

Mode calculations have been done to evaluate mode confinement properties at 7.5  $\mu\text{m}$  wavelength. A finite difference eigenmode (FDE) method using a commercial software *Mode solution* is used [65]. As can be observed in Fig.2.1.2, for ED = 1.5  $\mu\text{m}$ , the guided

mode expands a lot in the buffer layer and mode confinement is poor. Interestingly the confinement increases when ED increases, and an etching depth  $ED = 4 \mu\text{m}$  is chosen, in order to benefit from strong light confinement.

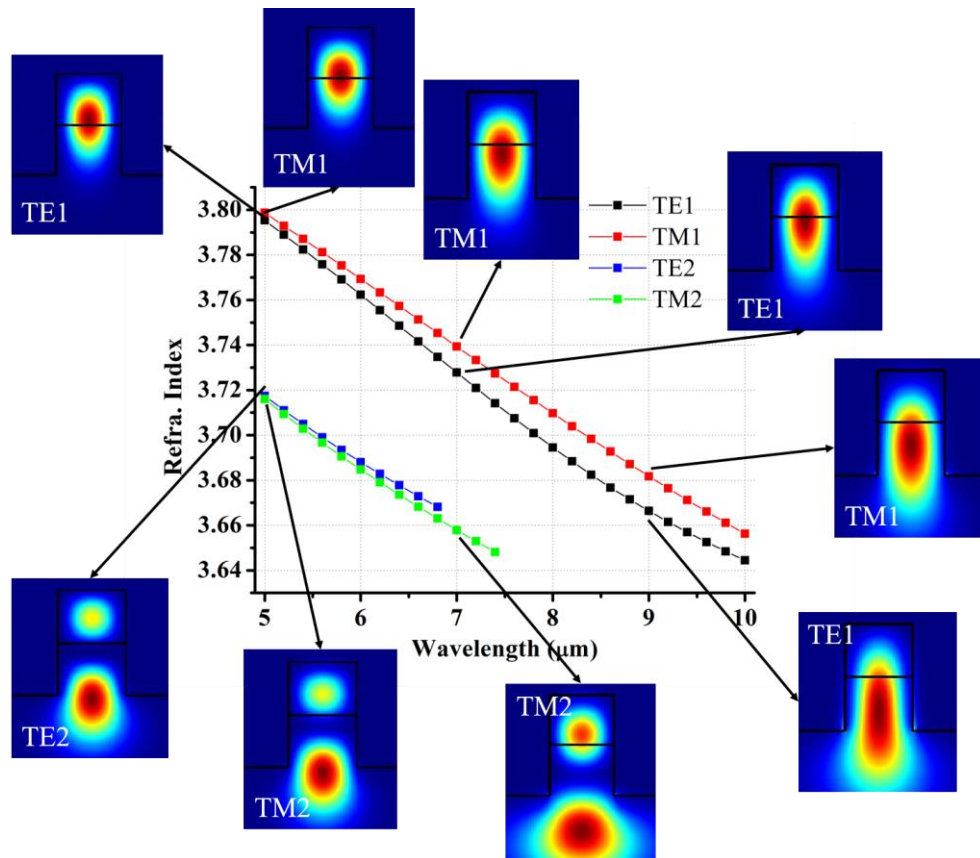


Fig.2.1.3. Effective index evolution as a function of wavelength for different modes guided in a 4- $\mu\text{m}$ -width waveguide based on platform A.

[Fig.2.1.3](#) presents the simulation results of the effective index evolution as a function of the wavelength for different modes guided in a 4- $\mu\text{m}$ -wide waveguide. As presented, the variation of the mode effective index and of the mode profiles are very small while varying the operation wavelength (the effective index variation of the fundamental mode is below 0.2 between 5 and 10  $\mu\text{m}$  wavelength). This is a clear evidence that the structure will provides low dispersion resulting in wide bandwidth operation. The waveguide design thus shows theoretically broadband operation with a cut-off wavelength at 11  $\mu\text{m}$  for TE mode and at 12.5  $\mu\text{m}$  for TM mode. Moreover, waveguide based on platform A with 4- $\mu\text{m}$ -width and 4- $\mu\text{m}$ -etch depth is single mode while operating at a wavelength larger than 7  $\mu\text{m}$  for

transverse electric (TE) polarization and larger than  $7.5 \mu\text{m}$  for transverse magnetic (TM) polarization. Interestingly we will see in the following that the multimode behavior at wavelength below  $7 \mu\text{m}$  is not prejudicial, as the higher order modes composed of two vertically separated lobes are poorly excited. Then the impact of the waveguide width on the effective index has also been calculated. As shown in [Fig2.1.4](#) the effective index of the guided modes increases when the waveguide width increases, and higher order modes appear when the waveguide width is increased.

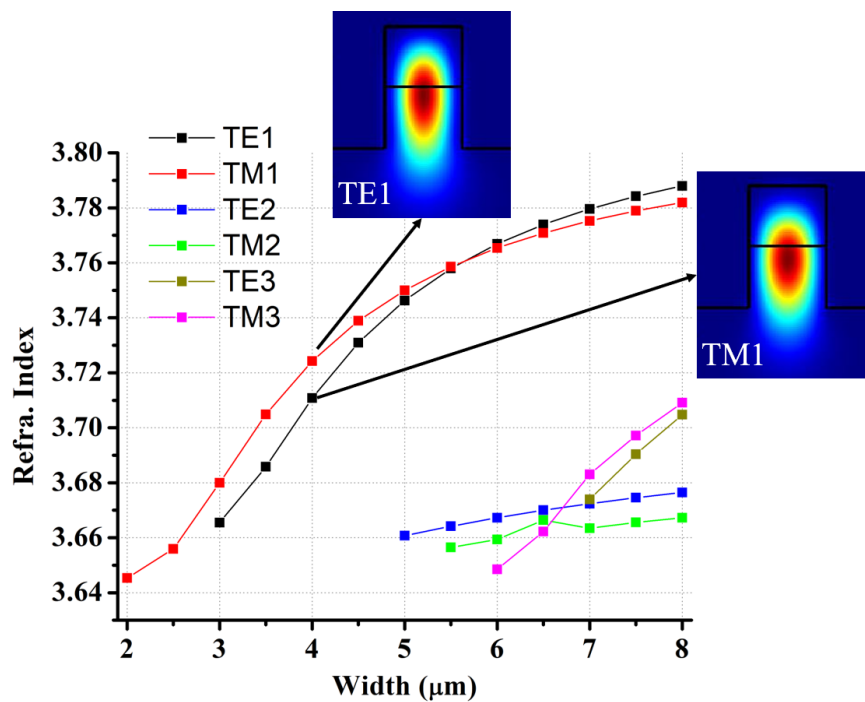


Fig.2.1.4. Evolution of effective index at  $7.5 \mu\text{m}$  wavelength as a function of waveguide width for different guided modes in a waveguide based on platform A.

To go further, an increase of the index contrast to obtain higher light confinement, for example to decrease waveguide bending radius, is highly desirable. Thus two other graded  $\text{Si}_{1-x}\text{Ge}_x$  platforms are proposed, aiming at decreasing the waveguide thickness, and increasing the slope of the refractive index gradient (see [Fig.2.1.1](#)). In this case, a compromise in the optimal thickness is expected. Indeed the thickness of the graded layer cannot be too thin, otherwise the waveguide propagation loss could increase due to in one hand the overlap of the guided mode with bottom Si substrate, and in the other hand possible

high TDD occurred during the material growth. Finally, as these new designs specifically target operation in the MIR, gradient up to pure Ge can now be used which is favorable for high refractive index and large transparency spectral range.

Therefore, the second platform (platform B) uses a 6- $\mu\text{m}$ -thick graded layer where Ge concentration is linearly increased from 0 (pure Si) to 100% (pure Ge) without any constant composition layer (see Fig.2.1.1) In this case, the electromagnetic mode propagates directly in the graded layer. The vertical refractive index profile varies from 3.5 ( $n_{Si}$ ) to 4.1 ( $n_{Ge}$ ) within 6  $\mu\text{m}$ , it thus yields higher vertical confinement due to a steeper index profile comparing to the platform A. Then, on purpose of further improving the light confinement, profiting the high nonlinearity of Ge and verifying how compact the graded-index  $\text{Si}_{1-x}\text{Ge}_x$  platform can achieve, a third platform (platform C) with an even more compact stack is designed. In order to confine light as far as possible from the Si substrate in the Ge-rich part, instead of one single graded layer as platform B, two graded layers for a total thickness of 4  $\mu\text{m}$  is designed. In this case, a 3- $\mu\text{m}$ -thick layer is grown with an increasing Ge concentration in the growth direction from 0 (pure Si) to 50% ( $\text{Si}_{0.5}\text{Ge}_{0.5}$ ), then followed by a second 1- $\mu\text{m}$  thick graded layer with Ge concentration starting from 50% up to 100% (pure Ge) (see Fig.2.1.1).

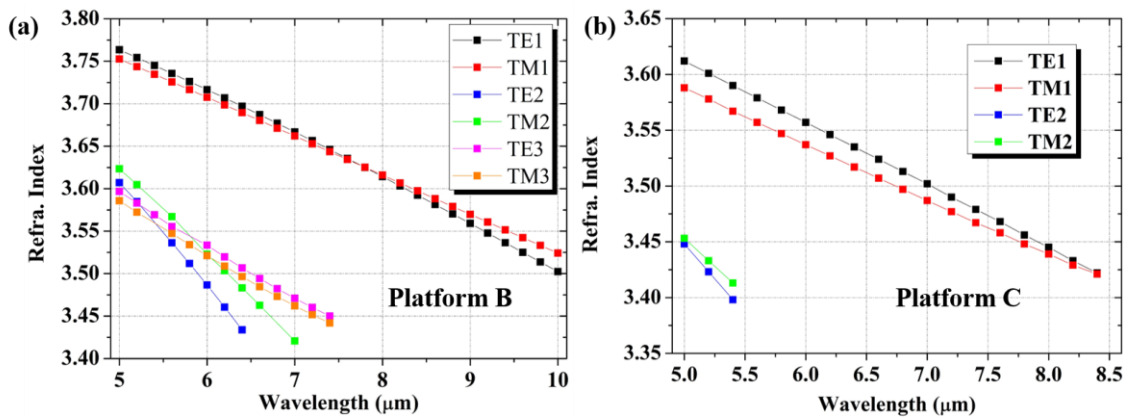


Fig.2.1.5. Effective index evolution of guided modes as a function of wavelength in a 4- $\mu\text{m}$ -width waveguide for (a) platform B and (b) platform C.

Mode calculations for platform B and C are reported in Fig2.1.5 where the effective index is reported as a function of wavelength. As can be observed, both platforms provide low dispersion which allows broadband operation. The single mode condition is obtained

for a wavelength larger than 7.5  $\mu\text{m}$  (platform B) and 5.5  $\mu\text{m}$  (platform C). Moreover, waveguide based on platform C shows a cut-off wavelength at 8.5  $\mu\text{m}$  where the effective index of guided mode is almost equal to the Si substrate.

Furthermore, since the silicon shows high absorption at large wavelength after 8  $\mu\text{m}$  as shown in [Fig.1.3.2](#), the overlap factor between the fundamental guided mode and the Si substrate has been calculated in order to predict in one way the waveguide propagation loss due to the material absorption at large wavelength. For the waveguide based on platform A, the overlap factor of the guided mode with the Si substrate is less than  $10^{-7}$  over the whole simulated wavelength range from 5.2 to 8.5  $\mu\text{m}$ . The simulation results for platform B and C are shown in [Fig.2.1.6](#). Using platform B, for wavelength below 7.5  $\mu\text{m}$ , the overlap between the guided mode and the Si substrate is less than 0.02%. However, it increases a lot for the waveguides based on the platform C. This calculation indicates that waveguides based on platform C can suffer from higher propagation loss due to the substrate absorption at large wavelength.

After the theoretical study of waveguides based on different platforms, to illustrate experimentally the waveguide properties, I designed an optical mask including spiral waveguides with different waveguide widths ( $W_{\text{WG}} = 4, 5, 6 \mu\text{m}$ ) and lengths ( $L = 0.6, 4.2, 6.1, 8.3, 10.4 \text{ cm}$ ). Thus, it is possible to measure precisely the propagation losses using a non-destructive cut-back method. The main difficulty of fabricating designed MIR  $\text{Si}_{1-x}\text{Ge}_x$  waveguides is to properly etch 4  $\mu\text{m}$  deep the waveguide with a smooth sidewall, otherwise the waveguide propagation would be high. Identical waveguides have been fabricated using the same fabrication process based on the 3 different platforms A, B and C to compare their performance. Details about waveguide fabrication are discussed in the next section.

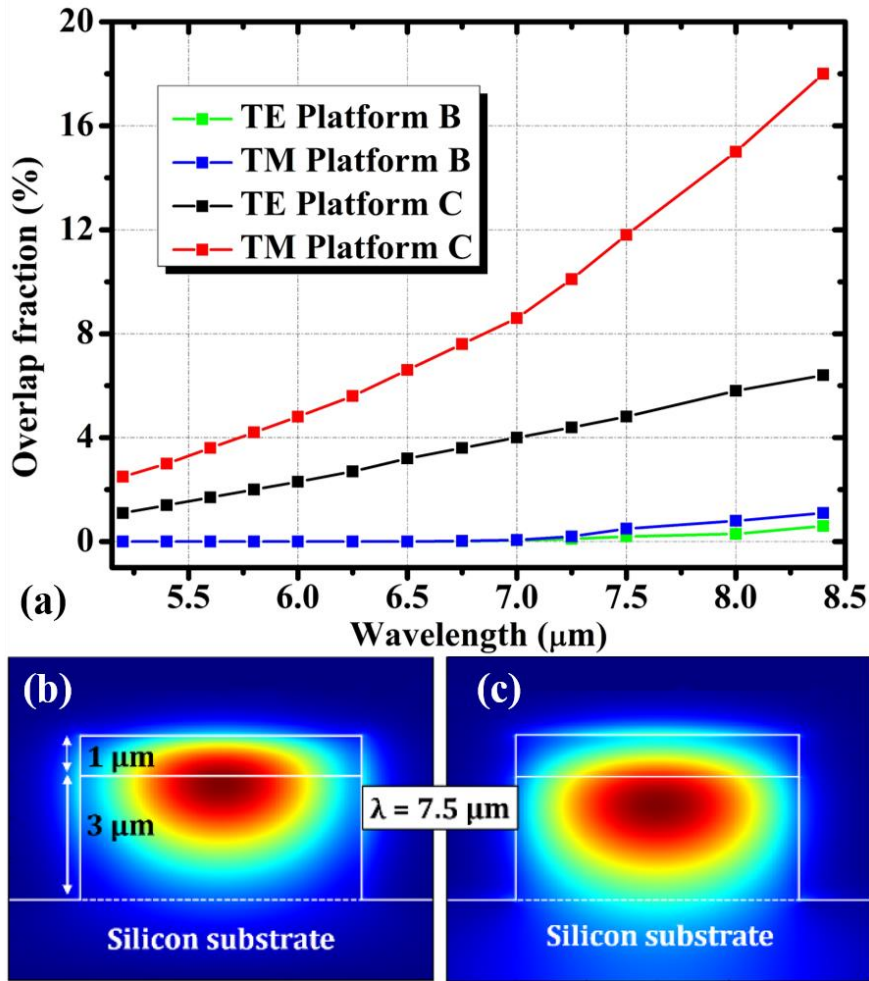


Fig.2.1.6. (a) Simulated overlap factor of the guided mode with silicon substrate; Simulated optical mode confinement at  $7.5 \mu\text{m}$  in platform C for (b) TE and (c) TM polarizations.

## 2.2. Waveguides fabrication

In this section, the fabrication process mainly in terms of optical lithography and inductively coupled plasma (ICP) etching is presented. The graded  $\text{Si}_{1-x}\text{Ge}_x$  wafers are epitaxially grown using low-energy plasma enhanced chemical vapor deposition (LEPECVD) by our collaborators in the Laboratory for Nanostructure Epitaxy and Spintronics on Silicon (L-NESS) in Italy in the group of Pr. Giovanni Isella. As an example of platform A, the Ge concentration is increased linearly from 0 to 0.79 along the growth direction over 11- $\mu\text{m}$ -thick with a growth rate of 5–10 nm/s. Then a 2- $\mu\text{m}$ -thick  $\text{Si}_{0.2}\text{Ge}_{0.8}$  guiding core layer is grown on top. With such an approach, the lattice parameter is gradually

accommodated, thus leading to the typical threading dislocation density (TDD) of  $3 \times 10^6 \text{ cm}^{-2}$  and 3.5 nm rms roughness [66].

Comparing to the previous work in  $\text{Si}_{1-x}\text{Ge}_x$  [64], instead of 1.5  $\mu\text{m}$  etch depth, new waveguide design requires 4  $\mu\text{m}$  etching depth which is challenging for fabrication. A vertical profile of photoresist is the key point to properly etch 4  $\mu\text{m}$  deep the waveguides. It can be done by well-controlled lithography and development. The fabrication flow is presented in [Fig.2.2.1](#).

Once we received the optical mask and  $\text{Si}_{1-x}\text{Ge}_x$  wafers, spiral waveguides have been fabricated on three platforms A, B and C. The  $\text{Si}_{1-x}\text{Ge}_x$  wafers are firstly cleaned 10 mins with acetone and then with isopropanol using an ultrasound cleaning machine, to strictly clean the sample surface. Then, a positive photoresist UVIII is deposited upon the sample surface. The UVIII is spin coated on the sample surface with a speed of 1000 rpm, followed by 3 mins annealing at 130  $^\circ\text{C}$ . A photoresist layer of about 1.2- $\mu\text{m}$ -thick is obtained. The waveguide patterns are defined by optical lithography using manual mask aligner MJB4.

After the illumination of photoresist, a second annealing at 140  $^\circ\text{C}$  is performed to amplify the dose applied into the photoresist before development with MF-CD-26 developer. Once the development has been done, the SiGe samples are etched by ICP etching (ICP-SPTS), then followed by a chemical wet etch with  $\text{H}_2\text{O}_2$  to smooth sidewall roughness produced during the ICP process. The used ICP etching, which is anisotropic, is performed by a combination of two different gas:  $\text{C}_4\text{F}_8$  and  $\text{SF}_6$  where  $\text{SF}_6$  is used to etch the  $\text{Si}_{1-x}\text{Ge}_x$  material, and  $\text{C}_4\text{F}_8$  is to passivate the etch flanks. The anisotropy of the etching is reinforced by the formation of polymer on the flanks. The etching speed is controlled by the ratio between two gas.

Finally, the waveguide facets are defined by mechanic dicing performed inside the access waveguide using a diamond blade with a fine grain. This optimized dicing process gives us a reproducible waveguide facet with similar coupling condition. At the end, the photoresist is removed by acetone and isopropanol. Representative optical microscope images are shown in [Fig 2.2.2](#).

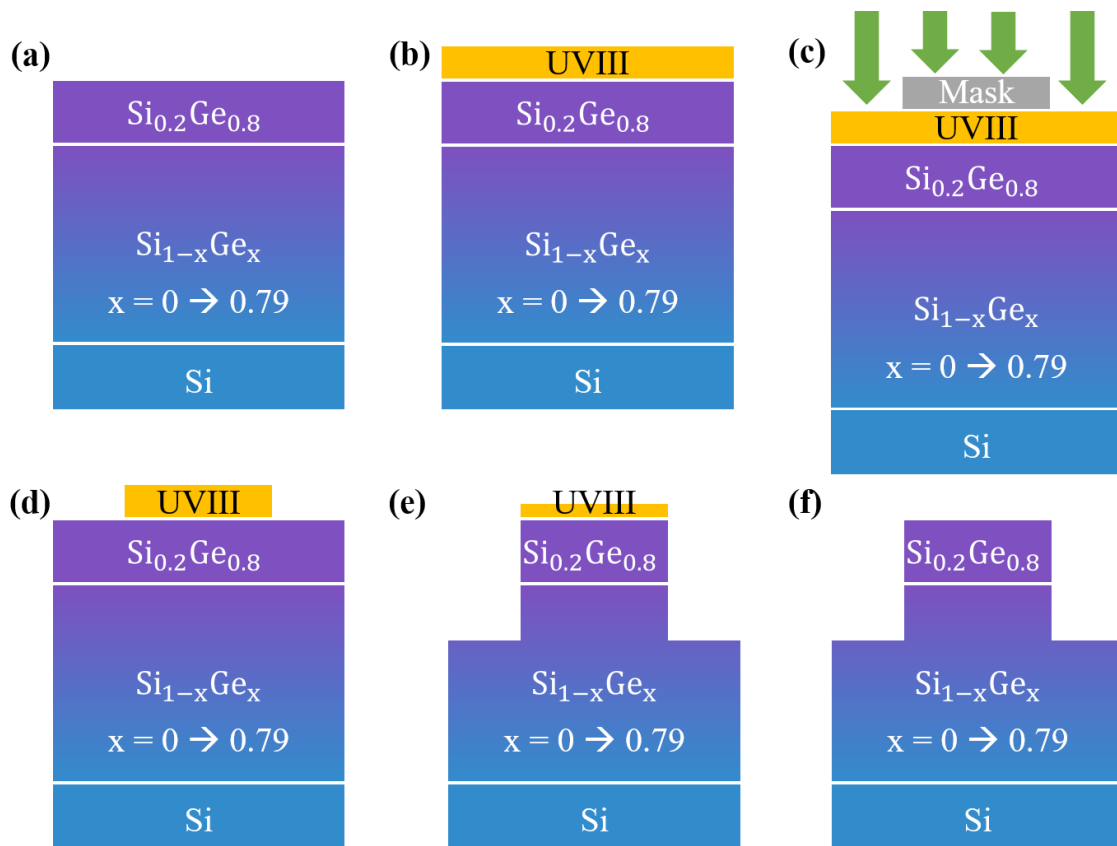


Fig.2.2.1. (a) sample surface cleaning; (b) deposition of photoresist; (c) optical lithography; (d) development; (e) waveguide etching; (f) remove of residual of photoresist.

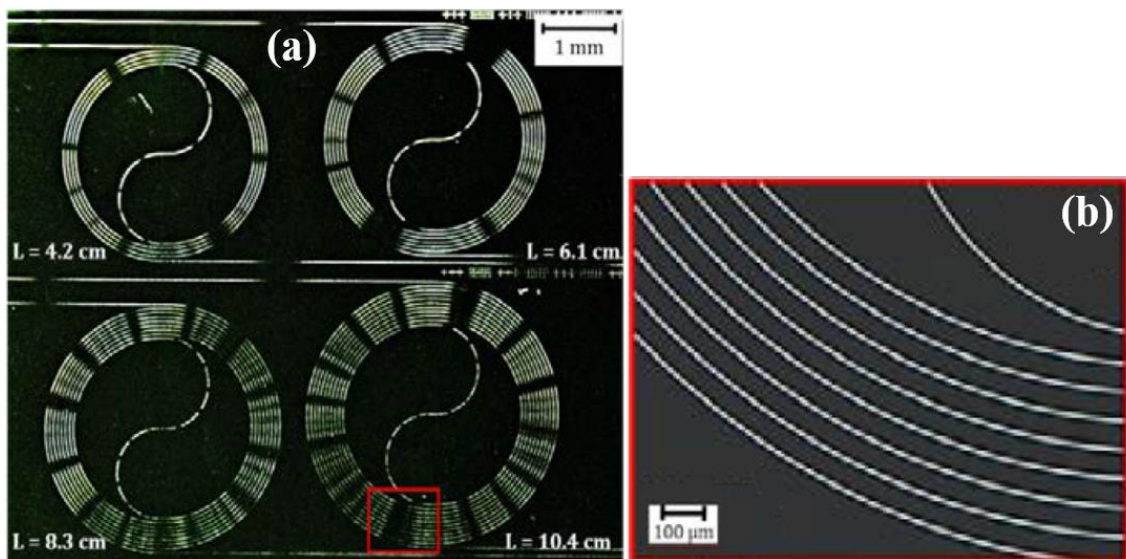


Fig.2.2.2. (a) Optical microscopic top view of the fabricated  $\text{Si}_{1-x}\text{Ge}_x$  spiral waveguides; (b) Magnified region of a single spiral waveguide corresponding to the red square area depicted in (a).

## 2.3. Characterization

After the fabrication of the photonic circuits comprising the spiral waveguides, the fabricated samples have been characterized using a free-space configuration set-up. In this section, the experiment and characterization results for the study of waveguide properties in terms of propagation losses and coupling losses will be presented. The measurements have been performed in collaboration with Joan Manel Ram íez, post-doctor who built the experimental set-up.

### 2.3.1. Description of experimental set-up

The mid infrared characterization set-up uses an ad hoc free-space configuration as shown in [Fig.2.3.1](#).

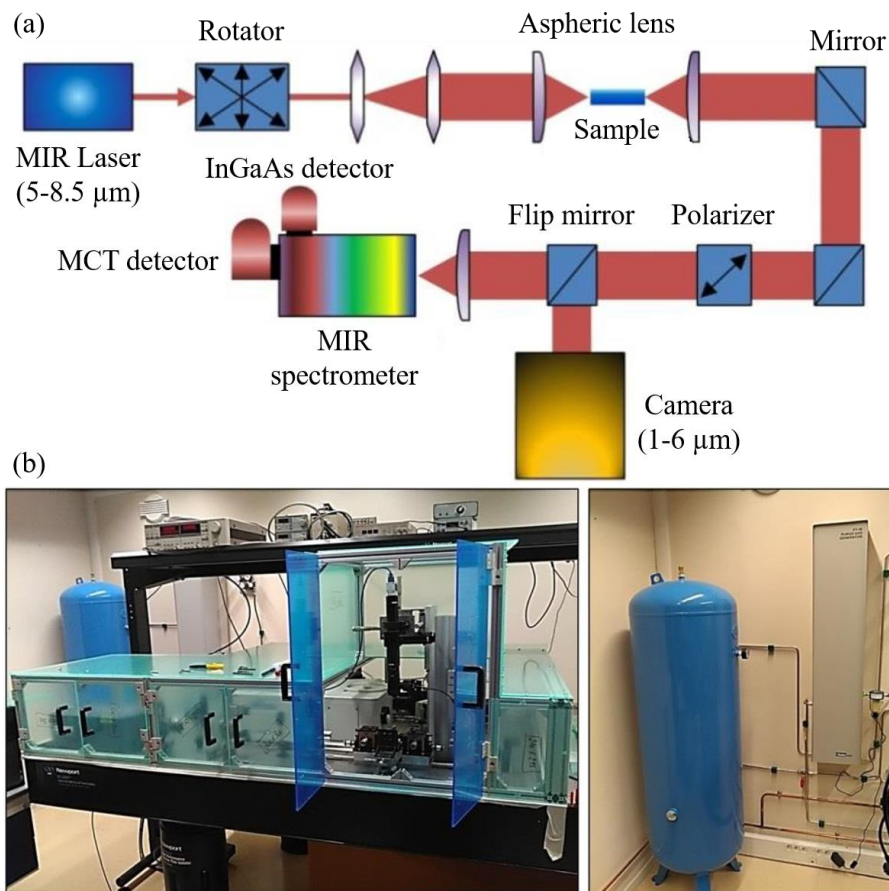


Fig.2.3.1. (a) Schematic image of the MIR characterization set-up; (b) Image of MIR set-up covered by isolation box (left), and the dry air pump system (right).

The MIR laser is a MIRCAT tunable quantum cascaded laser (QCL) with an external cavity operating in pulse regime with a duty cycle of 5% and a repetition rate of 100 kHz. The laser which contains three laser chips, emitting in TM polarization provides a tunable wavelength range from about 5  $\mu\text{m}$  ( $2000\text{ cm}^{-1}$ ) to 8.5  $\mu\text{m}$  ( $\sim 1170\text{ cm}^{-1}$ ) with a maximum peak power of 300 mW at 6.5  $\mu\text{m}$  and a wavelength accuracy lower than  $1\text{ cm}^{-1}$  (below 6.5 nm) [67]. A polarization rotator is installed at the output of the laser while measuring in TE polarization. Then using the aspheric ZnSe lens, light is butt coupled into and out from the sample. To facilitate this coupling, the width of the waveguides at the chip input and output are 50  $\mu\text{m}$ . They are followed by 1.2 mm-long tapers to reach the targeted width, typically 5  $\mu\text{m}$ . The collected optical signal propagates through a polarization filter to discard any polarization rotation throughout the sample. The signal is then sent to either a MIR camera or a spectrometer with an MCT HgCdTe photodetector. The MIR camera is available from 1 to 5.5  $\mu\text{m}$  allowing us to observe the mode profile coupled out of the sample, to ensure the fundamental mode coupling. Finally, the detected signal is recorded through a lock-in amplifier. The full optical path is installed inside an isolation box connected to a dry air pump system which allows to reduce the impact of atmospheric absorption lines at different wavelengths (mainly the H<sub>2</sub>O absorption).

### 2.3.2. Experimental results

The spiral waveguides on three platforms have been measured at a wavelength range from 5.5  $\mu\text{m}$  to 8.5  $\mu\text{m}$  in a step of 4 nm. [Fig.2.3.2](#) shows a representative measured transmission of 5- $\mu\text{m}$ -width waveguides based on platform A and the laser response without sample. The drops at 5.8  $\mu\text{m}$  and 7  $\mu\text{m}$  correspond to the changes of laser chip during the wavelength-scan measurement. Moreover, drop lines in a wavelength range from 5.5  $\mu\text{m}$  to 7  $\mu\text{m}$  are corresponding to the atmospheric absorption lines of other components in air and some residual H<sub>2</sub>O due to the non-perfect isolation of the optical path.

Waveguide propagation losses and coupling losses have been characterized using the cut-back technique. [Fig.2.3.3\(a\)](#) shows a representative cut-back measurement of the spiral waveguides on the three platforms in quasi-TE polarization at 7.5  $\mu\text{m}$ . As can be observed, the recorded transmittance decreases linearly with the waveguide length, whose slope

represents the waveguide propagation losses, and the intercept at  $L = 0$  can be directly correlated to the coupling losses. Coupling losses of 9.5 dB/facet, 4.5 dB/facet and 8.6 dB/facet at 7.5  $\mu\text{m}$  are obtained for platform A, B and C respectively. Different coupling condition can be predicted by different index profile at the waveguide facet of each platform.

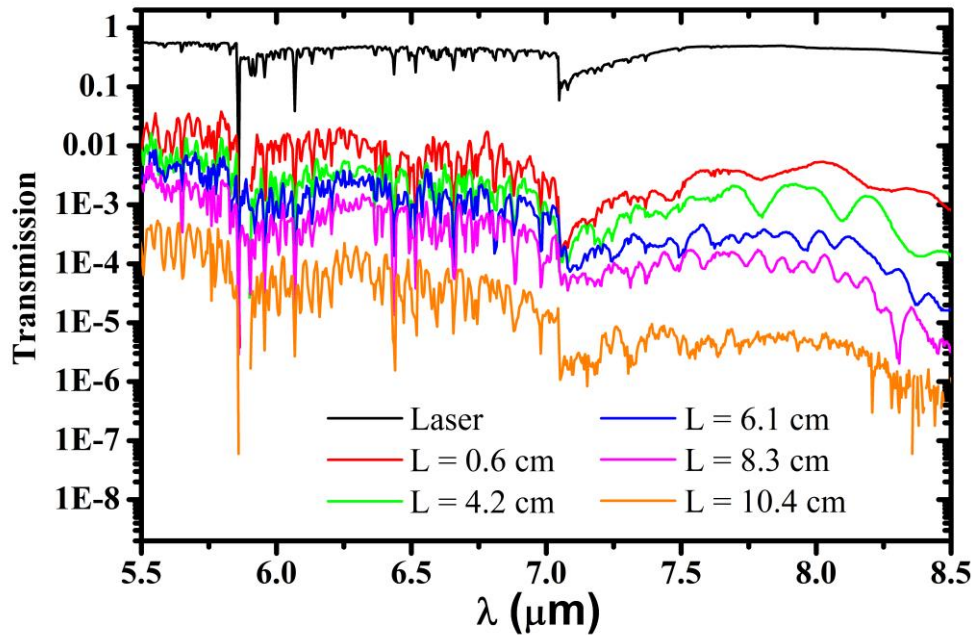


Fig.2.3.2. Measured transmission of 5- $\mu\text{m}$ -width waveguides based on platform A (colored lines) and the laser response without sample (black line).

This cut-back method has been performed to calculate the propagation losses at different wavelengths from 5.5  $\mu\text{m}$  to 8.5  $\mu\text{m}$  for both TE and TM polarizations measurements. [Fig.2.3.3\(b-d\)](#) show the waveguide propagation losses of each platform for both TE/TM polarizations. As shown, broadband low-loss ( $\leq 3$  dB/cm) performance is achieved for platform A and B in both polarizations with a nearly negligible wavelength dependency. On another hand, the platform C presents high loss up to 10 dB/cm at 8  $\mu\text{m}$  in TE polarization. In TM polarization, propagation loss increases continuously as a function of operation wavelength which is corresponding to the theoretical prediction. Similar values of waveguide propagation losses have been obtained for waveguides with different widths ( $W_{\text{WG}} = 4, 5$   $\mu\text{m}$ ). However, mode beating has been observed for 6- $\mu\text{m}$ -width waveguides which are highly multimode.

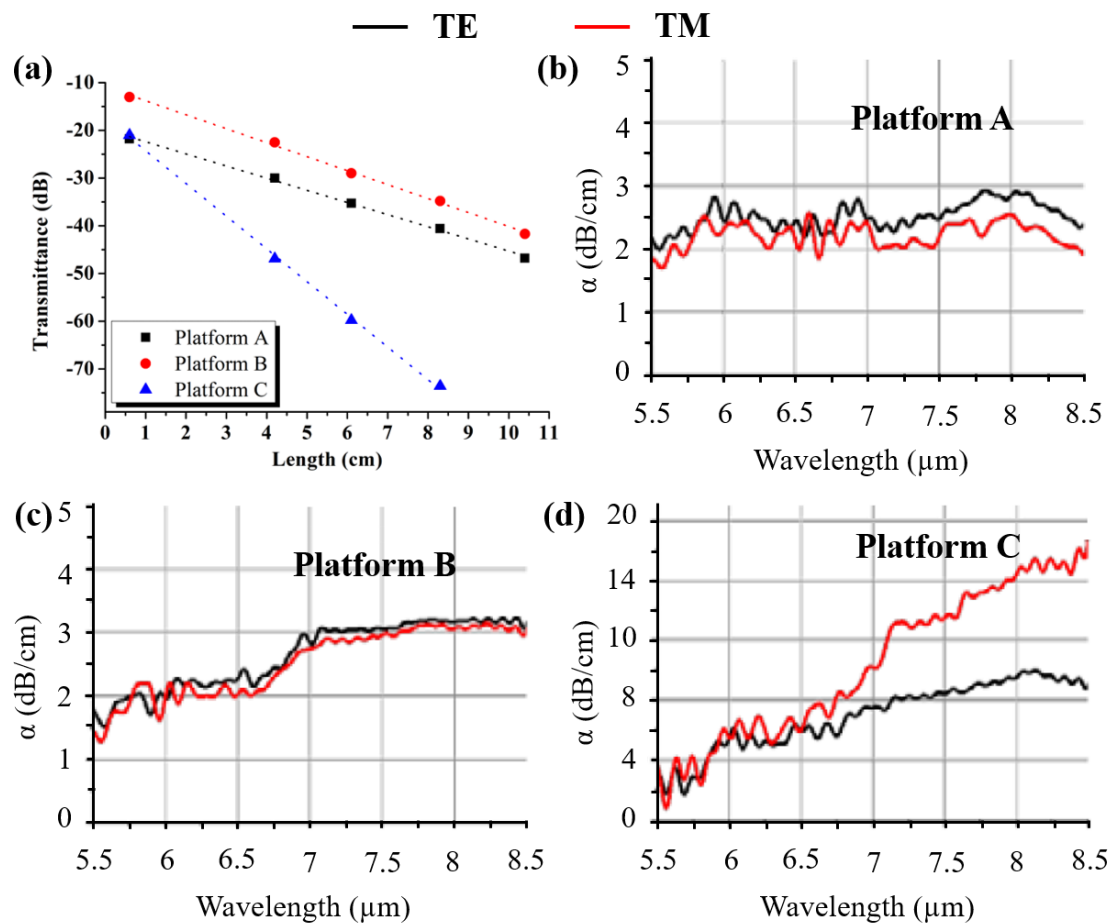


Fig.2.3.3. (a) Transmittance as a function of waveguide length for quasi-TE polarization at 7.5  $\mu\text{m}$ , dashed colored lines are linear fits of the data; (b)-(d) Measured propagation loss from 5.5 to 8.5  $\mu\text{m}$  for platform A, B and C [68].

## 2.4. Study of sensing capability of $\text{Si}_{1-x}\text{Ge}_x$ waveguides

The determination of broadband low-loss waveguide based on platforms A and B provides a good starting point for the demonstration of on-chip integrated circuits. After the evaluation of waveguide properties, the sensing capability of  $\text{Si}_{1-x}\text{Ge}_x$  waveguides using evanescent field absorption can be evaluated.

### Theoretical study of sensing capability

A theoretical evaluation of sensing capability of such graded-index  $\text{Si}_{1-x}\text{Ge}_x$  waveguides using evanescent field absorption has been done by means of evaluating the field overlap of

the guided mode with the waveguide upper cladding. In the theoretical calculation, “no-cladding” ( $n_{\text{clad}} = n_{\text{air}} = 1$ ) corresponds to the scenario of gas-trace sensing, i.e. methane ( $\text{CH}_4$ ), and “with cladding” (a refractive index  $n \sim 1.6$  is used in this calculation) corresponds to a liquid-phase analyte sensing.

As can be observed in [Fig.2.4.1](#), the power fraction increases as a function of wavelength. Comparing the simulated power fraction of guided mode in the upper cladding for waveguides based on three  $\text{Si}_{1-x}\text{Ge}_x$  materials, waveguide on platform B and platform C have better performance than waveguide on platform A. Then considering the possible high propagation loss in platform C, graded-index  $\text{Si}_{1-x}\text{Ge}_x$  waveguides based on platform B would show best performance for evanescent field sensing in this wavelength range.

To further discuss the potential of  $\text{Si}_{1-x}\text{Ge}_x$  waveguides for the application of gas-trace sensing, the detection limit in terms of the minimum detectable analyte concentration has been estimated. As an example, the possibility of using  $\text{Si}_{1-x}\text{Ge}_x$  to detect the presence of methane ( $\text{CH}_4$ ), which is well known as one of the key roles in global warming [69] is considered.  $\text{CH}_4$  presents a strong absorption line at  $\lambda = 7.7 \mu\text{m}$  [12]. Considering a waveguide length  $L$  and propagation loss  $\alpha$ , the change of transmitted light intensity  $\Delta I$  affected by the presence of analyte can be calculated by [27]:

$$\Delta I = \exp(-\alpha L) [1 - \exp(-\Gamma \alpha' L)] \approx \exp(-\alpha L) \Gamma \alpha' L \quad (1)$$

where  $\alpha'$  is the absorption coefficient of the analyte and  $\Gamma$  is the overlap factor of guided mode in the air (gas-phase analyte). The optimum waveguide length which yields the maximum detectable optical attenuation providing an optimum sensitivity can be given by:

$$\frac{\partial \Delta I}{\partial L} = 0 \Rightarrow L = \frac{1}{\alpha} \quad (2)$$

The optimum waveguide length can be obtained as  $L \approx 1.45 \text{ cm}$  considering the typical waveguide loss  $\alpha = 3 \text{ dB/cm}$ . The minimum detectable concentration is then given by the following equation:

$$C_{\min} = \frac{-\ln \left[ 1 - \frac{\Delta P_{\min-\text{detec}}}{P_0 \exp(-\alpha L)} \right]}{\epsilon \Gamma L} \quad (3)$$

where  $\Delta P_{\text{min-detec}}$  is the minimum detectable variation of optical power of the detection system, and  $\varepsilon$  is the molar absorption of analyte, which is equal to  $174 \text{ L mol}^{-1}\text{cm}^{-1}$  for methane. Considering the used detector in our experimental set-up, a DSS-MCT14 020L photodetector from Horiba with a NEP of  $5.10^{-12} \text{ W/Hz}^{1/2}$ , a signal to noise ratio of 10 and an averaging time of 0.1 ms, the minimum detectable power can be calculated as 3.5 nW. Thus, considering the overlap factor of 0.3% (TE mode, Platform A, [Fig.2.4.1\(a\)](#)) and 0.72% (TE mode, Platform B, [Fig.2.4.1\(b\)](#)), the minimum detectable concentration  $\text{CH}_4$  is around  $1.2 \times 10^{-5} \text{ mol L}^{-1}$  (Platform A) and  $5.3 \times 10^{-6} \text{ mol L}^{-1}$  (Platform B). It corresponds to 293 ppm (Platform A) and 130 ppm (Platform B) lower than the occupational exposure limit of 1000 ppm recommended by the international environmental standards [70].

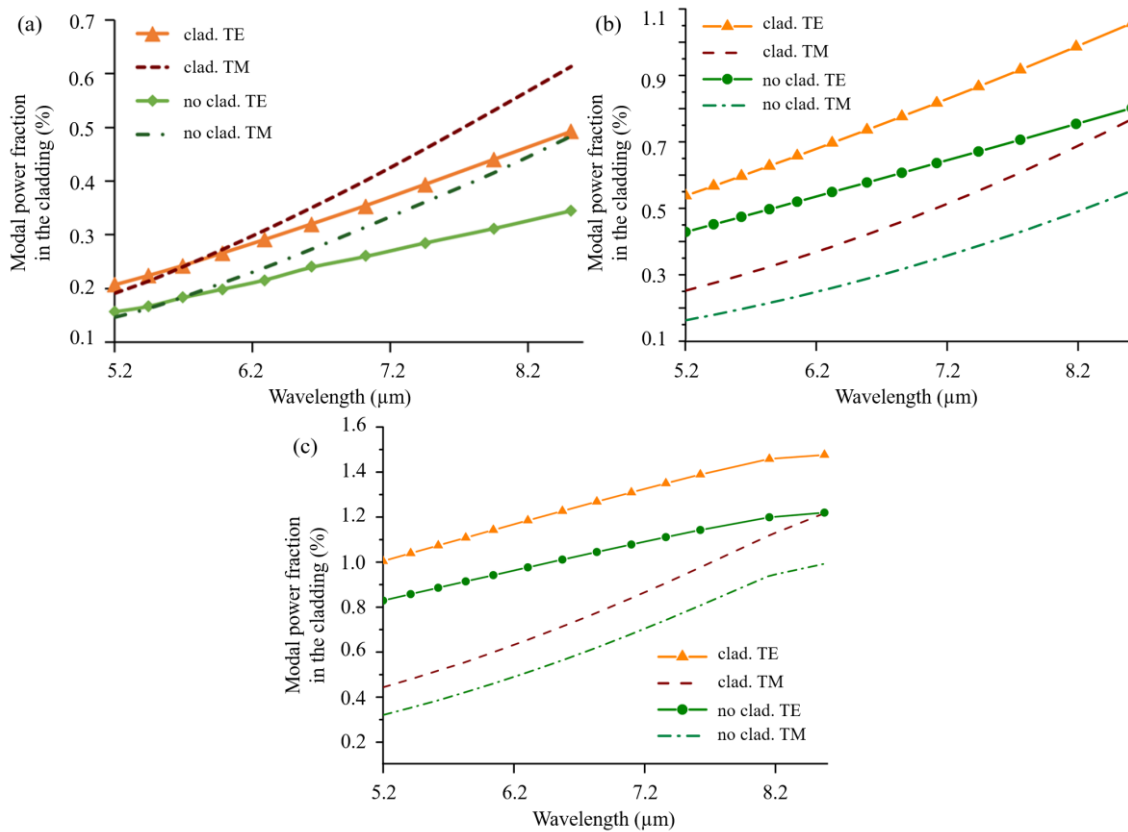


Fig.2.4.1. Simulated overlap factor of guided mode with and without upper cladding for (a) Platform A; (b) Platform B and (c) Platform C.

## Experimental demonstration of sensing capability

Considering the requirement of an additional gas-supply microfluidic system for sensing experiment of gas detection, a simple approach is performed for the first proof of concept. A cladding layer of photoresist S1818 ( $n \sim 1.6$ ) which can be easily found in our laboratory is used. The S1818 is a positive photoresist which is widely used for optical lithography in the micro/nano fabrication. It contains mainly propylene glycol monomethyl ether acetate ( $C_6H_{12}O_3$ ) polymer and Mixed cresol novolak resin [71]. The first one consists with the chemical bonds of C-C (absorption between 6.6-16.7  $\mu\text{m}$ ), C-O (absorption between 7.7-10  $\mu\text{m}$ ) and C=O (absorption between 5.7-5.9  $\mu\text{m}$ ) [72]. The last one consists with the chemical bonds of C-C, C-O and the structure of benzene (absorption between 5.9-6.5  $\mu\text{m}$ ) [73]. [Fig.2.4.2](#) shows the absorption band of different chemical bonds in the mid infrared.

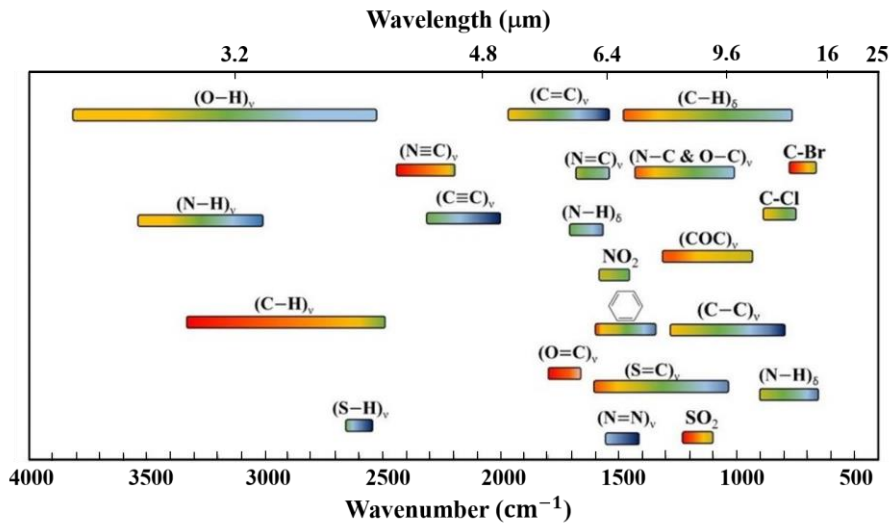


Fig.2.4.2. Absorption band of different chemical bonds, readapted from [73].

To evaluate the absorption of the evanescent component of the guided mode, 1.8  $\mu\text{m}$ -thick S1818 photoresist has been spin coated on the spiral waveguides based on platform A. A schematic waveguide cross-section and the SEM image are presented in [Fig.2.4.3](#). The SEM image of waveguide confirms that the waveguide is fully covered by the photoresist. The evanescent field of guided mode thus interacts with the photoresist cladding, resulting in a wavelength-dependent absorption. Transmission measurement of waveguide with photoresist cladding has been performed to compare with previous measurement without

cladding. Raw transmission measurements of spiral waveguides between 5.2 and 7  $\mu\text{m}$  for different lengths are shown in [Fig.2.4.4](#).

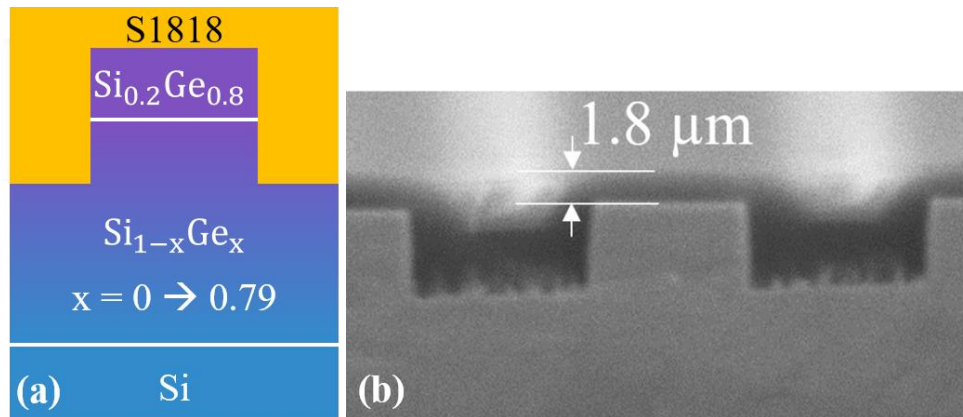


Fig.2.4.3. (a) Schematic cross-section of the waveguide; (b) SEM image of the waveguide presenting 1.8  $\mu\text{m}$  thick photoresist on top of the waveguide.

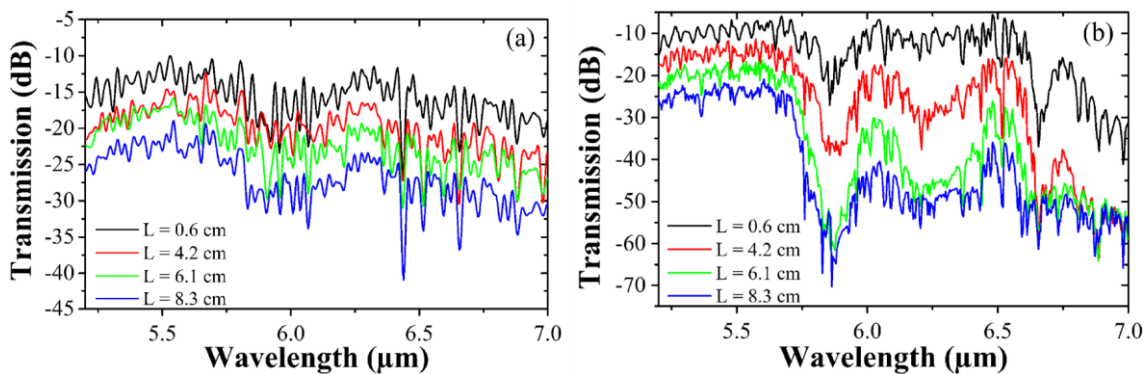


Fig.2.4.4. Raw transmission spectrums of the spiral waveguides of different lengths (normalized by the laser spectrum without sample) (a) without and (b) with photoresist cladding in TE polarization [74].

Transmission spectrum of all waveguides for wavelengths larger than 7  $\mu\text{m}$  are at the noise level of our set-up. It is due to the high absorption of the pre-mentioned chemical bonds at long wavelength. The cut-back method has also been applied to calculate the propagation losses with the presence of photoresist up to 7  $\mu\text{m}$ . [Fig.2.4.5\(a\)](#) shows the waveguide propagation losses with the presence of photoresist S1818 for both TE/TM polarizations. It is evident that we can observe the increased losses at wavelengths of 5.8  $\mu\text{m}$ , 6.25  $\mu\text{m}$  and after 6.5  $\mu\text{m}$ . The high losses at 5.8  $\mu\text{m}$  and 6.25  $\mu\text{m}$  are mainly corresponding to the absorption of chemical bonds of C=O and of benzene, respectively. Moreover, the

high loss for wavelength larger than 6.5  $\mu\text{m}$  (even larger than 7  $\mu\text{m}$ ) corresponds to the absorption of high concentration of C-C and C-O bonds in the photoresist S1818.

To verify the absorption coefficient of different chemical bonds of the photoresist, the transmission characteristics of the photoresist has been measured in a surface illumination configuration (a layer of photoresist on a Si wafer). Transmission of a Si wafer covered by 78- $\mu\text{m}$ -thick photoresist has been performed, and then normalized by the transmission of the Si wafer without photoresist.

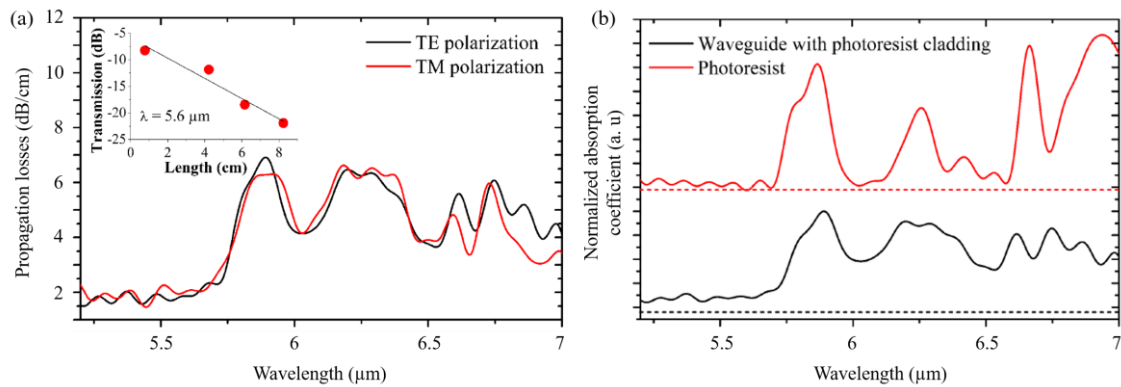


Fig.2.4.5. (a) Propagation losses of  $\text{Si}_{1-x}\text{Ge}_x$  waveguide covered by photoresist S1818 for TE and TM polarizations from 5.2 to 7  $\mu\text{m}$ , (inset) illustration of cut-back method at  $\lambda = 5.6 \mu\text{m}$ ; (b) Normalized absorption coefficient of the photoresist compared with the losses of waveguide (in TE polarization) covered by photoresist [74].

It has thus been possible to estimate the absorption of the photoresist, as reported in [Fig.2.4.5\(b\)](#). Interestingly, a very good correlation is obtained when comparing the spectral evolution of the photoresist absorption and the propagation losses of the waveguides with the photoresist cladding, proving that the increase of the propagation loss can be attributed to the absorption of the evanescent field by photoresist at certain wavelengths. The comparison of the waveguide propagation losses and the photoresist absorption coefficient at 6.25  $\mu\text{m}$  has then be used to calculate the overlap factor of the guided mode with the absorbing cladding. This overlap factor has thus been estimated to 0.16% for TE polarization and 0.17% for TM polarization. It is worth to note that this calculated overlap factors are a bit lower than the values obtained by simulation (0.29% and 0.3% respectively, see [Fig.2.4.1\(a\)](#)). The slight difference between experiment and simulation could be attributed to an over-estimation of absorption coefficient of the photoresist in the surface

illumination measurement where the Si wafer has been tilted about  $45^\circ$  to avoid direct reflection of laser signal back to QCL. An effective reduction of the estimated overlap factor may be occurred.

This experiment proves that the feasibility of using  $\text{Si}_{1-x}\text{Ge}_x$  waveguide to demonstrate evanescent field sensing circuits in the MIR range. Further improvement of the performance of the sensing circuits is also expected by implementing on-chip resonant structures. The demonstration of broadband MIR resonators will be presented in [Chapter 4](#).

## 2.5. Conclusion

In this chapter, the properties of MIR waveguide based on three  $\text{Si}_{1-x}\text{Ge}_x$  platforms and the sensing capability of such waveguide are discussed. In the first part, theoretical study of waveguide properties, in terms of effective index of guided mode, single mode condition, field overlap with Si substrate and upper cladding, are evaluated for the design of MIR broadband waveguide.

In a second part, the waveguides fabrication process mainly about lithography and ICP etching are presented. A main challenge of etching 4- $\mu\text{m}$ -deep while keep a low sidewall roughness is overcome. Waveguides with 5 different lengths ( $L = 0.6, 4.1, 6.1, 8.3, 10.4$  cm), 3 different widths ( $W_{WG} = 4, 5, 6$   $\mu\text{m}$ ) have been fabricated on all three  $\text{Si}_{1-x}\text{Ge}_x$  materials.

In the third part, fabricated waveguides are measured using a free-space configuration, obtaining low-loss broadband operation. A propagation loss less than 3 dB/cm over the whole measured wavelength range are obtained for waveguides based on platform A and B.

The last part is dedicated to the evaluation of sensing properties based on these MIR platforms. The feasibility of using graded-index  $\text{Si}_{1-x}\text{Ge}_x$  waveguide for applications of gas-trace sensing, as an example of  $\text{CH}_4$  are discussed. A theoretical minimum detectable concentration of  $\text{CH}_4$  is obtained as low as 130 ppm using the evanescent field absorption based on  $\text{Si}_{1-x}\text{Ge}_x$  waveguide. Then, as a proof of concept, a sensing experiment of detecting an optical photoresist S1818 is performed. The experimental results prove that the feasibility of graded-index  $\text{Si}_{1-x}\text{Ge}_x$  waveguide for further demonstration of high performance on chip sensing systems.

### 3. Periodic Waveguides

In the context of integrated optics, periodic waveguides are widely used for many applications, for example grating couplers are used for fiber to chip light coupling [75–79]. Moreover, waveguide Bragg gratings have been widely used for the demonstration of on-chip Fabry-Perot cavities for many applications such as sensing and laser source [80–82]. In both cases, the operation relies on the periodicity of the waveguide which creates periodicity of the effective index of the guided mode. By varying the period of the refractive index perturbation in a waveguide, three regimes can be achieved as shown in Fig.3.1.1 [83]: i) diffraction regime where light is radiated out of the waveguide. In this case the period is larger than half of the wavelength; this regime is used to couple light from the waveguide to a fiber on top of the photonics circuit. ii) Bragg reflection regime where light is back reflected inside the waveguide. The period is thus equal to half of the wavelength to achieve the Bragg condition. iii) Subwavelength regime where light is transmitted through the waveguide. In this case the period is less than half of the wavelength.

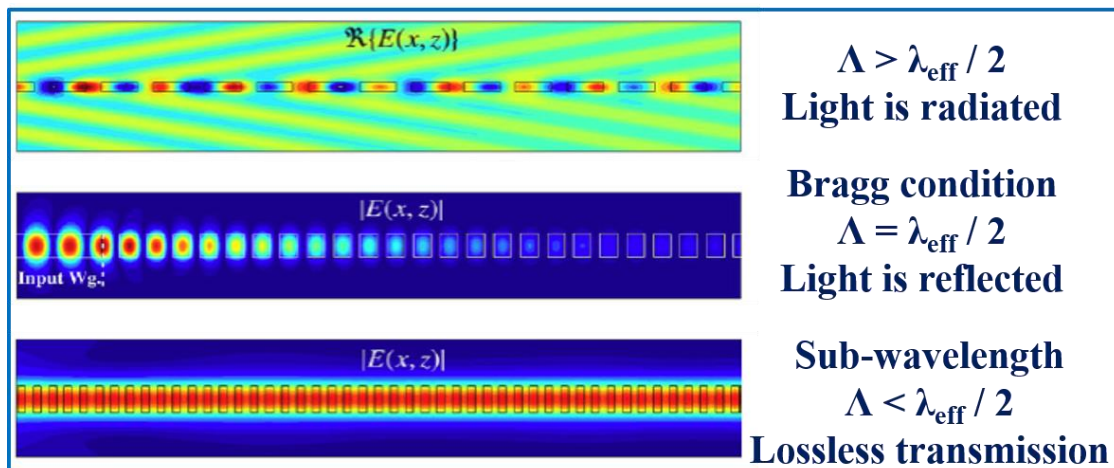


Fig.3.1.1. Light propagation through a periodic waveguide for three regimes, adapted from [83].

During this thesis, periodicity has been introduced in the MIR Ge-rich graded SiGe waveguides for two main applications: first to evaluate the possibility to couple light from the waveguide to a top fiber; then to demonstrate the first integrated Fabry-Perot cavities at MIR wavelength. The design of the MIR grating coupler is reported in [section 3.1](#). Grating

coupler for TE/TM polarization have been designed at a wavelength of 7.5  $\mu\text{m}$ . A -1-dB bandwidth of more than 300 nm is obtained for both polarizations. A coupling efficiency of -12 dB (-9 dB) is obtained for TE(TM) polarization. It can be further optimized by grating trench apodization. The second part of this chapter is then dedicated to the design, fabrication and characterization of Bragg reflectors integrated on the waveguide. Interestingly, operation is demonstrated in a wide range of MIR wavelength between 5.4  $\mu\text{m}$  and 8.4  $\mu\text{m}$  by simply modifying the period of Bragg grating. The use of these reflectors to demonstrate the first MIR Fabry-Perot cavities working at 8  $\mu\text{m}$  wavelength will be reported in the [chapter 4](#) of the manuscript.

### 3.1. MIR broadband grating couplers

There are two ways to couple light into a photonic integrated circuit, one is using the butt coupling where light is coupling from the edge of the sample normally through an adiabatic taper. In this way, it requires edge facet polishing for the fabrication to obtain an efficient coupling, and the in/output waveguides must be at the edge of the sample. Apart from these limitations, butt-coupling shows wide coupling bandwidth, and the operation of a butt-coupled PIC is generally limited by the bandwidth of other building blocks or the waveguide itself.

The second approach is coupling from the sample surface using the grating couplers which have been largely developed in NIR wavelength range. An example of grating couplers for light coupling at the sample surface from an optical fiber is presented in [Fig.3.1.2](#). This approach shows high tolerance to fabrication and alignment and reasonable to good coupling efficiency. Due to its flexibility of implementation anywhere on the chip and its high tolerance to alignment, grating couplers are interesting for complex systems and allow wafer-level characterization without chip dicing and facet preparation. . In terms of optical fiber, the classical silica fiber cannot be used in the mid-infrared range because of light absorption in this wavelength range. New approaches have thus been developed for MIR fiber, such as Chalcogenide glasses fiber, Germanate glasses fiber, heavy metal fluoride glasses (HMFG), sapphire fiber, photonic crystal fiber and others [84–88]. Most of them are still limited in short-wave infrared and are multimode fibers. In the

lab we did experiments with Chalcogenide-based photonic crystal single-mode fiber. The grating coupler has thus been designed for coupling light from chip to this type of fiber with a core diameter of 13  $\mu\text{m}$  [89].

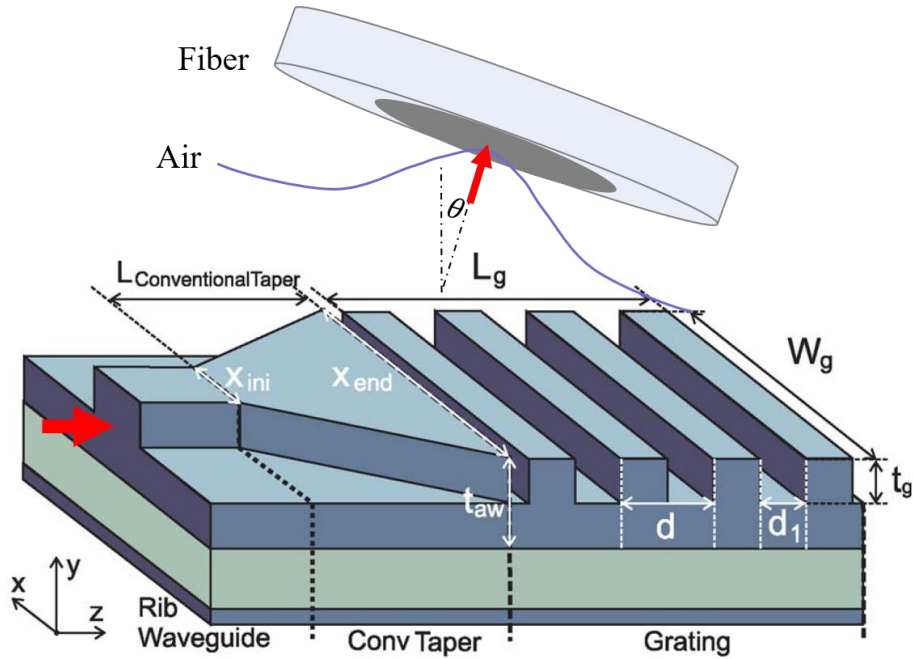


Fig.3.1.2. 3D schematic view of a grating coupler where light is coupled out from the waveguide to the optical fiber on top, readapted from Ref. [90]; SMF, single mode fiber.

Ref.	Year	CE (dB)	BW (nm)	$\lambda_c$ ( $\mu\text{m}$ )	Remarks
[75]	2006	-5.2	40	1.55	
[91]	2007	-1.2	60	1.55	high directionality; simulated
[77]	2009	-4.7	40	1.46	nano hole; DUV fabrication
[92]	2010	-3.7	55	1.55	TM pol.; apodized
[93]	2011	-1.4	38 (1-dB)	1.55	optimized BOX; simulated
[94]	2011	-4.5	60	1.55	pol. independent; simulated
[90]	2011	-2.2	40	1.55	inverse taper; low back reflection
[95]	2012	-4.1	57	1.55	Silicon membrane on glass
[96]	2012	-5	-	2.75	mid-infrared; silicon-on-sapphire
[97]	2013	-1	50	1.55	high efficiency; apodized
[98]	2014	-4.7	100 (1-dB)	1.55	focusing curved; ultra-broadband

[99]	2015	-1.3	52	1.55	high-directionality
[100]	2015	-0.69	60	1.55	sub-dB efficiency
[101]	2016	-11	70 (1-dB)	3.8	mid-infrared; low reflectivity
[102]	2016	-2	410	4.5	mid-infrared; suspended SiGe
[79]	2017	-5	100	5	mid-infrared; Ge-on-Si
[79]	2017	-4	180	5	mid-infrared; Ge-on-SOI
[103]	2017	-0.54	61 (1-dB)	1.55	anti-reflection cladding
[104]	2018	-9.6	310 (1-dB)	7.5	mid-infrared; SiGe (this work)

Table 1. Overview of grating couplers demonstration; coupling efficiency (CE), bandwidth (BW) and central wavelength ( $\lambda_c$ ).

In this context, many outstanding works on grating couplers operating in NIR and MIR have been demonstrated in the last decade as an objective of optimizing its performance in terms of coupling efficiency, bandwidth, polarization dependence and other properties as shown in [Table 1](#). Among them, the recently developed grating couplers operating in MIR operates mainly at short-wave infrared [96,101,102]. Grating couplers working at large wavelength range in the MIR (beyond 6  $\mu\text{m}$  in the fingerprint region) remains missing, especially for the fingerprint region. In this section, we will present the design of grating couplers at long-wave infrared for light coupling from Chalcogenide Photonic Crystal fiber to the Ge-rich SiGe photonic circuit. We chose to design the grating coupler at 7.5  $\mu\text{m}$  wavelength, for possible application in alkane sensing.

### 3.1.1. Phase matching condition

To operate in the diffraction regime where the light is scattered out from the waveguide, the target wavelength  $\lambda$  and the grating period  $\Lambda$  must obey the phase matching condition expressed by the following equation:

$$n_{uc} \sin(\theta_k) = n_B + \frac{k\lambda}{\Lambda} \quad (4)$$

where  $n_{uc}$  is the refractive index of the upper cladding of the grating,  $\theta_k$  is the radiation angle measured from the surface normal,  $n_B$  is the refractive effective index of the Bloch-Floquet mode in the periodic grating region,  $k$  is the diffraction order which is an integer.

Considering that the effective index of the Bloch-Floquet mode is larger than the upper cladding (air cladding  $n_{uc} = 1$ ), it can be deduced that only negative diffraction orders can be radiated out of the grating coupler. As multiple diffraction beams propagating at different angles would interfere each other resulting in a poor coupling efficiency, the single diffraction beam is critical.

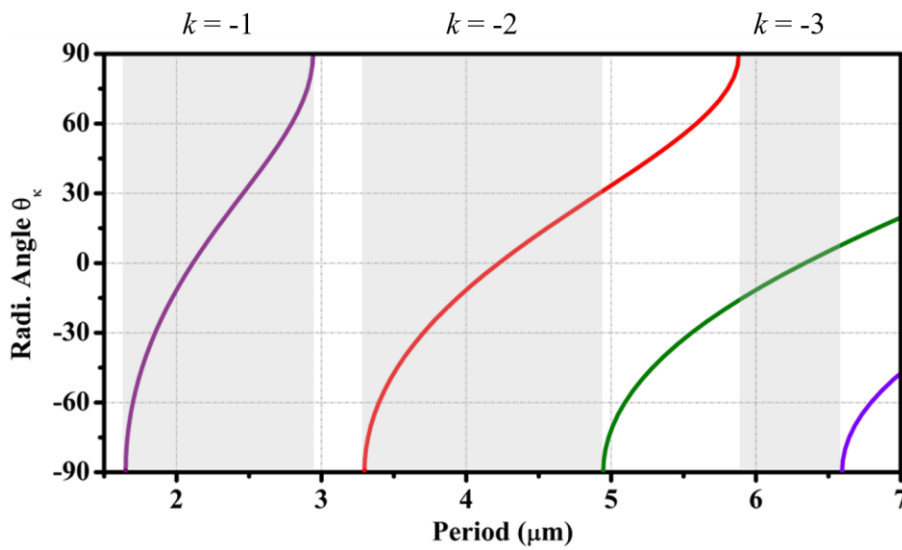


Fig.3.1.3. Radiation phase matching condition in Eq. (4), evaluated as a function of period ( $\Lambda$ ) for TE polarization at a wavelength of  $\lambda = 7.5 \mu\text{m}$  with  $n_B = 3.66$  and  $n_{uc} = 1$ .

To illustrate the behavior of grating couplers in the graded-index  $\text{Si}_{1-x}\text{Ge}_x$  waveguides, the 6- $\mu\text{m}$ -thick graded platform (platform B, waveguide cross-section shown in [Fig.2.1.1](#)) is considered. This choice is related to the higher confinement comparing to platform A while implementing grating couplers in a low index contrast platform is very challenging. Though the coupler design has been done for both TE and TM polarizations, the analysis and simulation process are presented for TE polarization. An effective index of the TE mode, calculated by 2D-Finite Difference Eigenmode (FDE) method, a  $n_B$  of 3.66 at 7.5  $\mu\text{m}$  is considered. [Fig.3.1.3](#) shows the phase matching conditions for radiation as a function of the grating period. The radiation angles ( $\theta_k$ ) is calculated at different grating period for different diffraction orders ( $k = -1, -2, -3\dots$ ). Only first three orders can show the single beam radiation as shown below. Regions colored in gray present the single beam diffraction area where only one order meets the phase matching condition ensuring the single-beam

radiation out of the coupler. Moreover, within the single-beam region, the targeted radiation angle can be obtained.

### 3.1.2. Simulations: evaluation of grating coupler performances

The performance of grating couplers relies first on the fiber-chip coupling efficiency which is defined as the ratio between the power coupled to the fundamental mode of the optical fiber ( $P_F$ ) and the injected power in the fundamental mode of the waveguide ( $P_{AW}$ ). Assuming that the grating is long enough to radiate out all injected power, the coupling efficiency can be expressed by the following equation:

$$CE = \frac{P_F}{P_{AW}} = (1-r) \cdot \Gamma \cdot \eta \quad (5)$$

The factor  $(1-r)$  indicates the power injected into the gratings, where  $r = \frac{P_R}{P_{AW}}$  and  $P_R$  is the reflection back to the access waveguide.  $\Gamma$  is the grating directionality defined by the ratio of the power fraction radiated upward to the sum of power fractions radiated upward and downward expressed as  $\Gamma = P_{up} / (P_{up} + P_{down})$ . The factor  $\eta$  presents the fraction of power radiated upward that is coupled into the fiber, which can be calculated as an overlap factor between the grating radiated field and the optical fiber mode. Ideally, a perfect grating coupler should have no back reflection ( $r \approx 0$ ), high directionality ( $\Gamma \approx 1$ ) and maximum overlap between radiated field and fiber mode ( $\eta \approx 1$ ). The objective of designing a good grating coupler is thus to minimize the back-reflection and maximize simultaneously its directionality and the overlap between radiated field and fiber mode.

### Grating coupler with conventional adiabatic taper

2D Finite-difference time-domain (FDTD) method has been used to calculate the directionality and the back-reflection of the grating coupler with various dimensions at a wavelength of 7.5  $\mu\text{m}$ . Instead of applying 3D simulation method, 2D method provides mainly the advantage of much less time-consuming for the calculation maintaining high-accuracy in the case of low confinement waveguides. As shown in [Fig.3.1.4](#), a light source ( $\lambda = 7.5 \mu\text{m}$ ) is set at the input of the grating considering an access waveguide with an

adiabatic taper, and four electromagnetic field monitors are used to calculate the back-reflection, transmission, power radiated upward and downward, respectively. Moreover, another monitor covering the whole grating coupler is used to calculate the electric field profile. Calculations have firstly been performed for different etching depth by roughly scanning the grating period from 1.5  $\mu\text{m}$  to 6.5  $\mu\text{m}$  with a step of 0.2  $\mu\text{m}$ , and the duty cycle ( $DC = L_{TO}/\Lambda$ , where  $L_{TO}$  is the length of non-etched tooth) from 0.1 to 0.9 with a step of 0.05, to roughly analyze the performance of grating coupler. Calculations have been done for an etching depth of 2 to 4  $\mu\text{m}$ , [Fig.3.1.5](#) shows the representative results of electric field profile simulated for an etching depth of 3 and 4  $\mu\text{m}$ . As can be observed in this figure, the electric field is radiated (mainly down radiation) only at the first few periods of the coupler. The deep etching depth is responsible for the effect. As the used waveguide has a graded-index profile which results in a low vertical light confinement, the radiation down to the substrate occurs when the etching depth is too deep. Then, an etching depth of 2  $\mu\text{m}$  is chosen to reduce the radiation down to substrate.

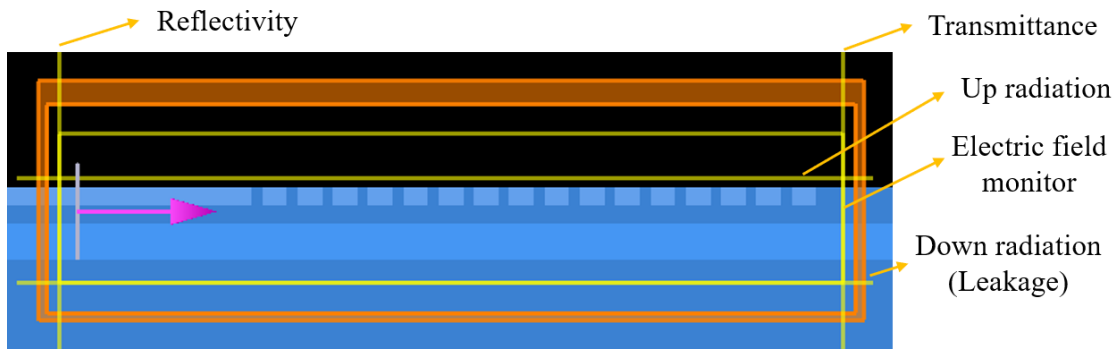


Figure 3.1.4. Captured image of a representative 2D-FDTD simulation window, a light source is set at the input waveguide, a monitor is set in the left of light source to calculate the back-reflection, a second monitor is set at the end of the gratings to calculate the transmittance, then two monitors are set in the upper/lower cladding to calculate the up/down radiation, and a final monitor covering the whole grating coupler is used to calculate the electric field profile.

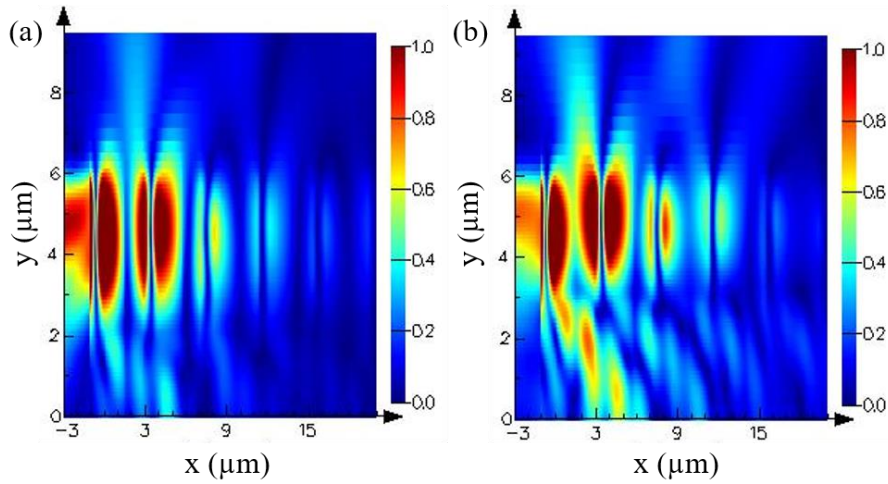


Fig.3.1.5. Simulated electric field profile of grating coupler for a period of 4  $\mu\text{m}$ , duty cycle of 0.5 and an etching depth of (a) 3  $\mu\text{m}$ , and (b) 4  $\mu\text{m}$ .

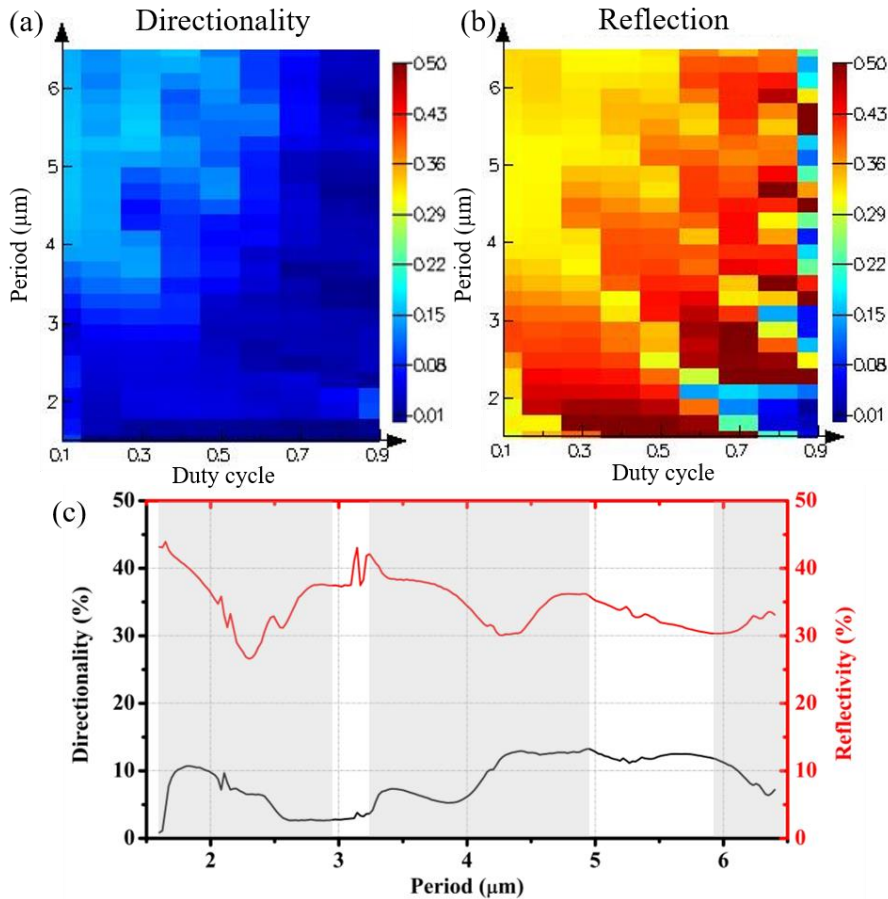


Fig.3.1.6. Simulated color map of (a) directionality and (b) reflectivity for a grating coupler with different period and duty cycle, (c) Example of simulated directionality and reflectivity as a function grating period for a coupler with DC = 0.5 and etching depth of 2  $\mu\text{m}$ .

[Fig.3.1.6](#) reports the calculation of directionality and reflection in the case of a grating coupler using adiabatic taper with 2- $\mu\text{m}$ -etching depth. Poor performances are obtained, as the high back-reflection at the interface of the access waveguide and the gratings limits its performance. The reflectivity could be reduced with large duty cycles ( $> 0.7$ ) but this correspond to very narrow etched patterns, which are challenging to fabricate in terms of practical fabrication.

### Grating coupler with inverse taper

The high value of the back-reflection is a limiting factor for the grating coupler performances. Reflection occurs at the interface between the input waveguide and the grating, because of the index mismatch. It has been shown in [90,101] that inverse taper can be used to reduce the reflection that occurs using conventional adiabatic taper.

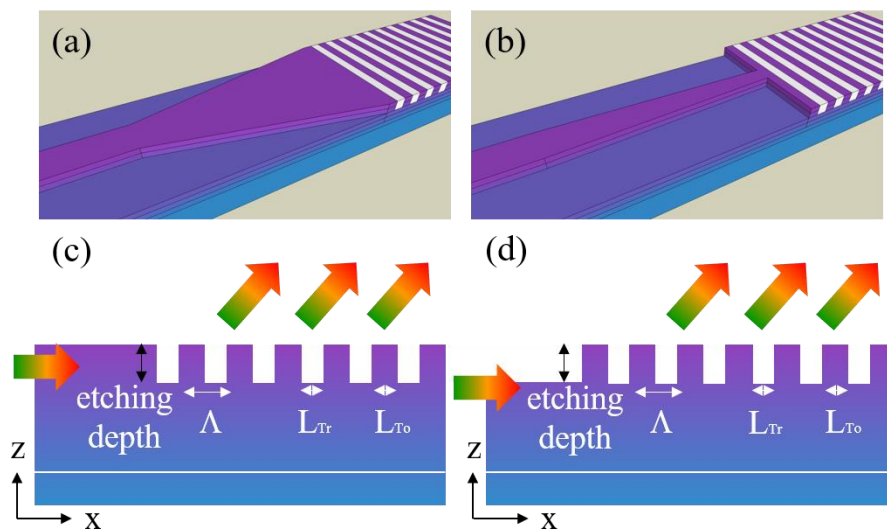


Fig.3.1.7. 3D schematic view of grating coupler with (a) conventional adiabatic taper access, (b) inverse taper access; Equivalent side view of 2D simulation of grating coupler with (c) conventional taper, (d) inverse taper; different colors present the variation of material refractive index.

The 3D schematic view of the two approaches are compared in [Fig.3.1.7](#), the taper width is decreasing along the propagation direction, the optical mode is then deconfined in the y-z plan along the y axis. Thus comparing the equivalent 2D side view, it can be seen that in the 2D simulation approach, the use of an inverse taper is equivalent to a low-index access of coupler as presented in [Fig.3.1.7\(d\)](#). It reduces the index contrast between access

taper and the grating, therefore reduces the back-reflection. Then, starting from the structure with conventional taper access with 2- $\mu\text{m}$ -etching depth, the directionality and the back-reflectivity are then calculated. As shown in Fig.3.1.8, the reflectivity is almost eliminated, and the directionality is thus increased.

Moreover, to calculate the coupling efficiency, the overlap factor of the power radiated upward, and the optical fiber mode has been calculated. The overlap factor is calculated as an integral of the electromagnetic field radiated upward and the gaussian profile of the single mode fiber over the surface of fiber cross-section. In a 2D simulation, in y-z plan, considering the spatial symmetry of fiber mode, the overlap can be calculated as:

$$\eta = \left| \int_z E_{up} \left( G \cdot \exp(i \frac{2\pi n_{uc} z}{\lambda} \sin(\theta)) \right) \right|^2 \quad (6)$$

where  $E_{up}$  is the upward radiation field distribution,  $G$  is the gaussian profile of the fiber mode, and  $\theta$  is the radiation angle of the coupler in radians. The calculated efficiency is shown as the red curve in Fig.3.1.8. As can be observed, the maximum coupling efficiency is -12.5 dB. It is obtained for a grating coupler with a period of 4.5  $\mu\text{m}$  where the length of grating trench ( $L_{Tr}$ ) is equal to 2.75  $\mu\text{m}$  and the length of grating tooth ( $L_{To}$ ) is equal to 1.75  $\mu\text{m}$ . The corresponding duty cycle is of about 0.4.

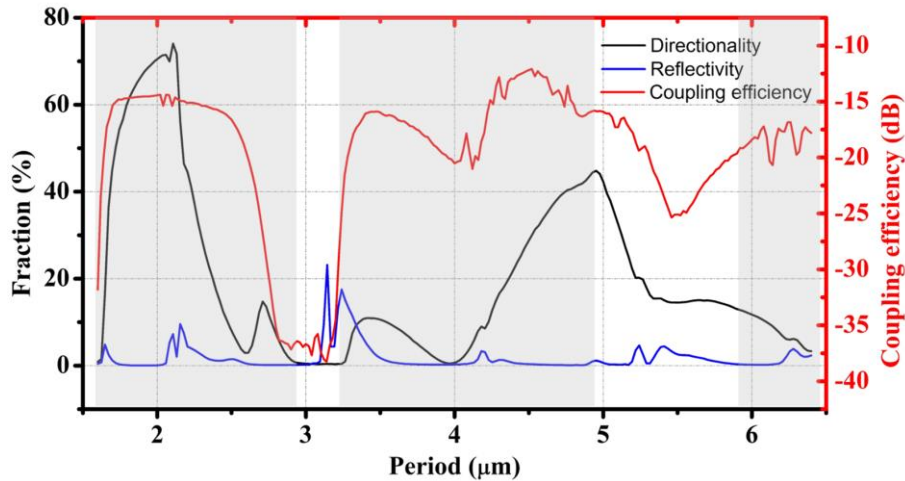


Fig.3.1.8. Simulated directionality, reflectivity and coupling efficiency as a function of period of grating couplers using inverse taper with an etching depth of 2  $\mu\text{m}$  and a duty cycle of 0.4.

After the determination of grating period and duty cycle by optimizing the coupling efficiency in a 2D simulation, the third dimension has to be considered, to obtain the width of the grating and of the inverse taper. The grating width is firstly calculated by means of maximizing the field overlap between the grating coupler and the fiber. Once the grating width is obtained, the tip width of the inverse taper can be calculated by maximizing the mode overlap at the interface of the taper and the grating coupler. The mode profile at the tip of the inverse taper with various tip width is calculated by FDE method using *mode solution*. The objective mode profile of grating coupler at the interface is then calculated by a vector product of its horizontal ( $\vec{E}_y$ ) and vertical ( $\vec{E}_z$ ) components:

$$\vec{E} = \vec{E}_y \wedge \vec{E}_z \quad (7)$$

where  $\vec{E}_y$  can be obtained by extraction of the horizontal component of the simulated electromagnetic field of grating coupler at high-index region,  $\vec{E}_z$  can be obtained by the 2D FDTD simulation which has been performed for the calculation of coupling efficiency.

As the simulation results shown in [Fig.3.1.9](#), the grating coupler with 18  $\mu\text{m}$  width gives an overlap higher than 99% between the coupler and the mode of the optical fiber (black curve). The decrease of field overlap value after the optimization point is due to the continues expansion in lateral direction of the mode when the grating width increasing. Moreover, the largest field overlap between taper tip and gratings can be obtained for a tip width of 1.8  $\mu\text{m}$  as can be observed in [Fig.3.1.9\(a\)](#) (red curve).

Apart from the coupling efficiency, another property, the operating bandwidth is also important for grating couplers. To determine it, the coupling efficiency of the grating coupler for different wavelengths has been calculated. As the result shown in [Fig.3.1.9\(b\)](#) in blue curve, the TE-designed grating coupler has a coupling efficiency of -12 dB at 7.5  $\mu\text{m}$  wavelength with a -1-dB bandwidth of about 300 nm. Furthermore, similar study has also been done for TM polarization. It is worth to note that the TM-designed grating coupler uses a conventional adiabatic taper. It is due to the cut-off of TM mode at this wavelength for narrower waveguide which is limiting the approach of inverse taper. The simulation results show that the TM-designed coupler has an efficiency of -9.6 dB at 7.45  $\mu\text{m}$  with a -1-dB

bandwidth of 310 nm. The final design of grating couplers for both TE and TM polarizations is shown in [Table 2](#).

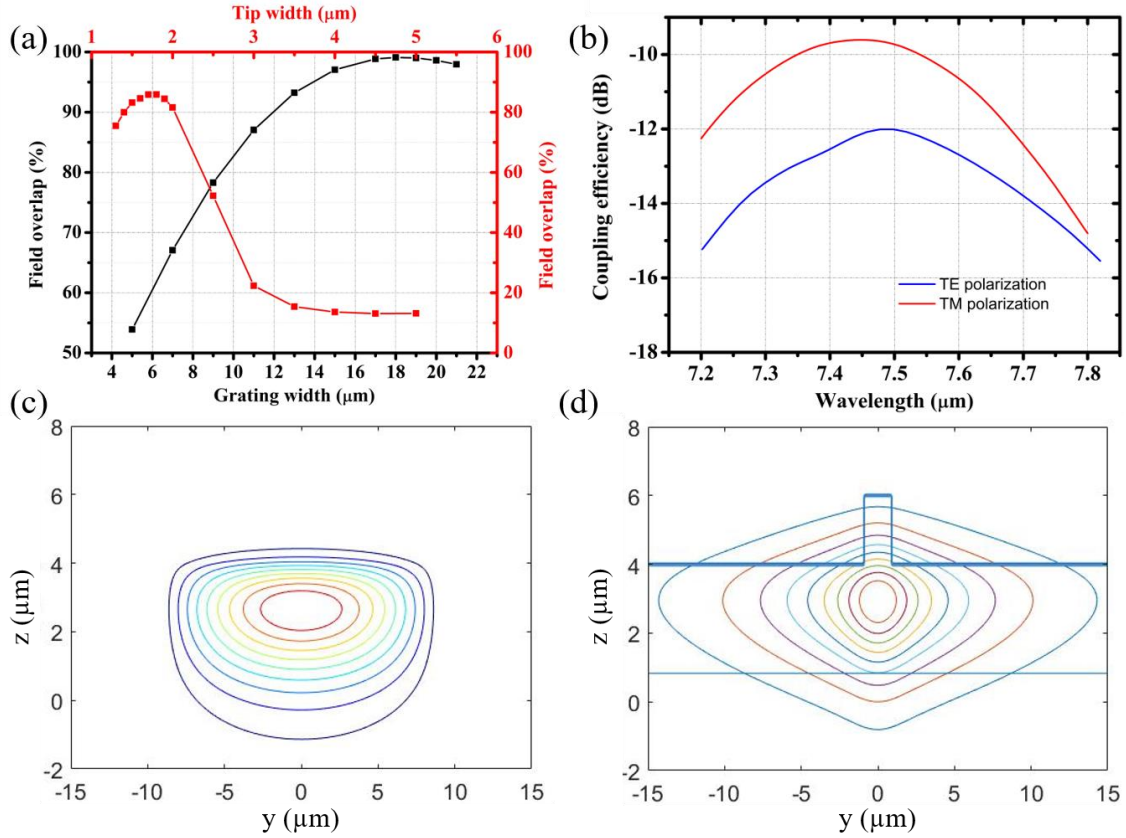


Fig.3.1.9. (a) Field overlap factor between grating coupler and single mode fiber (black curve), and the field overlap between grating coupler and taper tip (red curve); (b) Coupling efficiency as a function of wavelength for TE (blue curve) and TM (red curve) polarization; The contour of (c) the simulated objective mode for grating coupler at the interface; (d) the simulated mode of inverse taper tip.

Polarization	Etch(μm)	$\Lambda$ (μm)	DC	$k$	CE (dB)	BW (nm)	access
TE	2	4.5	0.4	-2	-12	300	I*
TM	1	2.5	0.8	-1	-9.6	310	A**

Table 2. Comparison of grating coupler design for TE and TM polarization. \* Inverse taper access; \*\* Adiabatic taper access.

As the overview of grating couplers demonstration shown in [Table 1](#), grating coupler have been previously demonstrated with a -3-dB bandwidth of 410 nm at 4.5 μm [102] using suspended SiGe. In our work, the -1-dB bandwidth is already more than 300 nm at a

wavelength of 7.5  $\mu\text{m}$ , and the -3-dB bandwidth is more than 600 nm. This broadband operation is due to in one hand the low material dispersion in the MIR wavelength, in another hand the self-mode-adaptation of the graded-index waveguide.

## 3.2. Waveguide Bragg grating

Since the discovery of Bragg's law by Lawrence Bragg [105], Bragg gratings have shown a great impact in the optics society. There are today two main approaches of implementing the Bragg grating, the fiber Bragg grating or on-chip waveguide Bragg grating. The development of waveguide Bragg grating (WBG) could back to 1960s [106], then the first fiber Bragg grating (FBG) was demonstrated in 1978 [107]. Though, the development of WBG is earlier than FBG, however the WBG approach shows today relatively less achievement than FBG in the manufactory point of view. It is mainly due to the technical difficulties on the fabrication method. Although, the development of WBG shows great potential for tones of applications in a point of view of on-chip integration.

In the simplest configuration, as the general principle presented in [Fig.3.1.1](#), similar to the grating couplers, the WBG is also a periodic waveguide with periodic perturbation of the effective index along the propagation direction. For a given wavelength, the periodic waveguide operates as different functionalities while varying the grating period. It operates as a grating coupler when the period is larger than half of the effective wavelength as already presented in the last section. When the grating period decreases, less and less diffraction orders are allowed, once the period meets the Bragg condition where the period is equal to half of the effective wavelength. Thus the periodic waveguide operates as a waveguide Bragg grating where light is back reflected to the waveguide.

Ref.	Year	Rejection (dB)	BW (nm)	Remarks
[108]	2009	~ -7	16	cladding-modulated
[20]	2009	~ -3	~ 60	microfluidic; RI sensing
[109]	2011	-30	1.4	slab-modulated
[110]	2013	-40	2 - 20	slot waveguide
[111]	2015		5.16	temperature sensing

[112]	2016	-25		dual phase-shift; PAM-4 modulation
[113]	2017	~ -60	~ 4	dual-polarization operation
[114]	2017	-40	1.1	subwavelength engineering
[115]	2018	-40	0.8	subwavelength; asymmetry
[116]	2019	-21		mid-infrared; Si <sub>1-x</sub> Ge <sub>x</sub> (this work)

Table 3. Overview of demonstration of waveguide Bragg grating; BW: bandwidth.

The WGB is used in various devices for applications in data communication and sensing systems. A lot of outstanding works have been done in the last years, such as the demonstration of  $\lambda$ -division multiplexer [117], the use of WGB to realize RI sensing [20,21,80]. More recently, a fully reconfigurable waveguide Bragg grating has been implemented on a SOI platform for signal processing [81], then different approaches of cascading Bragg gratings have been demonstrated to achieve narrow-band ultrahigh rejection notch filter for on-chip pump rejection [118,119]. Many other works of waveguide Bragg grating are shown in [Table 3](#). In this section, the design, fabrication and characterization of MIR waveguide Bragg grating are discussed.

### 3.2.1. Waveguide Bragg grating modeling and design

In order to operate in the Bragg regime, where the guided mode is reflected into a backward-propagating mode, the back reflection from each individual period in the gratings should interfere constructively as the schematic view shown in [Fig.3.2.1](#). The constructive interference occurs when the phase matching condition also called the Bragg condition is achieved:

$$k\lambda_B = 2n_{eff}\Lambda \quad (8)$$

where  $k$  is a positive integer which indicates the reflection order,  $\lambda_B$  is the Bragg wavelength and  $n_{eff}$  is the effective index of the Bloch-Floquet mode in the gratings. The reflections interfere constructively only in a narrow band centered at the Bragg wavelength where light is strongly reflected. The waveguide Bragg gratings considered in this work operate in the first order ( $k = 1$ ) in TM polarization. It is obtained by a periodic corrugation of the waveguide surface as shown in [Fig.3.2.1\(a\)](#).

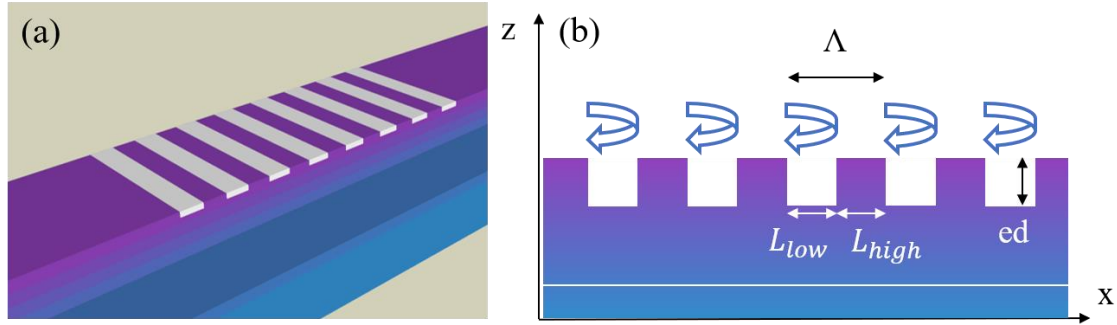


Fig.3.2.1. (a) 3D schematic view of a uniform Bragg grating; (b) Longitudinal 2D schematic view of a uniform Bragg grating,  $x$  is the propagation direction,  $\Lambda$  is the grating period,  $L_{high}$  is the length of high index region,  $L_{low}$  is the length of low index region.

## Coupled mode theory

The most common method to evaluate the performance of Bragg grating is to make use of the coupled mode theory (CMT). It can be used to describe the operation of Bragg grating structure in which the gratings can be considered as a perturbation in the waveguide. Due to its mathematical simplicity and physical intuitiveness, it has been extensively applied as a mathematical tool to analyze the propagation and interaction of electromagnetic field with material [120,121]. Details on the demonstration of CMT for the Bragg grating can be found in [122,123]. Considering a surface-corrugated uniform Bragg grating with rectangular corrugation profile, the reflection (R) and transmission (T) for a such Bragg grating with a length of  $L$  at the target Bragg wavelength can be given respectively by:

$$R = \tanh^2(\kappa L) \quad (9)$$

$$T = \text{sech}^2(\kappa L) \quad (10)$$

with the coupling coefficient  $\kappa$  can be calculated by:

$$\kappa = \frac{\Gamma(n_{high}^2 - n_{low}^2) \sin(\pi \cdot DC)}{\lambda_B n_{eff}} \quad (11)$$

where  $n_{high}$  and  $n_{low}$  denotes high and low refractive index of the two materials inside the gratings,  $DC$  is the duty cycle ( $DC = L_{high} / \Lambda$ ), and  $\Gamma$  indicates the overlap factor between the guided mode and the grating corrugation. It can be calculated as an integral of the

normalized electric field intensity distribution  $\phi_B$  of the guided mode over the surface of grating region.

$$\Gamma = \iint_{\text{grating}} \phi_B(y, z) dy dz \quad (12)$$

As can be calculated by equations (9,11), the maximum reflection of a uniform Bragg grating is obtained for a duty cycle of 0.5. Moreover, the bandwidth of the Bragg grating centered at  $\lambda_B$ , is proportional to the coupling efficient  $\kappa$  :

$$\Delta\lambda = \frac{\lambda_B^2}{\pi n_g} \sqrt{\kappa^2 + \frac{\pi^2}{L^2}} \quad (13)$$

where  $n_g$  is the group index. Therefore, both the reflection and the bandwidth depend on the coupling coefficient  $\kappa$  and on the grating length  $L$ .

## Simulation method and results

The CMT method allows us to put forward a primordial factor, the coupling coefficient (or coupling strength) of the grating which crucially depends on the overlap between guided mode and corrugations. Thus, the design of waveguide Bragg grating requires to maximize this overlap factor at interesting wavelengths. Although the CMT method allows to analyze the performance of the waveguide Bragg grating, however, it requires complex mathematic calculation to properly simulate its spectrum. Therefore, for the spectrum simulation of waveguide Bragg grating, people usually use the FDTD method to determine the dimensions of its corrugations and total length [108,115]. However, the accurate simulation of a waveguide Bragg grating using FDTD method is in general very time-consuming. In order to decrease the simulation time, eigenmode expansion (EME) method has been applied for the design of MIR  $\text{Si}_{1-x}\text{Ge}_x$  waveguide Bragg gratings. The EME method is a rigorous technique to calculate electromagnetic propagation in a waveguide which relies on the modal decomposition of the field into a basis set of local eigenmodes that exists in the cross section of waveguide. It has to be noted that the simulation has been performed for the Bragg grating design is a 2D EME simulation in the x-z plan as schematic shown in [Fig.3.2.1\(b\)](#).

The simulations have firstly been performed on the waveguides based on platform A with 11- $\mu\text{m}$ -thick graded layer and 2- $\mu\text{m}$   $\text{Si}_{0.2}\text{Ge}_{0.8}$  constant layer (cross-section see [Fig.2.1.1](#), schematic simulated structure see [Fig.3.2.1](#)). Simulation has been done with  $\text{DC} = 0.5$ ,  $\lambda_B = 7.5 \mu\text{m}$  and for a grating pitch  $p = 1 \mu\text{m}$  calculated by Eq. (8) considering the fundamental TM mode in a 5- $\mu\text{m}$ -wide waveguide.

The simulation results show that the coupling coefficient with weak top corrugation (etching depth  $ed = 0.3 \mu\text{m}$ ) is very low which leads to an extremely low Bragg reflection, as can be observed in [Fig.3.2.2\(a\)](#). The Bragg reflection is less than 30% for a uniform grating with 1 cm total length. Moreover, it shows a saturation when the total length increases, because of the high grating loss.

As shown in [Fig.3.2.2\(b\)](#), the grating loss increases when the etching depth of corrugation is increasing. The high grating loss is due to the low vertical index contrast of the platform A as shown in [Fig.2.1.1](#). When the perturbation increases, more and more power is scattered into the substrate. Consequently, to design a waveguide Bragg grating based on platform A, the etching depth of the corrugations must be low enough to avoid the power leakage. However, the total length of such a Bragg grating with weak corrugations will be extremely long ( $> 1 \text{ cm}$ ) in order to obtain high reflection.

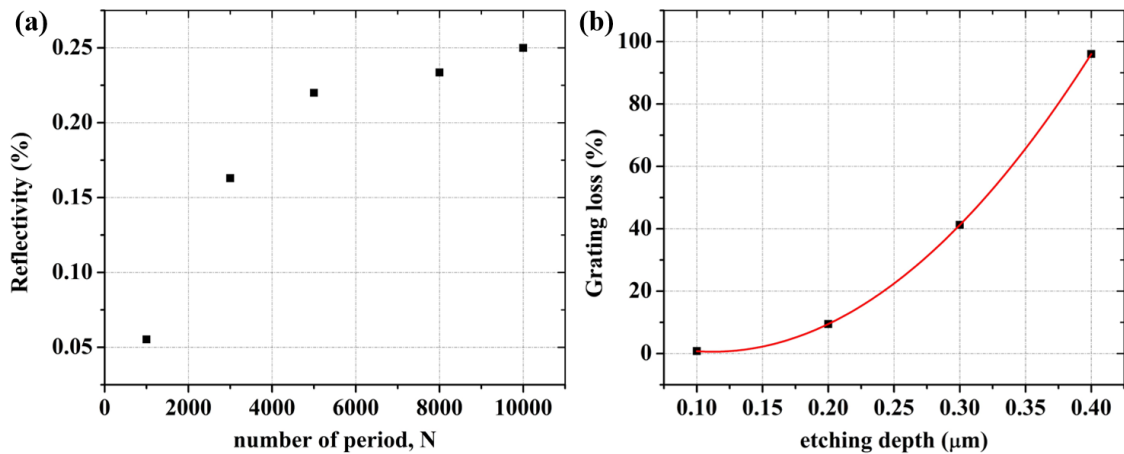


Fig.3.2.2. (a) Simulated spectrum of Bragg grating with  $ed = 0.3 \mu\text{m}$ ; (b) Simulated grating loss as a function of corrugation etching depth  $ed$  with  $N = 1000$ ; simulation has been performed with  $\text{DC} = 0.5$ , and  $p = 1 \mu\text{m}$ .

Therefore, waveguide Bragg gratings have been designed using the platform B, which provides higher index contrast together with low propagation loss as already presented in the previous chapter. To evaluate the grating loss as a function of the corrugation etching depth, simulations have been performed for different values of the etching depth (ed) while fixing all other parameters (DC = 0.5, N = 100,  $p = 1.02 \mu\text{m}$  calculated by considering fundamental TM mode for a 5- $\mu\text{m}$ -width waveguide at  $\lambda_B = 7.5 \mu\text{m}$ ). [Fig.3.2.3](#) presents the grating loss as a function of the corrugation etching depth. As can be observed, the grating loss is negligible (< 1%) for a corrugation etching depth below 400 nm.

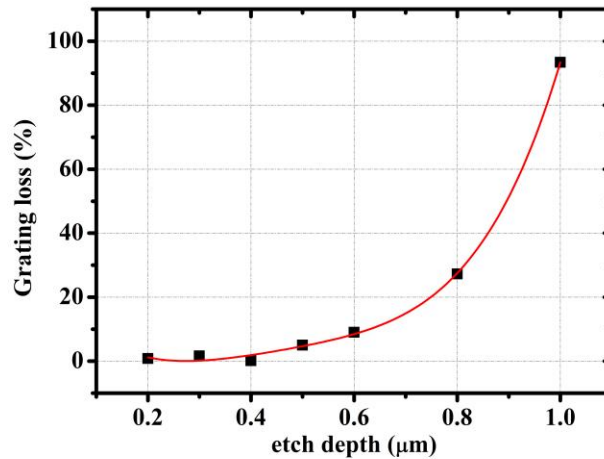


Fig.3.2.3. Grating loss as a function of etch depth of corrugations. Simulation has been performed with DC = 0.5, N = 100, and  $p = 1.02 \mu\text{m}$ .

The total reflection and grating loss have then been simulated for gratings with different number of period N from 50 to 300, for an etching depth of 400 nm. As shown in [Fig.3.2.4\(a\)](#), a waveguide Bragg grating with N = 250 can achieve a total reflection higher than 90% keeping low grating loss (<5%) as shown in Fig 3.2.4 (b). The blue-shift of the Bragg wavelength is due to the over estimation of the effective index of the Bloch-Floquet mode. Indeed in the calculation of the period of the Bragg grating by Eq. (8), as an approximation we used the effective index of TM mode of the straight waveguide ( $n_{WG} > n_{Bloch}$ ). However it is then straightforward to tune the Bragg wavelength by slightly tuning the Bragg period, to achieve for example a target wavelength of 7.5  $\mu\text{m}$ .

Thus, finally, a waveguide Bragg grating based on the graded-index  $\text{Si}_{1-x}\text{Ge}_x$  waveguide has been designed. The width is  $W_{WG} = 5 \mu\text{m}$ , the waveguide etching depth is  $\text{ED} = 4 \mu\text{m}$ , the duty cycle is  $\text{DC} = 0.5$ , the period is  $p = 1.02$  for operation at  $\lambda_B = 7.3 \mu\text{m}$ , and the corrugation etching depth is  $\text{ed} = 400 \text{ nm}$ . With period number  $N \geq 250$  it is possible to obtain a Bragg reflection higher than 90%. Furthermore, the broadband characteristics of the  $\text{Si}_{1-x}\text{Ge}_x$  waveguides allow us to efficiently tailor the central operating wavelength of Bragg grating by simply modifying the grating period according to the Bragg condition as shown on [Fig 3.2.4\(c\)](#).

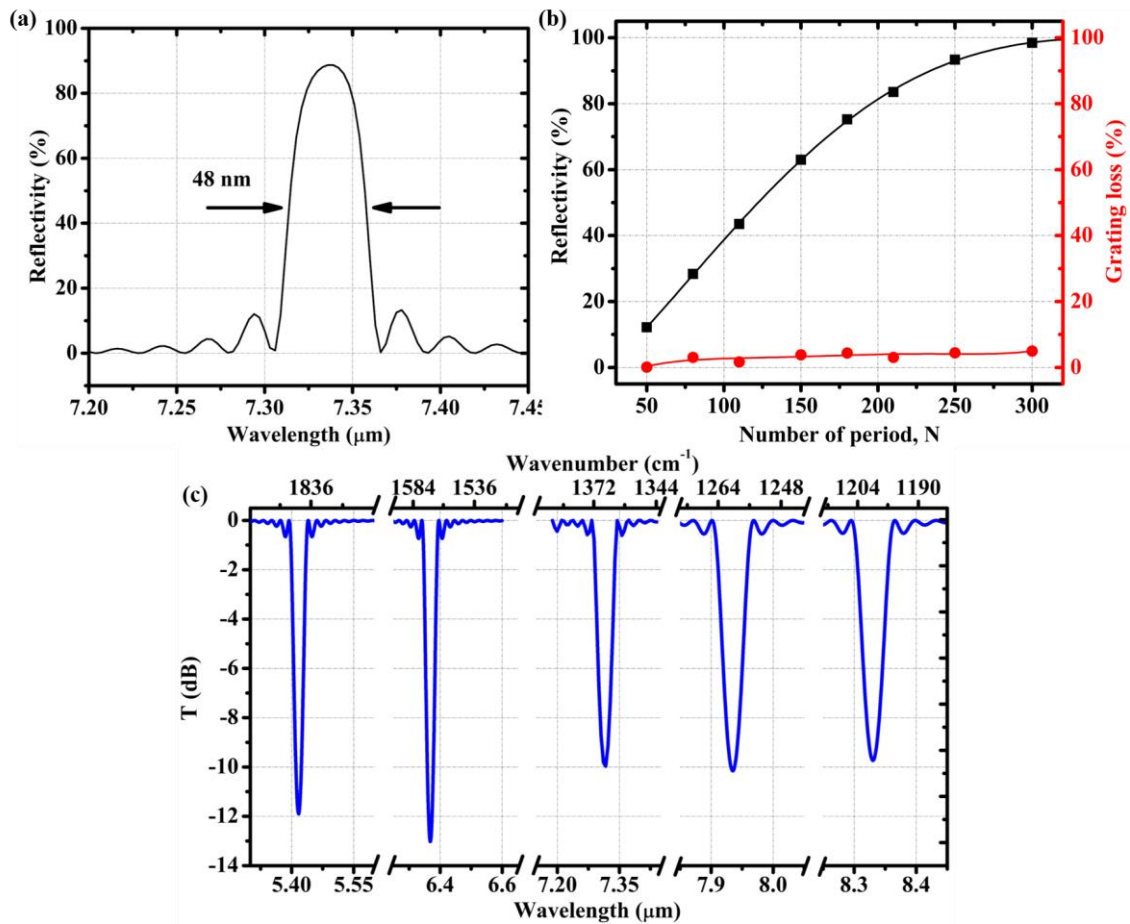


Fig.3.2.4. (a) Simulated reflectivity of a Bragg grating with  $N = 250$ , and  $p = 1.02 \mu\text{m}$ ; (b) Simulated reflection and grating loss at Bragg wavelength as a function of number of period; (c) Simulated spectrum of waveguide Bragg gratings with various period. Simulations have been performed with  $\text{DC} = 0.5$ ,  $\text{ed} = 0.4 \mu\text{m}$ , and  $N = 250$ .

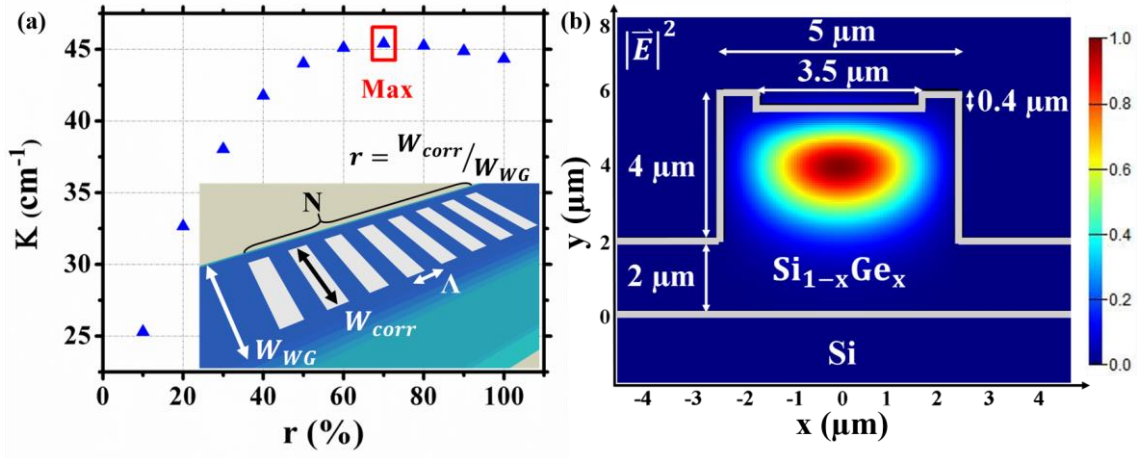


Fig.3.2.5. (a) Calculated coupling coefficient of the waveguide Bragg grating as a function of the ratio  $r$  between the corrugation width ( $W_{corr}$ ) and the nominal waveguide width ( $W_{WG}$ ); Inset: 3D schematic view of a waveguide Bragg grating. (b) Schematic of the waveguide cross-section with the simulated fundamental TM mode profile at the low index region of grating.

Then, in order to experimentally confirm the operation of the designed MIR waveguide Bragg grating, devices with different number of period ( $N = 210, 250, 280$ ) and values of the period ( $p = 0.74, 0.88, 1.02, 1.10, 1.16 \mu\text{m}$ ) have been selected for device fabrication. Moreover, taking into account the technical limitation which will be discussed in the next section in detail, the corrugations within the Bragg waveguide will be narrower than the waveguide width. Thus, it is possible to overcome technical issues related to the alignment of the corrugation and the waveguide definition. Furthermore, with this design, illustrated in the inset of [Fig.3.2.5\(a\)](#), an increase of the Bragg coupling coefficient is even obtained, which is attributed to an increase of the overlap factor between the Bloch-Floquet mode and the corrugation, that leads to a higher Bragg reflection as described by Eq. (11). [Fig.3.2.5](#) presents the calculated coupling coefficient as a function of the corrugation width and the cross-section of the designed Bragg grating at low-index region with the simulated TM mode profile at  $7.3 \mu\text{m}$ . The coupling coefficient is calculated by Eq. (11) with an overlap factor estimated using *mode solution* by calculate the overlap of guided mode with the corrugation region as shown in [Fig.3.2.5\(b\)](#). Although this method is not a rigorous 3D simulation of the Bragg grating, it gives the tendency on how the corrugation width affects the performance of waveguide Bragg gratings. The corrugation width is then chosen to be

$W_{corr} = 0.7W_{WG}$ , as it provides the highest coupling coefficient which would result in the highest value of the Bragg reflection.

### 3.2.2. Fabrication

The waveguide Bragg grating requires two etching steps: a shallow etch (400 nm) for the corrugation, and a deep etch (4  $\mu\text{m}$ ) for the waveguide definition. In a first attempt, we targeted to have the corrugation in the full width of the waveguide, targeting the structure of [Fig.3.2.1](#). Considering the alignment between the two steps during fabrication, the width of corrugations is designed much wider than the nominal waveguide width to avoid the misalignment as shown in [Fig.3.2.6](#) (blue bar represents the waveguide, black bars represent the grating corrugations).

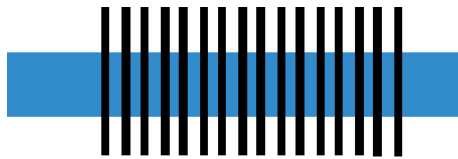


Fig.3.2.6. Schematic top view of the optical mask of waveguide Bragg grating.

Considering the dimension of the grating corrugations, the use of the optical lithography is challenging to properly define the small corrugations. Therefore, the fabrication process is a combination of an electron-beam (ebeam) lithography to define grating corrugations and optical lithography to define the waveguides. [Fig.3.2.7](#) shows the fabrication flow of the waveguide Bragg grating presented as a cross-section in the low-index region. Fabrication process for the first level, grating corrugations, are shown in [Fig.3.2.7\(a-d\)](#), and the process for the second level, waveguide definition, are shown in [Fig.3.2.7\(e-i\)](#). Same as the process described in chapter 2, the wafer is firstly cleaned using acetone and isopropanol in ultrasound cleaning machine. Then a layer of high resolution ebeam resist, ZEP520A, is spin-coated on the sample surface with a speed of 3000 rpm followed by 3 mins annealing at 180  $^{\circ}\text{C}$ . In this condition, a layer of about 260 nm-thick ZEP is deposited upon the sample surface. The grating corrugations are defined by ebeam lithography. After the illumination, the photoresist is developed using ZED-N50 and a solution of methyl isobutyl ketone and isopropanol (MIBK/IPA = 1:3). Once the development has been done, the gratings are

etched using ICP etching, followed by a chemical wet etch with  $\text{H}_2\text{O}_2$  to smooth sidewall roughness. Finally, the photoresist is removed by butanol. Once the first level of grating corrugations is well fabricated, the second level, waveguides are fabricated using the same technique as described in chapter 2 (see [section 2.2](#)). It is worth to note that the alignment marks are used during the process of optical lithography to align corrugations and waveguide. The used recipes for lithography and ICP etching have been developed by Xavier Le Roux.

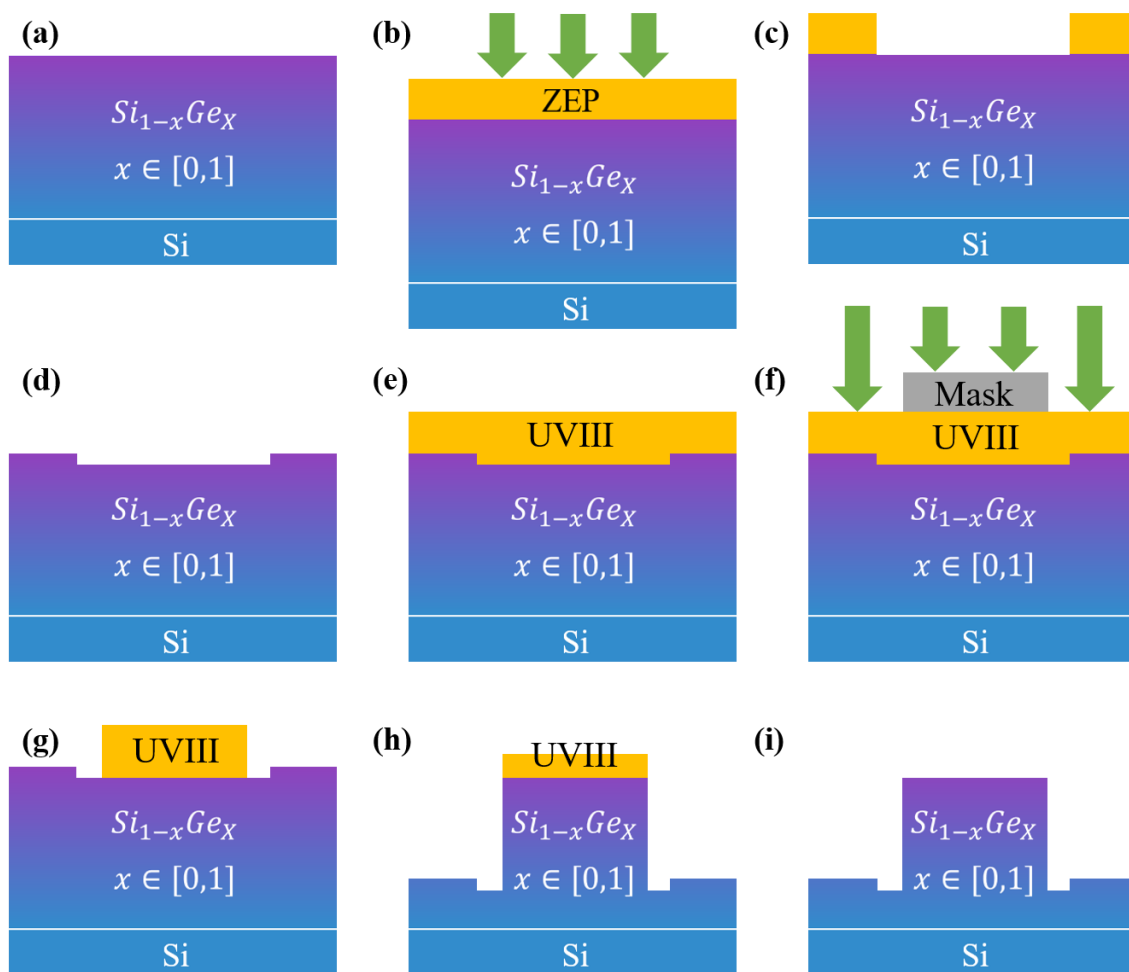


Fig.3.2.7. (a-d) 1<sup>st</sup> level, (e-i) 2<sup>nd</sup> level. (a) sample surface cleaning; (b) deposition of photoresist and the ebeam lithography; (c) development; (d) ICP etch for corrugation and clean of residual of photoresist; (e) deposition of photoresist for optical lithography; (f) optical lithography; (g) development; (h) ICP etch of waveguide; (i) clean of residual of photoresist.

The SEM images of fabricated  $\text{Si}_{1-x}\text{Ge}_x$  MIR waveguide Bragg grating sample are shown in [Fig.3.2.8](#). The micropillars on both sides of the grating area which can be observed in [Fig.3.2.8\(a,b\)](#), is the fact that the etched corrugations modify the initial conditions for the second level, i.e. for the waveguide definition. It results in a non-homogenous deposition of the photoresist, which would result in a non-homogeneous illumination during the lithography. Moreover the used photoresist for optical lithography, UVIII is very sensitive to illumination dose. The non-homogeneous layer of photoresist causes then overdose at the waveguide edge in the straight waveguide area and grating area. After the development, it brings a trapezoid-like layer of photoresist as shown in [Fig.3.2.8\(d\)](#) which at the end causes an over-etch effect of the waveguide. Closer to the grating area, the more tremendous over-etch effect is observed (it means a bigger value of  $\alpha$  in [Fig.3.2.8\(d\)](#)). Consequently, waveguides with narrower width and tangible sidewall roughness are obtained as shown in [Fig.3.2.8\(c\)](#). Therefore, high propagation loss can be predicted.

In order to resolve this fabrication issue for the second level, we have to obtain homogeneous layers of photoresist. To do so, the design of the corrugation has been modified, to use narrower corrugations inside the waveguide as shown in [Fig.3.2.9\(right\)](#). In this case, micropillars on both sides of the grating area would disappear, and at the meantime, pre-etched corrugations would not affect anymore the waveguide sidewall roughness. However, this approach requires a more precise alignment between the two levels to make the grating corrugations at the center of waveguide. Therefore manual alignment is very challenging. E-beam lithography is then used for both the corrugation and waveguide definitions, with automatic alignment between them. An alignment precision of less than 100 nm is then achieved with the developed new process.

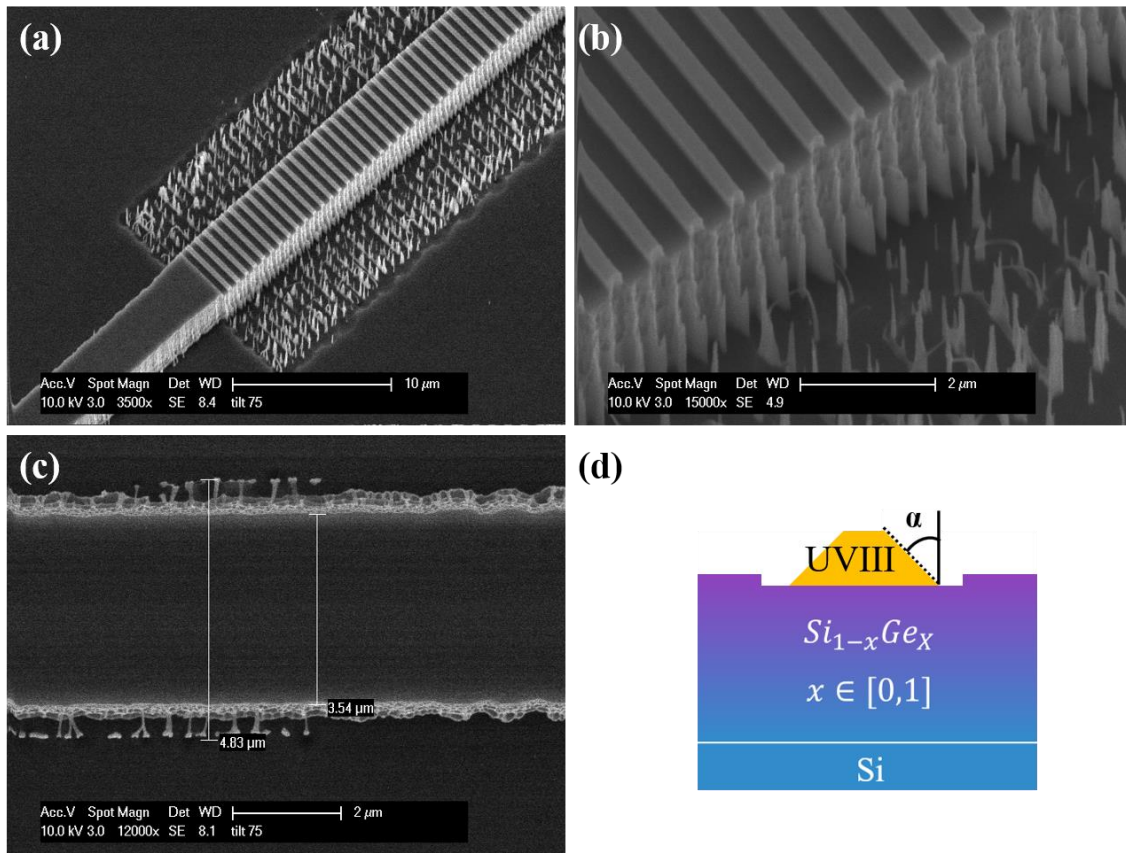


Fig.3.2.8. SEM images of waveguide Bragg grating (a) & (b) at grating area; (c) at straight waveguide area; (d) Schematic view of the cross-section of low-index region for second level.



Fig.3.2.9. Schematic top view of the optical mask of waveguide Bragg grating, (left) first design, (right) optimized design.

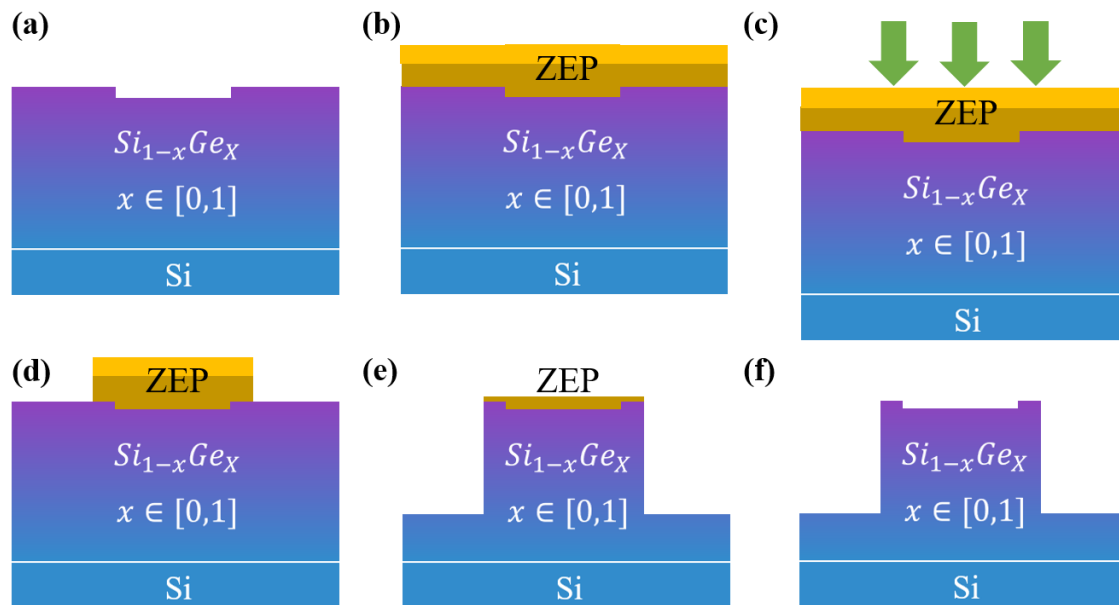


Fig.3.2.10. Fabrication flow for the second level presenting the schematic waveguide cross-section. (a) sample clean after corrugation etch; (b) deposition of double layers of ZEP; (c) ebeam lithography; (d) development; (e) ICP etch; (f) clean the residual of resist.

We started then the same process as described in [Fig.3.2.7\(a-d\)](#) for the first level. Then the new fabrication flow for the second level is shown in [Fig.3.2.10](#): two layers of ZEP520A are spin coated on the surface of the sample, with a spin speed of 1500 rpm. 1 min annealing at 180 °C is applied after the deposition of first layer, then 3 mins annealing at 180 °C is done after the deposition of second layer. A total thickness of about 1.2  $\mu\text{m}$  is obtained in order to etch 4  $\mu\text{m}$  deep for the waveguide. Then the waveguide patterns are defined using the ebeam lithography with the optimized auto-alignment process. After the illumination, the photoresist is developed using ZED-N50 and a solution of methyl isobutyl ketone and isopropanol (MIBK/IPA = 1:3). Once the development has been done, the waveguide is etched using the ICP process described above.

SEM images of waveguide Bragg grating fabricated using the new design are shown in [Fig.3.2.11](#). As it can be observed, the grating corrugations and waveguide are properly aligned, and the waveguide sidewall is well defined. The typical dimension of the sidewall roughness is in the order of magnitude of around 100 nm which is totally negligible in the MIR wavelength range.

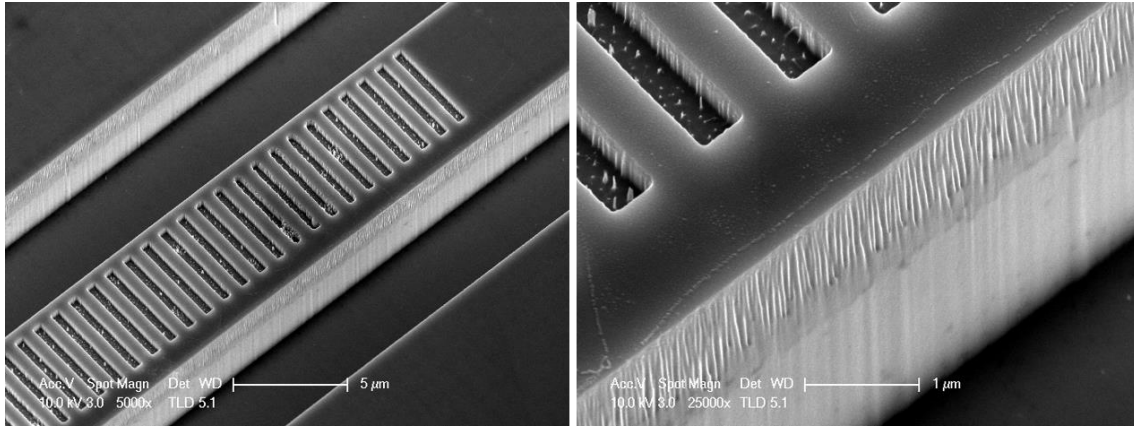


Fig.3.2.11. SEM images of waveguide Bragg grating fabricated using the optimized design and fabrication process.

### 3.2.3. Characterization and results

The waveguide Bragg grating sample is characterized using the free-space MIR set-up as described in [section 2.3.1](#). Measured transmission spectrums of  $\text{Si}_{1-x}\text{Ge}_x$  waveguide Bragg gratings normalized by the straight waveguide transmission are shown in [Fig.3.2.12](#). As it can be observed, the experimental results are in good agreement with EME simulation. The measured central wavelengths (with the simulated values in the parentheses) of each waveguide Bragg grating are  $5.43 \mu\text{m}$  ( $5.417 \mu\text{m}$ ),  $6.405 \mu\text{m}$  ( $6.368 \mu\text{m}$ ),  $7.32 \mu\text{m}$  ( $7.317 \mu\text{m}$ ),  $7.952 \mu\text{m}$  ( $7.935 \mu\text{m}$ ), and  $8.345 \mu\text{m}$  ( $8.33 \mu\text{m}$ ), respectively. The slight difference in central wavelength is due to the different corrugation width between simulation ( $W_{corr} = W_{WG}$ ) and experiment ( $W_{corr} = 0.7 \times W_{WG}$ ). It results in an increase of the index of Bloch-Floquet mode in the fabricated sample compared to simulation, which leads to a red-shift of the rejection band of the waveguide Bragg grating. The low power rejection at large wavelengths may be contributed to higher losses. Moreover, the measured FWHM (-3-dB bandwidth) of each Bragg grating (with the simulated values in the parentheses) are equal to  $59 \text{ nm}$  ( $30 \text{ nm}$ ),  $79 \text{ nm}$  ( $40 \text{ nm}$ ),  $71 \text{ nm}$  ( $44 \text{ nm}$ ),  $20 \text{ nm}$  ( $41 \text{ nm}$ ), and  $20 \text{ nm}$  ( $44 \text{ nm}$ ), respectively.

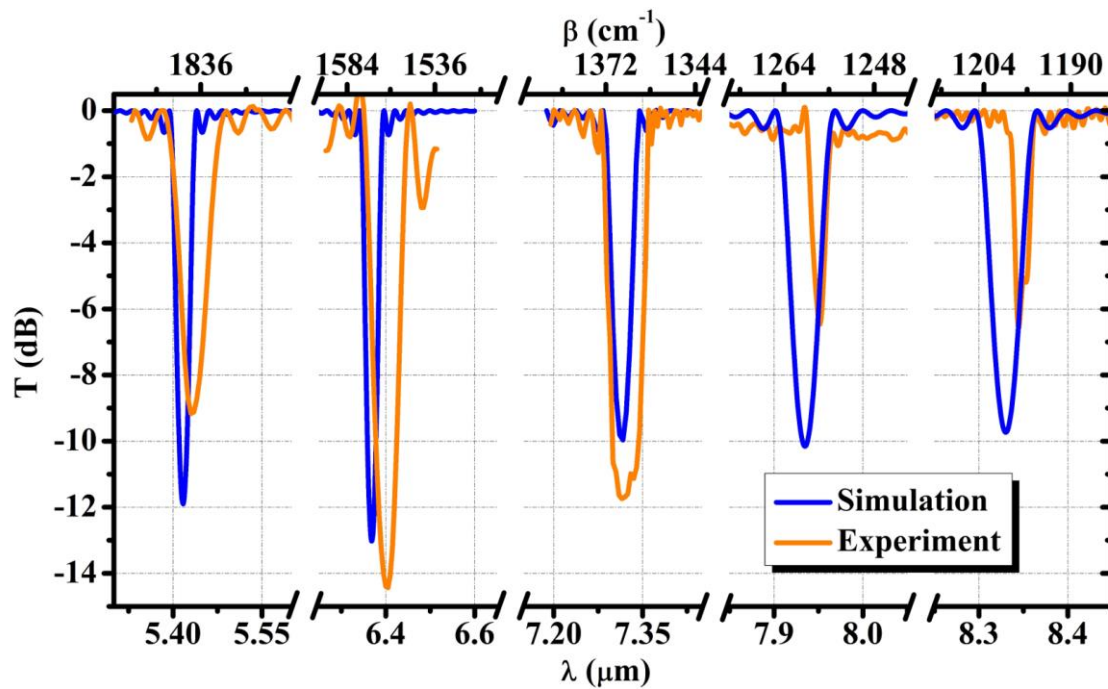


Fig.3.2.12. Simulated (blue curves) and measured (orange curves) transmittance spectrum of the  $\text{Si}_{1-x}\text{Ge}_x$  waveguide Bragg grating with number of period  $N = 250$ , and a period of 0.74, 0.88, 1.02, 1.10, 1.16  $\mu\text{m}$ , resulting in an operation at 5.4, 6.4, 7.3, 7.95 and 8.35  $\mu\text{m}$ , respectively.

[Fig.3.2.13\(a\)](#) presents the measured transmittance for various total grating lengths, i.e. different number of grating periods  $N$ , while maintaining a constant grating period of 0.88  $\mu\text{m}$ , providing rejection centered at  $\lambda = 6.4 \mu\text{m}$ . It can be observed that the minimum transmittance decreases as the number of period increases, which corresponds to an increase of the Bragg grating rejection. A maximum power rejection of 21.6 dB is measured for a waveguide Bragg grating with  $N = 280$ . The simulated minimum transmittance at Bragg wavelength as a function of the number of period  $N$  comparing with experiments is shown in [Fig.3.2.13\(b\)](#), a good agreement is obtained. The increasing error between simulation and experiment may be contributed to an accumulation of the error on the rejection power for each grating period.

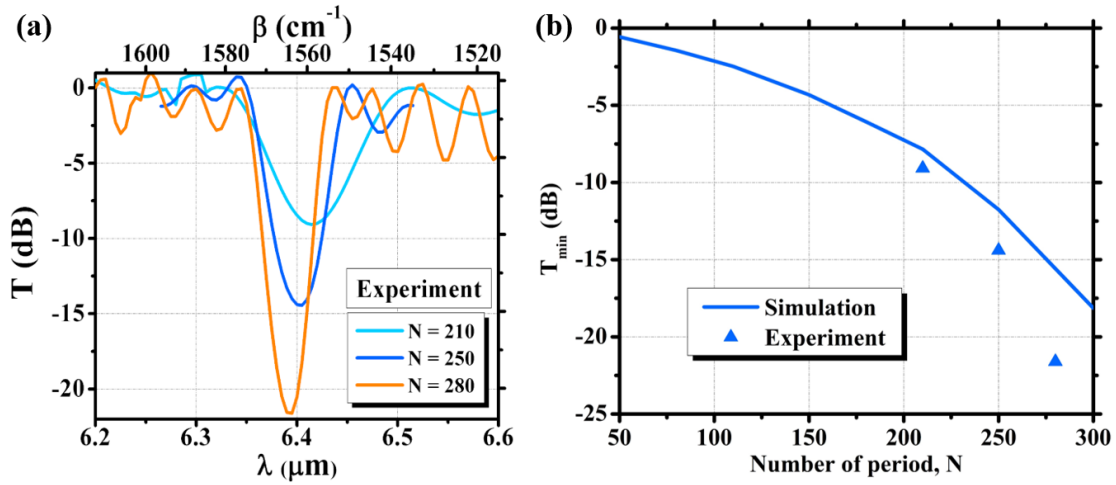


Fig.3.2.13. (a) Measured transmittance of waveguide Bragg grating for various number of period  $N = 210, 250, 280$ ; (b) Minimum transmittance at the Bragg wavelength as a function of number of period  $N$ .

### 3.3. Conclusion

In this chapter, two kinds of periodic structures working at long-wave infrared wavelengths have been discussed. In the first part, periodic waveguide operating in radiation regime as a grating coupler has been studied. 2D simulation method combining the FDTD simulations and analytical calculation by Matlab script are introduced for the design of broadband mid-infrared grating coupler based on the graded-index  $\text{Si}_{1-x}\text{Ge}_x$  waveguide. A coupling efficiency of about -12 dB (-9.6 dB) has been obtained for TE (TM) polarization, with a -1-dB bandwidth of more than 300 nm in both polarizations. Moreover, the performance of such grating coupler can be further improved by apodizing the geometry of the gratings. Departing from the simulation results, the next step would be to experimentally confirm the performance of the grating couplers in the MIR wavelength range. This would require a re-adaptation of our MIR experimental set-up from free-space configuration to fiber system.

In the second part, waveguide Bragg gratings have been studied. The simulation methods using coupled mode theory (CMT) and eigenmode expansion (EME) have been discussed. Then, fabrication process and designs have been optimized simultaneously to properly fabricate waveguide the waveguide Bragg gratings. Finally, simulation results have

been confirmed by experimental measurements. MIR Bragg gratings are indeed experimentally demonstrated at different wavelengths in a very large wavelength range from about 5.4 to 8.4  $\mu\text{m}$ , benefiting from the advantage of broadband  $\text{Si}_{1-x}\text{Ge}_x$  waveguide. This result paves the way for the demonstration of integrated MIR resonant structures, like Fabry-Perot cavity using the Bragg gratings as mirrors. It can be a key component, in terms of enhancement of sensing capability, for the demonstration of high-performance integrated MIR optical sensor. The integrated MIR resonators are then presented in the next chapter.

## 4. Mid-IR integrated resonators

Following the demonstration of low-loss broadband graded-index  $\text{Si}_{1-x}\text{Ge}_x$  waveguides and their sensing capability in the mid-infrared wavelength range, the possibility to integrate resonators has been investigated. Resonators are building blocks that can be used in different applications including: i) wavelength filtering, ii) to increase the performance of sensing structures or iii) to enhance non-linear Kerr effect for frequency comb generation. Since the waveguide Bragg grating has been successfully implemented in a wide wavelength range, the distributed Bragg reflector cavities are then demonstrated by integrating two identical Bragg gratings as reflecting mirrors, with a straight waveguide in between as a cavity. Another approach, racetrack resonators are also implemented based on this graded-index  $\text{Si}_{1-x}\text{Ge}_x$  waveguides in the long-wave infrared wavelength range. In this chapter, the demonstration of these two resonant structures in a point of view of design, fabrication and experimental results are discussed. The design and demonstrations are done at 8  $\mu\text{m}$  wavelength. This wavelength has been chosen as it is localized in the molecular fingerprint region which is interesting for bio-chemical sensing and is not easily accessible with Si-based photonics, while it has been demonstrated that the SiGe platform can provide low propagation losses at this wavelength.

### 4.1. Fabry-Perot Cavities

From the demonstration of waveguide Bragg grating presented in the previous chapter, it is possible to implement the distributed Bragg reflector cavity, which can be considered analogous to a Fabry-Perot cavity, by integrating two identical Bragg gratings as reflecting mirrors. [Fig. 4.1.1](#) shows a 3D schematic view of the Fabry-Perot cavity using the  $\text{Si}_{1-x}\text{Ge}_x$  waveguide Bragg grating. As a main difference with conventional Fabry-Perot cavity using dielectric coatings which strongly reflect the light within a few periods of the alternating layers, Bragg gratings reflect the light over a much larger number of grating period. Consequently, light is reflected in a distributed manner along the propagation direction in the Bragg gratings. The key advantage of distributed Bragg grating cavity is that, in the

opposite of ring or racetrack resonators where the maximal Free Spectral Range (FSR) is dictated by the minimal ring radius, there is no restriction on the minimal cavity length of a distributed Bragg grating cavity, excepted the one related to the penetration depth in the Bragg mirror. Thus large FSR ( $> 30$  nm at  $8 \mu\text{m}$  in the case of  $\text{Si}_{1-x}\text{Ge}_x$  waveguides) is achievable. Furthermore, thanks to the narrow reflection bandwidth of the distributed Bragg mirror, single longitudinal mode cavity is achievable.

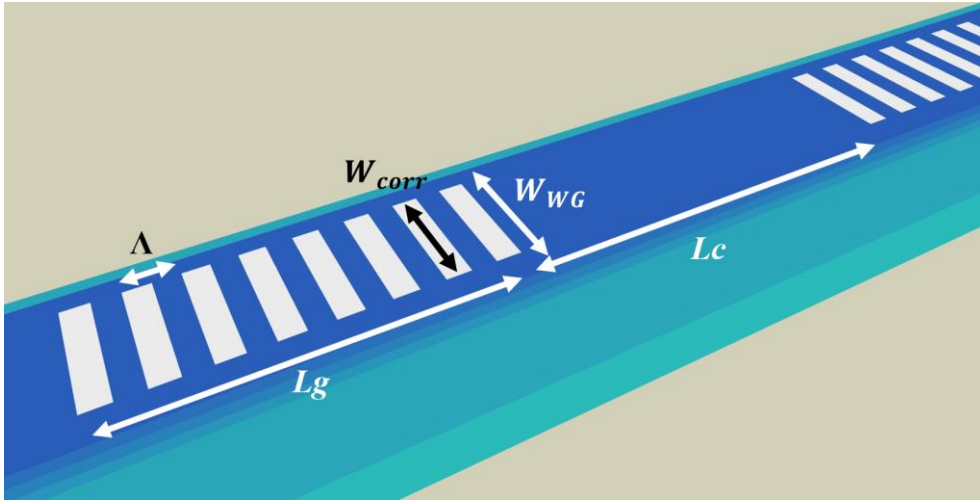


Fig.4.1.1. 3D schematic view of Fabry-Perot cavity using  $\text{Si}_{1-x}\text{Ge}_x$  waveguide Bragg grating with top corrugations.

#### 4.1.1. Analytical model and Simulations

The distributed Bragg reflector cavity obeys in general the same principle as conventional Fabry-Perot cavity. Considering two identical mirrors for in/output as shown in [Fig.4.1.2](#), assuming no loss in the mirror, the light transmission spectrum can be calculated using the following function [124]:

$$T = \frac{T_{\max}}{1 + \frac{4h}{(1-h)^2} \sin^2\left(\frac{2\pi}{\lambda} n_{\text{eff}} L_c\right)} \quad (14)$$

with

$$T_{\max} = \frac{(1-R_g)^2 \exp(-\alpha L_c)}{(1-R_g \exp(-\alpha L_c))^2} \quad (15)$$

$$h = R_g \exp(-\alpha L_c) \quad (16)$$

where  $R_g$  is the mirror reflection in intensity,  $\alpha$  is the loss per unit length in the cavity ( $\text{m}^{-1}$ ),  $L_c$  is the cavity length.

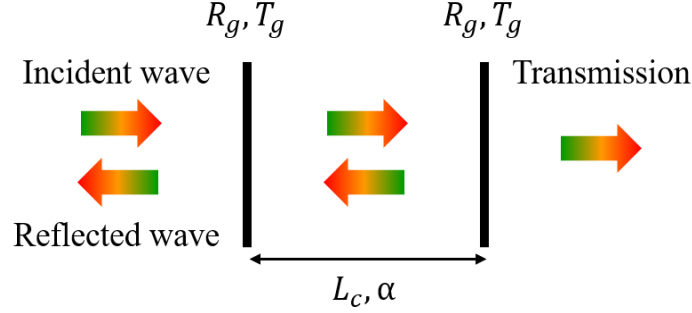


Fig.4.1.2. Schematic view of a simplest configuration Fabry-Perot cavity.

The Eq. (14) indicates the periodicity of the transmission of cavity as a function of wavelength for the resonance where the maximum transmission  $T_{max}$  is obtained. The wavelength spacing, called the free spectral range between the respective cavity resonances can be given by:

$$FSR = \Delta\lambda_{FSR} = \frac{\lambda^2}{2n_g L_c} \quad (17)$$

Moreover, considering a central wavelength of a cavity resonance  $\lambda_0$ , the spectral width, full width at half maximum (FWHM) of the resonance peak is given by:

$$\delta\lambda = \frac{\lambda_0^2}{\pi n L} \arcsin \left( \sqrt{\frac{(1 - R_g e^{-\alpha L_c})^2}{4R_g e^{-\alpha L_c}}} \right) \quad (18)$$

Then, the quality factor (Q-factor) which describes the resonance behavior of the cavity can be calculated by Eq. (19). It indicates that a high Q resonance would have sharp resonance peaks with small spectral width.

$$Q = \frac{\lambda_0}{\delta\lambda} = \frac{\pi n L_c}{\lambda_0} \left( \arcsin \left( \sqrt{\frac{(1 - R_g e^{-\alpha L_c})^2}{4R_g e^{-\alpha L_c}}} \right) \right)^{-1} \quad (19)$$

In the case of distributed Bragg reflector cavity, as the reflection is distributed over a large number of grating periods (partial reflection for each period), the virtual cavity length

is now given by the sum of the distance between the two Bragg mirrors and the penetration depth into each of the two Bragg mirrors.

$$L_c = L_{cavity} + 2L_{pen} \quad (20)$$

For a uniform Bragg grating of length  $L_g$ , the penetration depth can be given by:

$$L_{pen} = \frac{\tanh(\kappa L_g)}{2\kappa} \quad (21)$$

where  $\kappa$  is the coupling coefficient of the Bragg grating which is discussed in the previous chapter [section 3.2](#). From Eq. (13,17,20), the condition where the cavity supports only one single resonant mode inside the stopband of the two identical waveguide Bragg gratings can be estimated by:

$$L_{cavity} < L_{lim} = \frac{\pi - 2 \tanh(\kappa L_g)}{2\kappa} \quad (22)$$

Thus, based on the graded-index Si<sub>1-x</sub>Ge<sub>x</sub> waveguide Bragg grating, a maximum cavity length for which the cavity keeps single mode operation is calculated as  $L_{lim} \approx 190 \mu\text{m}$  at a wavelength of  $8 \mu\text{m}$ . Following the theory and utilizing the analytical equations presented above, a Matlab script has been coded to simulate the performance of Fabry-Perot cavity.

A cavity length  $L_{cavity} = 70 \mu\text{m}$  is chosen mainly to localize the resonant peak at the center of the stopband of waveguide Bragg grating. To simulate the cavity performance, a lossless waveguide is considered ( $\alpha_{waveguide} = 0$ ). A Matlab simulation result is shown in [Fig.4.1.3\(a\)](#) for a cavity based on  $5\text{-}\mu\text{m}$ -width waveguide with two identical Bragg gratings whose grating periods are  $\Lambda = 1.1, 1.16 \mu\text{m}$ . The coupling coefficient is extracted by means of reproducing the EME simulated spectrum of Bragg gratings. Moreover, another simulation method using only EME solver has also been applied to verify the results obtained by Matlab script. In this case the full cavity is simulated. [Fig.4.1.3\(b\)](#) presents the EME simulated transmission spectrum of the Fabry-Perot cavities with the same parameters. A quite good agreement is obtained using the two different methods.

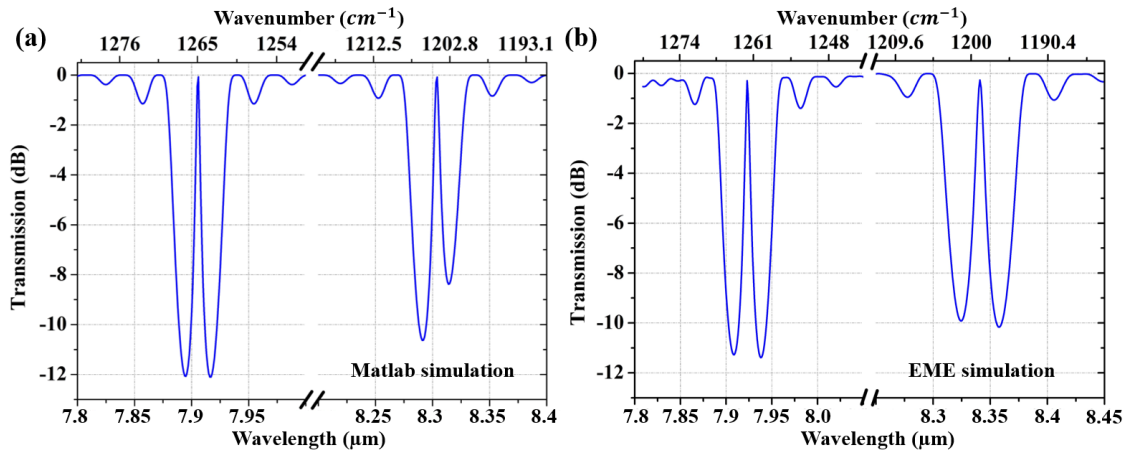


Fig.4.1.3. Simulated transmission spectrum of Fabry-Perot cavity (a) by Matlab script; (b) by EME solver for a cavity with 5- $\mu\text{m}$ -width waveguide, cavity length  $L_{\text{cavity}} = 70 \mu\text{m}$ , Bragg grating period  $\Lambda = 1.1 \mu\text{m}$  (left),  $1.16 \mu\text{m}$  (right), number of period  $N = 280$ .

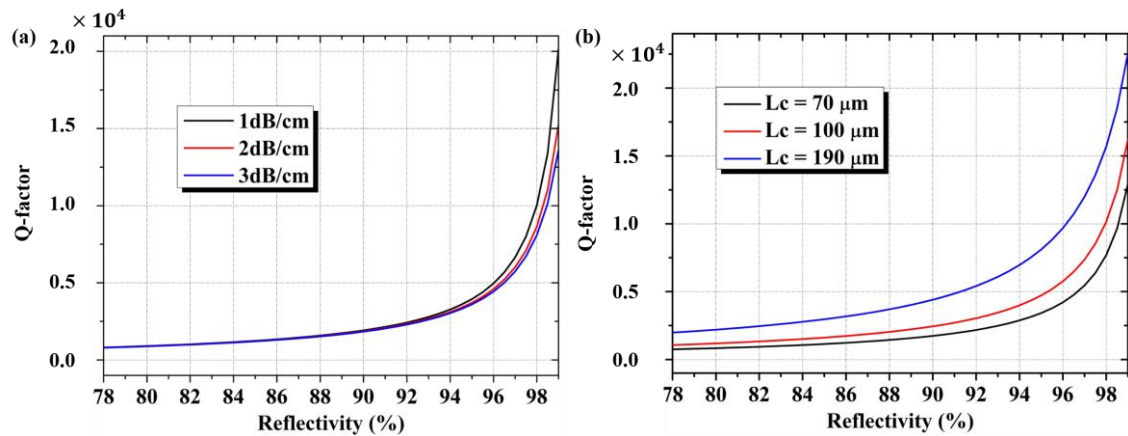


Fig.4.1.4. Evolution of Q-factor as a function of waveguide Bragg grating reflectivity (a) for different propagation losses at a Bragg wavelength  $\lambda_B = 8 \mu\text{m}$ ; (b) for different cavity distance with a propagation losses of 3 dB/cm.

Considering the measured performance of waveguide Bragg gratings as shown in [Fig.3.2.12](#), a Bragg grating rejection of between 7 and 20 dB is obtained. It corresponds in linear scale to a rejection of between 80% and 99%. [Fig.4.1.4\(a\)](#) shows the estimated Q-factor of Fabry-Perot cavity with a cavity length of  $70 \mu\text{m}$  as a function of Bragg grating reflectivity for different propagation losses (1, 2, 3 dB/cm), at a Bragg wavelength of  $\lambda_B = 8 \mu\text{m}$ . As can be observed, at low value of Bragg reflectivity ( $< 95\%$ ), the waveguide propagation losses have low impact on the Q-factor. The cavity Q-factor has a value in a

magnitude of  $10^4$ , if the reflectivity of Bragg grating is higher than 98%. As calculated by the Eq. (22), the cavity maintains single resonance mode inside the Bragg stopband while the cavity length is less than  $190 \mu\text{m}$ . The Q-factor can be thus improved by simply increasing the cavity length as shown in [Fig.4.1.4\(b\)](#). Q-factor could be higher than  $10^4$  if a Bragg grating reflectivity higher than 96% is achieved for a cavity with  $L_{cavity} = 190 \mu\text{m}$ .

#### 4.1.2. Fabrication

After the theoretical analysis and simulation, Fabry-Perot cavities based on the  $\text{Si}_{1-x}\text{Ge}_x$  waveguide Bragg grating have been fabricated using the same process described in the [section 3.2.2](#). Cavities with different parameters set have been fabricated: waveguide widths  $W_{WG} = 5 \mu\text{m}$ , two different grating periods  $\Lambda = 1.1, 1.16 \mu\text{m}$  for operation wavelength at  $8 \mu\text{m}$  and  $8.4 \mu\text{m}$ , number of period  $N = 280$ , cavity length  $L_{cavity} = 70 \mu\text{m}$ . [Fig.4.1.5](#) presents the SEM images of a representative fabricated cavity with  $\Lambda = 1.16 \mu\text{m}$ .

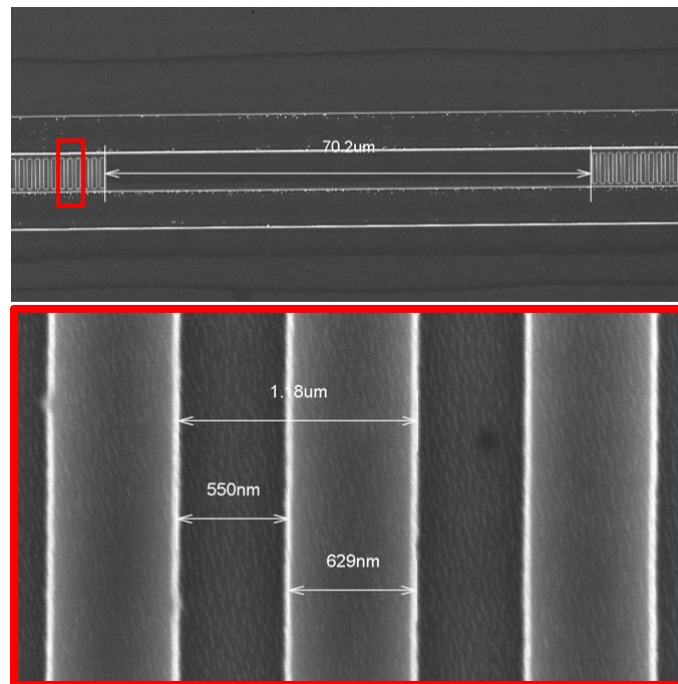


Fig.4.1.5. SEM images of fabricated Fabry-Perot cavity with  $L_{cavity} = 70 \mu\text{m}$ ,  $\Lambda = 1.16 \mu\text{m}$ ,  
DC = 0.5, N = 280.

### 4.1.3. Characterization

Fig.4.1.6 shows the measured transmittance spectrum of fabricated Fabry-Perot cavities which are obtained by normalizing the measured raw transmission spectrum of cavity over the transmission spectrum of a reference straight waveguide. The resonant peaks are localized at a wavelength of 7.95  $\mu\text{m}$  and 8.34  $\mu\text{m}$  that are in good agreement with the simulated results. The low rejection value comparing to simulation results of waveguide Bragg grating could be attributed to the non-equal value of low-index (etched) and high-index (non-etched) region in the gratings, which results in a duty cycle higher than 0.5 as shown in Fig.4.1.5. It thus leads to a lower value of coupling coefficient of the Bragg grating. Moreover, the maximum resonance transmission for both cavities ( $T_{max} = -1.37$  dB at 7.95  $\mu\text{m}$  and -1.25 dB at 8.34  $\mu\text{m}$ ) is caused by the waveguide propagation loss and the Bragg grating loss.

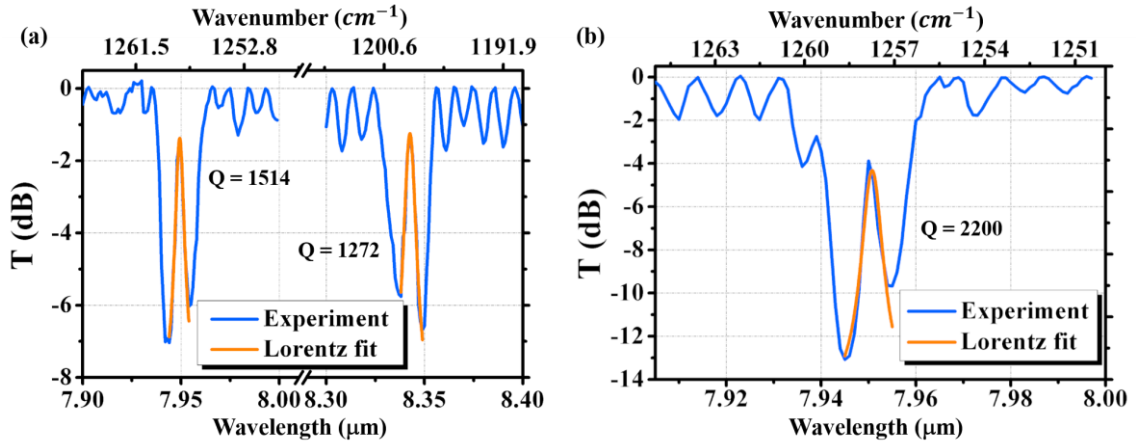


Fig.4.1.6. (a) Measured transmittance spectrum of two Fabry-Perot cavities with different parameters set: (left)  $\Lambda = 1.1$   $\mu\text{m}$ , (right)  $\Lambda = 1.16$   $\mu\text{m}$ ,  $N = 280$ ,  $L_{cavity} = 70$   $\mu\text{m}$ . (b) Measured transmittance spectrum of a cavity with  $\Lambda = 1.1$   $\mu\text{m}$ ,  $N = 500$ ,  $L_{cavity} = 70$   $\mu\text{m}$ .

To evaluate the property of the resonance, a Lorentzian function is used to fit the measured cavity resonance:

$$y = y_0 + \frac{1}{\pi} \frac{2\sigma}{4(x - x_0)^2 + \sigma^2} \quad (23)$$

where  $\sigma$  indicates the spectral width of the Lorentzian fitted curve which gives the -3-dB resonance bandwidth. Therefore, the measured FWHM of cavity resonance is equal to 5.3 and 6.5 nm for a cavity at 7.95 and 8.34  $\mu\text{m}$ , respectively. Then, the loaded cavity Q-factor can be calculated as 1514 and 1272, respectively.

Considering a waveguide propagation loss presented in [Fig.2.3.3\(c\)](#) for Platform B, of 3 dB/cm at 8  $\mu\text{m}$  wavelength, starting from the measured Q-factor, the Bragg reflectivity can be thus estimated according to Eq. (19). Bragg grating reflectivity values of around 88% and 85% are obtained for the mirrors with 280 periods. The cavity Q-factor can be improved by an increase of the cavity length at the expense of a smaller FSR or by increasing the Bragg grating reflectivity. A Fabry-Perot cavity using longer Bragg grating, keeping the same cavity length has been fabricated and characterized. In this case, the used Bragg grating has a number of period  $N = 500$ , the maximum cavity length for which the cavity keeps single mode operation is then calculated as 127  $\mu\text{m}$  because the penetration depth of a single Bragg mirror is also increased. Thus, the Fabry-Perot cavity using such 500-periods-Bragg-gratings is maintaining single resonance mode operation. The measured transmittance is shown in [Fig.4.1.6\(b\)](#). As can be observed, the -3-dB bandwidth at a wavelength of 7.95  $\mu\text{m}$  is reduced to 3.6 nm, which yields a loaded Q-factor of 2200. It corresponds to a Bragg reflectivity of about 92% which is lower than the rejection of the Bragg grating reported in the previous chapter in [Fig.3.2.13](#). Indeed a Bragg grating reflectivity up to 99% is expected, which should correspond to a Q factor of  $10^4$  assuming 3 dB/cm losses in the cavity.

The lower experimental Q-factor could be attributed to one of the following reasons or a combination of both: i) the limitation of the experimental set-up. The spectral width of the external cavity pulsed QCL is not known precisely but it is specified to be below  $1 \text{ cm}^{-1}$ . At 8  $\mu\text{m}$  wavelength this correspond to a maximum pulse width of 6.5 nm. Interestingly this value, compared to the measured 3.6 nm FWHM indicates that some limitation in the measured Q-factor can come from the experimental set-up. Furthermore, the wavelength scan for the transmission measurement has been performed in steps of 1 nm, attaining the maximum resolution of the QCL. Further experiments using a continuous (DC) operating mid-IR QCL with narrower spectral width, or using different technique based on cavity-ring

down spectroscopy for example should be performed to estimate the ultimate performance of the Bragg grating cavity ; ii) As a second reason, it is possible that the Bragg grating loss limits the achievable reflectivity. Indeed the rejection measurement reported in chapter 3 does not allow to dissociate the mirror reflectivity to the mirror loss. To confirm the issue, the mirror losses (grating loss) are estimated. Starting from the measured Q-factors and their maximum resonance transmission  $T_{max}$ , and assuming 3dB/cm propagation loss in the cavity, we can estimate an upper limit for the mirror losses of the three reported cavities, equal to 1.2%, 1.8% and 2.6%. It is clear that the level of losses can be compatible with the simulation reported in [section 3.2.1](#). Indeed during the design of the Bragg mirror, a value of losses below 5% was targeted which is obtained experimentally. To go further, this grating loss can be further reduced with a careful design of Bragg grating by playing with the etching depth of corrugations (ed) and the number of period (N).

#### **4.1.4. Cavities with lateral corrugations**

The Bragg gratings with top corrugations require two levels of fabrication process with good alignment between both steps. As an objective to ease the fabrication process, Fabry-Perot cavities using Bragg gratings with lateral corrugations have been designed and fabricated. A 3D schematic view of such cavity is shown in [Fig.4.1.7](#). In this approach, the grating corrugations and waveguide can be defined simultaneously by only one lithography and etching step. However, considering a 4  $\mu\text{m}$  waveguide etching depth, and the dimension of the corrugation (the period is about 1  $\mu\text{m}$ ), the typical aspect ratio of the corrugation should be around 1:8, which is also challenging in terms of fabrication.

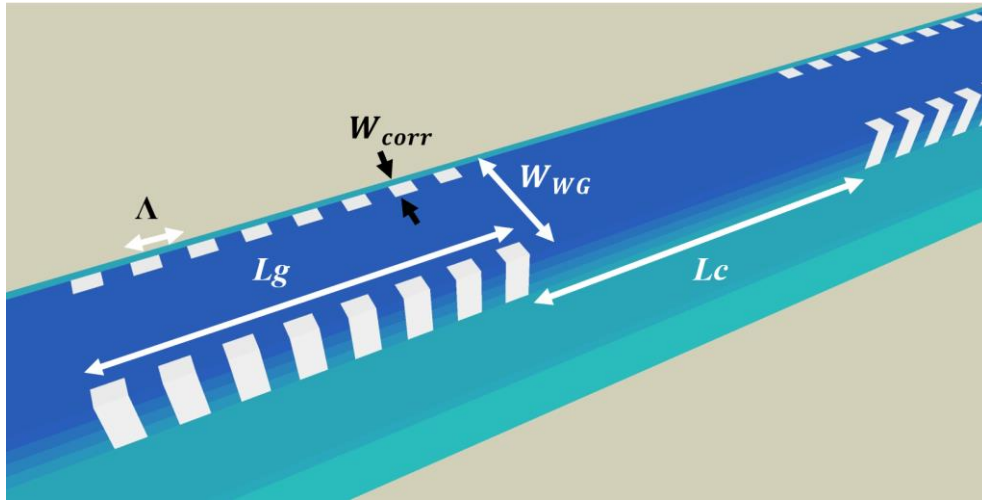


Fig.4.1.7. 3D schematic view of Fabry-Perot cavity using  $\text{Si}_{1-x}\text{Ge}_x$  waveguide Bragg grating with lateral corrugations.

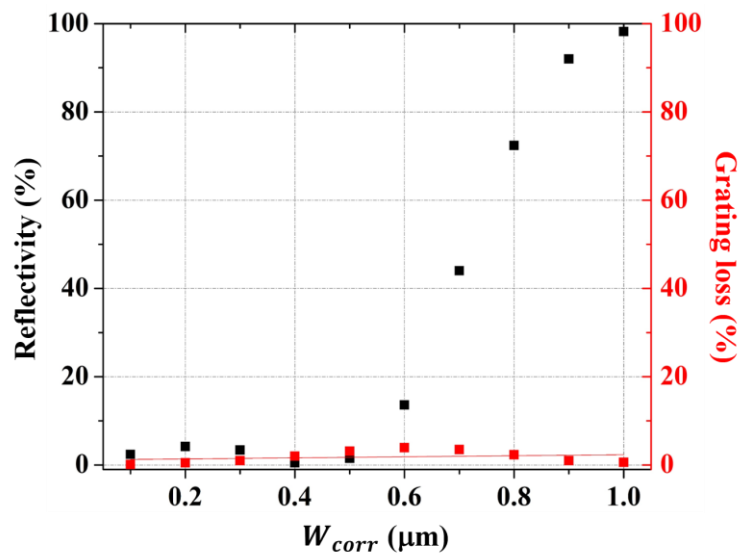


Fig.4.1.8. Simulated reflectivity and grating loss as a function of corrugation width of Bragg grating with lateral corrugations with  $N = 250$ .

In a point of view of device simulation, the cavity with lateral corrugations has been designed using the same method as discussed in the previous sections. [Fig.4.1.8](#) shows the simulated Bragg reflectivity and grating loss as a function of the corrugation width at each side of the waveguide. It is worth to note that the simulation is done for a  $5\text{-}\mu\text{m}$ -wide waveguide at a wavelength of  $7.5\text{ }\mu\text{m}$ . Thus the maximum value of  $W_{corr}$  of  $1\text{ }\mu\text{m}$  corresponds to a waveguide width of  $3\text{ }\mu\text{m}$  at low-index region in the gratings. As it can be

observed in [Fig 4.1.8](#), simulating a waveguide Bragg grating with 250 periods, the grating loss is always below 5%, and the Bragg reflectivity is obtained for the larger value of the corrugation used in the simulation, i.e. 1  $\mu\text{m}$ , a value of  $R = 98\%$  is obtained.

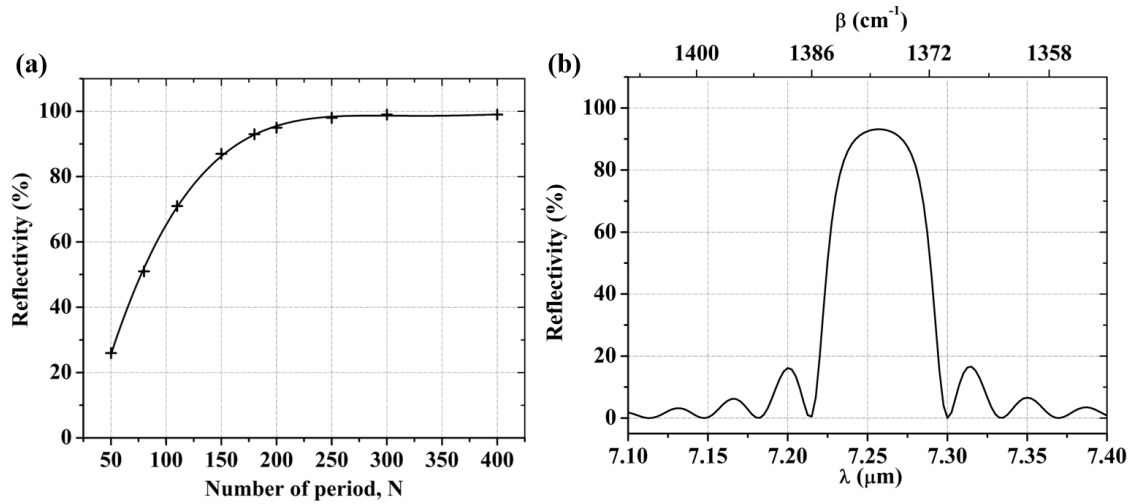


Fig.4.1.9. (a) Simulated Bragg reflectivity as a function of number of period; (a) Simulated Bragg reflectivity as a function of wavelength with number of period  $N = 180$ ; Both simulations are done with a period  $\Lambda = 1 \mu\text{m}$ , waveguide width  $W_{WG} = 5 \mu\text{m}$ , corrugation width  $W_{corr} = 1 \mu\text{m}$ .

[Fig.4.1.9](#) shows a representative simulation result of the Bragg grating with lateral corrugations of 1  $\mu\text{m}$  on both sides of the waveguide. The simulation is done in TE polarization in this approach since the TE mode has higher field overlap with lateral sides of the waveguides than the TM mode. As presented in [Fig.4.1.9\(a\)](#), with a number of period larger than 180, the Bragg reflectivity is higher than 90%. The reflectivity spectrum is plotted in [Fig 4.1.9 \(b\)](#), where a 64 nm stopband is observed.

In order to compare with the top corrugation approach, different cavities with lateral corrugated-Bragg grating have been fabricated, using the same parameter set: grating period  $\Lambda$  of 0.8, 1.02, 1.16  $\mu\text{m}$  are used, the number of period are  $N = 280$  and 500, and the cavity length  $L_{cavity}$  is fixed to 70  $\mu\text{m}$ .

The Fabry-Perot cavities using Bragg grating with lateral corrugations have been fabricated with an optimized e-beam lithography parameters set. Representative SEM images of fabricated cavity are shown in [Fig.4.1.10](#). It can be observed that the corrugations

and waveguide are well defined. Moreover the dimensions of obtained structure are very close to the targeted dimensions.

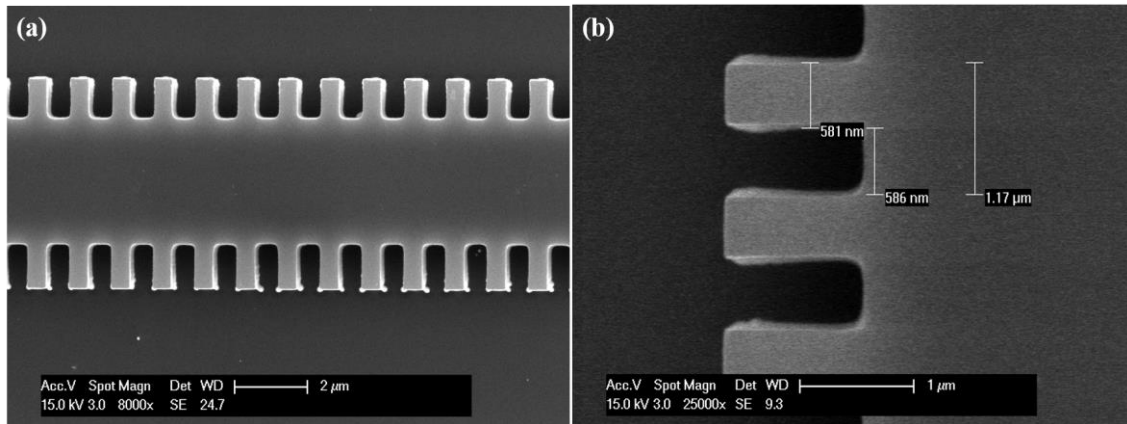


Fig.4.1.10. SEM images of fabricated Fabry-Perot cavity using Bragg grating with lateral corrugations, with a waveguide width  $W_{WG} = 5 \mu\text{m}$ , corrugation width  $W_{corr} = 1 \mu\text{m}$ , period  $\Lambda = 1.16 \mu\text{m}$ .

However, the measured transmission spectrum of all fabricated devices does not show any evident resonance. It is still not clear why the devices are not working properly, and it needs further investigations.

## 4.2. Racetrack Resonators

Besides the Fabry-Perot cavity using waveguide Bragg gratings, racetrack resonators have also been demonstrated based on the graded-index  $\text{Si}_{1-x}\text{Ge}_x$  waveguide. Racetrack resonators are a variant of ring resonators which are widely used in silicon photonics in the near-IR wavelength range, for many applications including modulation, frequency comb generation, spectroscopy and sensing to name a few [22,125–128]. Ring/racetrack resonators have been recently extended in the mid-IR wavelength range, and state of the art is summarized in [Table 4](#).

Concerning the mid-IR sensing applications, using resonators it is possible to take benefit from the attenuation of the maximum transmittance and/or the change of Q-factor of the resonance due to the optical absorption by the analyte to detect its presence and quantify its concentration.

The realization of high-Q MIR ring/racetrack resonators is challenging mainly due to: i) the minimum ring radius which is related to the operating wavelength and index contrast of the waveguide, ii) the fabrication of the directional coupler to couple light in the resonator. In this section, instead of ring resonator, the racetrack approach is chosen because of the low coupling coefficient at the coupling region for the classical ring resonator approach. Thus, racetrack resonators operating in long-wave infrared at 8  $\mu\text{m}$  wavelength have been demonstrated based on the graded-index  $\text{Si}_{1-x}\text{Ge}_x$  waveguide.

Ref.	Year	$\lambda$ ( $\mu\text{m}$ )	ER (dB)	Q-factor	Remarks
[129]	2010	5.5		$3 \times 10^3$	Silicon-on-sapphire
[45]	2013	4.4		$1.5 \times 10^5$	Silicon-on-sapphire; high Q-factor
[40]	2013	5.2	12	$10^5$	Chalcogenide, high Q-factor
[130]	2014	5.2	10	$3.7 \times 10^4$	$\text{CaF}_2$ substrate
[53]	2018	5	20	$2 \times 10^4$	Ge-on-SOI
[55]	2018	2	22	$5.7 \times 10^4$	Suspended Ge
[131]	2019	8	10	$3.2 \times 10^3$	Graded-index $\text{Si}_{1-x}\text{Ge}_x$ (this work)

Table 4. Overview of demonstration of MIR on-chip micro-resonators, ER: extinction ratio.

### 4.2.1. Analytical model and Simulations

A typical ring resonator is composed of a bus waveguide and a ring-shaped closed loop. [Fig.4.2.1](#) shows the schematic view of typical ring resonators with one or two bus waveguides.

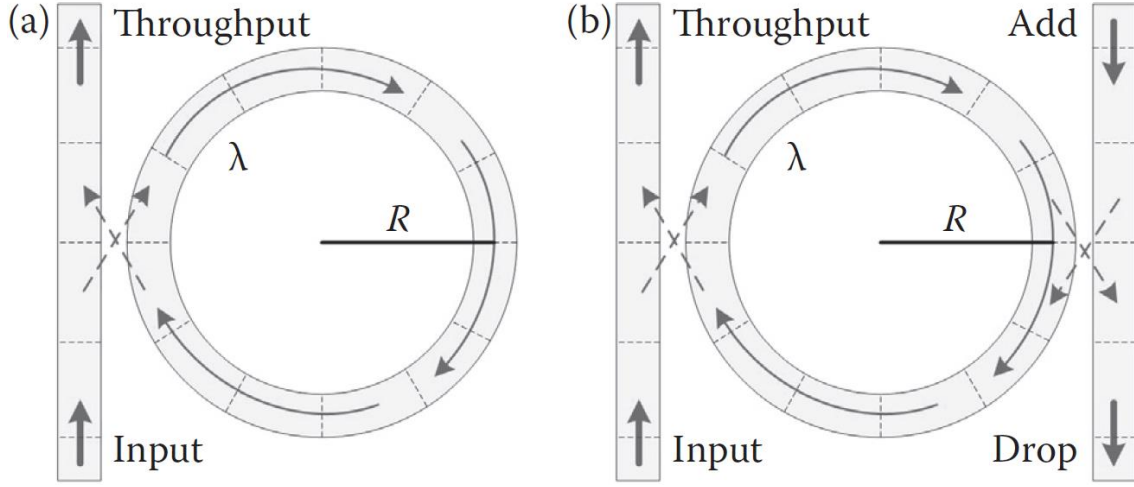


Fig.4.2.1. Schematics of waveguide coupled microring resonators (a) Notch filter (b) add-drop filter Ref. [132].

The resonance is given by the phased matching condition as:

$$k\lambda_k = n_{eff}L_c \quad (24)$$

where  $L_c$  is the round-trip cavity length,  $\lambda_k$  is the  $k^{\text{th}}$  order resonance wavelength with an integer number  $k$ . Considering the material dispersion, the spacing between two adjacent orders of resonance can be given by:

$$FSR = \frac{\lambda_k^2}{n_g L_c} \quad (25)$$

One important concept of the micro resonators is the coupling regime which depends on the balance between the bus waveguide coupling and the intrinsic cavity loss. Using the transfer matrix modeling, according to this balance, three regimes can be obtained: i) under coupling regime ( $t > a$ ) where the highest Q-factor can be obtained, ii) critical coupling regime ( $t = a$ ) where the largest extinction ratio (ER) can be obtained, and iii) over coupling regime ( $t < a$ ) where both the ER and Q-factor decrease, with the waveguide field transmission coefficient  $t$ , field coupling coefficient  $\kappa$  and amplitude round-trip loss coefficient  $a = \exp(-\alpha L_c/2)$  as shown in [Fig.4.2.2](#). Because of the symmetry of the matrix, the sum of square of the field coefficients is equal to 1 as  $|\kappa|^2 + |t|^2 = 1$ . Details on the transfer matrix modeling can be found in [132,133].

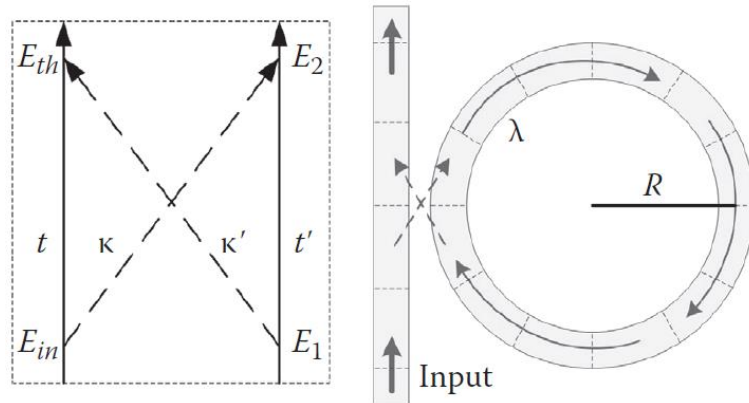


Fig.4.2.2. Schematic of a waveguide-coupled ring resonator-based notch filter, Ref. [132].

The most used method for light coupling between bus waveguide and the cavity is based on the evanescent field coupling. In a typical ring resonator light coupling occurs in a limited area approximately at one single point as shown in Fig.4.2.2. To achieve critical coupling, the gap between bus waveguide and the ring resonator must be close enough. As an example, for a ring resonator operating at telecom wavelength using typical strip waveguide on a 220-nm-SOI platform, the typical distance between bus waveguide and the ring is in the order of 100 nm. However, in the case of  $\text{Si}_{1-x}\text{Ge}_x$  waveguide for LWIR operation, the waveguide etching depth is of a few  $\mu\text{m}$ , and cannot be reduced at this is the condition to maintain a tight light confinement and thus small bending radius. With such etching depth, it is very challenging to achieve small gaps of around 100 nm. Therefore the distance between the ring and bus has to be larger, which will decrease the coupling of light from the bus waveguide to the ring resonator. In the following we thus considered a  $1\ \mu\text{m}$  gap as a conservative feasible distance, and racetrack resonators have been developed on the  $\text{Si}_{1-x}\text{Ge}_x$  waveguide. As a main difference with ring resonators, the localized coupling area is replaced by a directional coupler where the coupling length compensates for a wider gap between the ring and bus waveguide. In the following, the waveguide etching depth is also reduced to  $3\ \mu\text{m}$  instead of  $4\ \mu\text{m}$  to facilitate the coupling between bus waveguide and the resonator. Simulated coupling coefficients for different coupling length and wavelength are shown in Fig.4.2.3(a,b).

Considering previously reported 3 dB/cm waveguide propagation losses at  $8\ \mu\text{m}$  wavelength, a coupling length  $L = 200\ \mu\text{m}$ , the critical coupling can be obtained for a

resonator with 400  $\mu\text{m}$  radius. Moreover, taking into account the the measurable FSR of the experimental set-up, and the possible bending losses which needs to be systematically measured, the resonators with radii of  $R = 50, 100, 150, 200, 250 \mu\text{m}$  are fabricated for the first study of MIR  $\text{Si}_{1-x}\text{Ge}_x$  racetrack resonators.

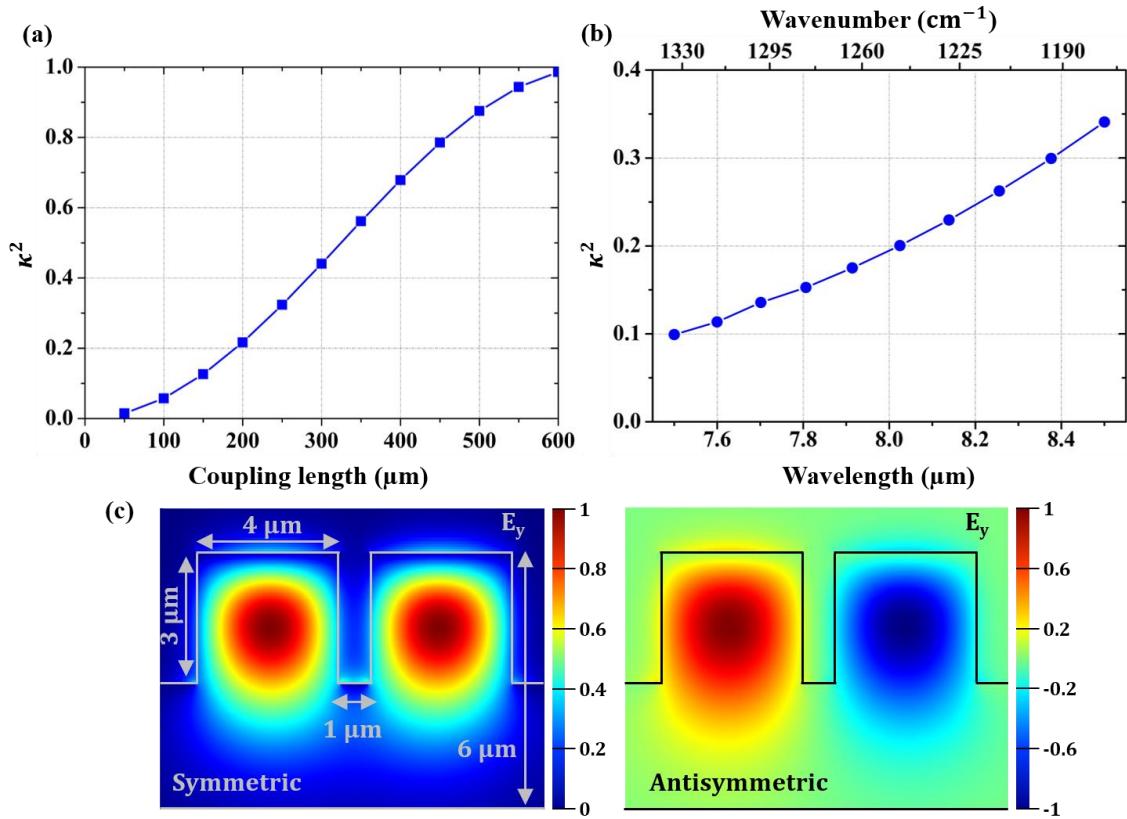


Fig.4.2.3. Simulated coupling coefficient  $\kappa^2$  for coupled waveguides with 1- $\mu\text{m}$ -gap (a) as a function of coupling length with  $\lambda = 8 \mu\text{m}$ ; (b) as a function of wavelength with  $L = 200 \mu\text{m}$ ; (c) Simulated coupled mode at a wavelength of 8  $\mu\text{m}$  for (left) even and (odd) quasi-TM mode.

## 4.2.2. Fabrication

The mid-infrared racetrack resonators have been fabricated using the same technique described in [section 3.2.2](#). The SEM images of the racetrack resonator with 100  $\mu\text{m}$  radius are shown in [Fig.4.2.4](#).

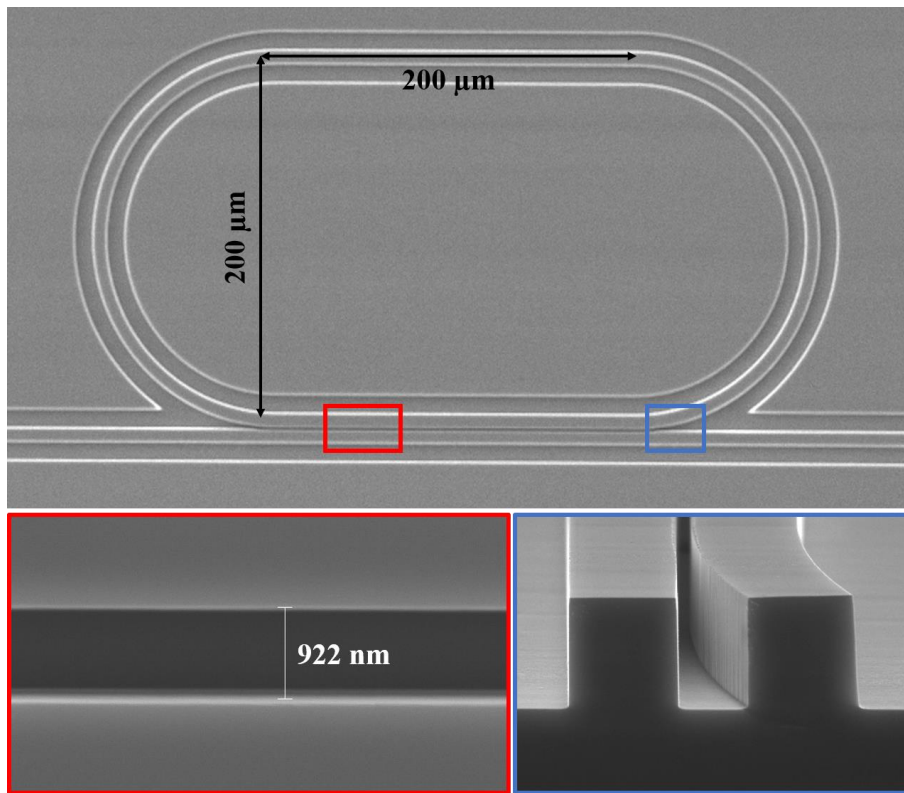


Fig.4.2.4. SEM images of racetrack resonator with 100  $\mu\text{m}$  radius, 200- $\mu\text{m}$ -long coupler.

### 4.2.3. Characterization

The racetrack resonators have been measured using the quantum cascaded laser in pulsed regime with a linewidth specified below  $1\text{ cm}^{-1}$  by a free-space configuration setup. [Fig.4.2.5\(a\)](#) summarizes the measured transmission spectrum of racetrack resonators operating in TM polarization with different bending radius  $R = 50, 100, 150, 200, 250\ \mu\text{m}$ . The shown spectra are obtained by normalization of the raw transmission spectrum over the transmission of a straight waveguide. Resonances can be observed in a broadband of about 900 nm around  $8\ \mu\text{m}$  wavelength. The characteristic interferometric pattern of ring resonators is observed, presenting periodic transmission dips that are sometimes partially clipped due to the limited resolution of our setup. It can be noted that the resonator with the lowest radius ( $R = 50\ \mu\text{m}$ ) shows a poor performance. In this case the resonance patterns show a multimode-like spectrum with an average drops of 4 dB. It can be attributed to a partial hybridization of the modes which results in a non-negligible conversion of the fundamental TM mode into TE polarization in agreement with the simulation (small  $\Delta n_{\text{TE-}}$

$T_M$ ). The resonators with  $R = 100 \mu\text{m}$  show also an asymmetric resonances which is equally attributed to a much weaker mode hybridization. Concerning the transmission response, resonators with radius larger than  $50 \mu\text{m}$  display an extinction ratio up to 10 dB. [Fig.4.2.5\(b\)](#) shows a representative zoomed view of a single resonance corresponding to the resonator with  $250 \mu\text{m}$  radius. Lorentzian function, Eq. (21) has been applied to fit the measured resonance, giving the FWHM of the resonance which is ultimately used to extract the loaded quality factor. A maximum loaded Q-factor of  $Q \approx 3200$  is obtained at a wavelength  $\lambda \approx 8.044 \mu\text{m}$  corresponding to a FWHM of 2.5 nm. Like the results obtained for Fabry-Perot cavity discussed in the previous section, considering the linewidth of the used QCL ( $< 1 \text{ cm}^{-1}$ ), the measured resonance response shape and Q-factor are most probably limited by the setup.

In order to verify the fundamental mode operation of the resonators with  $R > 50 \mu\text{m}$ , the free spectral range of resonances has been measured comparing to theoretical modal according to Eq. (23) with a cavity length given by  $L_c = 2\pi R + 2L_d$ . [Fig.4.2.6](#) presents the measured FSR (colored dots) of resonances for resonators with different radius in unit of  $\text{cm}^{-1}$  at different wavelengths, comparing with the calculated FSR (black lines) for a group index  $n_g = 3.8$ . As seen in the figure, larger FSR is measured for the resonators with smaller radius. The good agreement between experimental results and the modeling provides an evidence that the observed resonances correspond to a single mode operation of racetrack resonators.

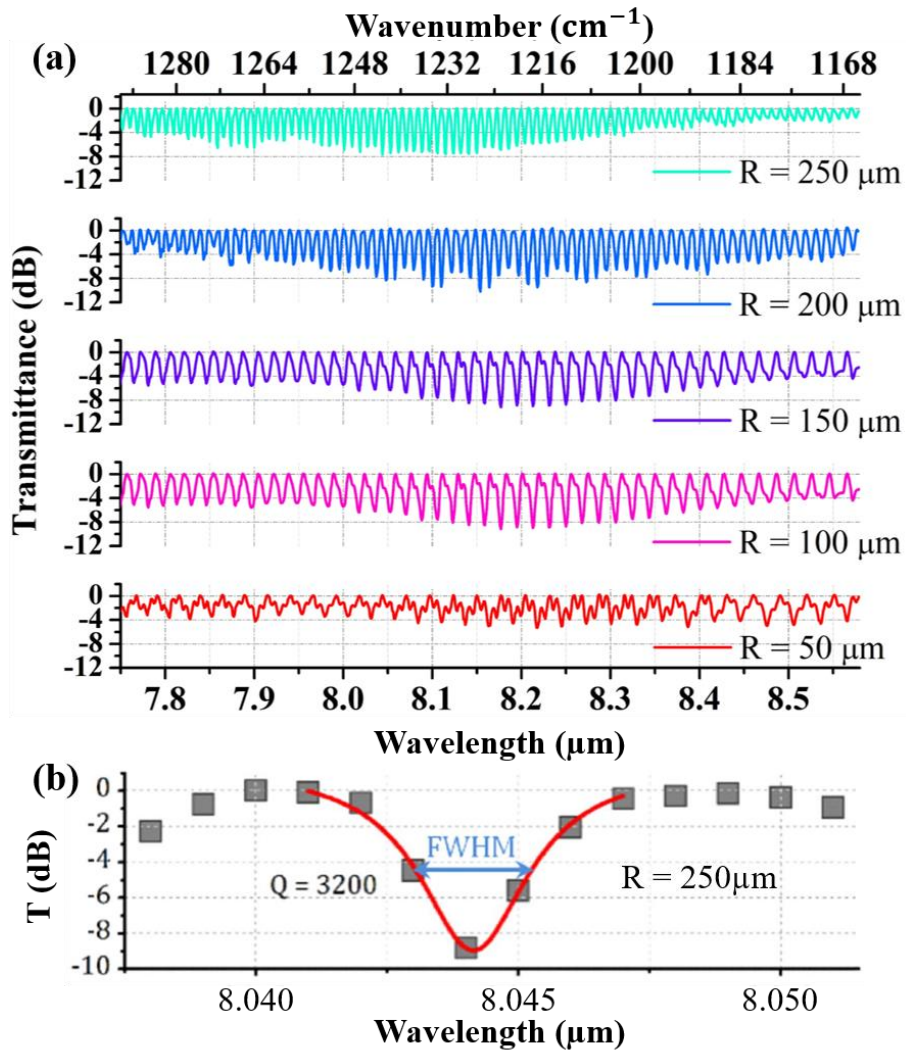


Fig.4.2.5. (a) Measured transmission spectrum of racetrack resonators with  $R = 50, 100, 150, 200, 250 \mu\text{m}$  operating in TM polarization; (b) Zoomed view of single resonance corresponding to a resonator with  $R = 250 \mu\text{m}$ , showing a Lorentzian fitting curve (red line).

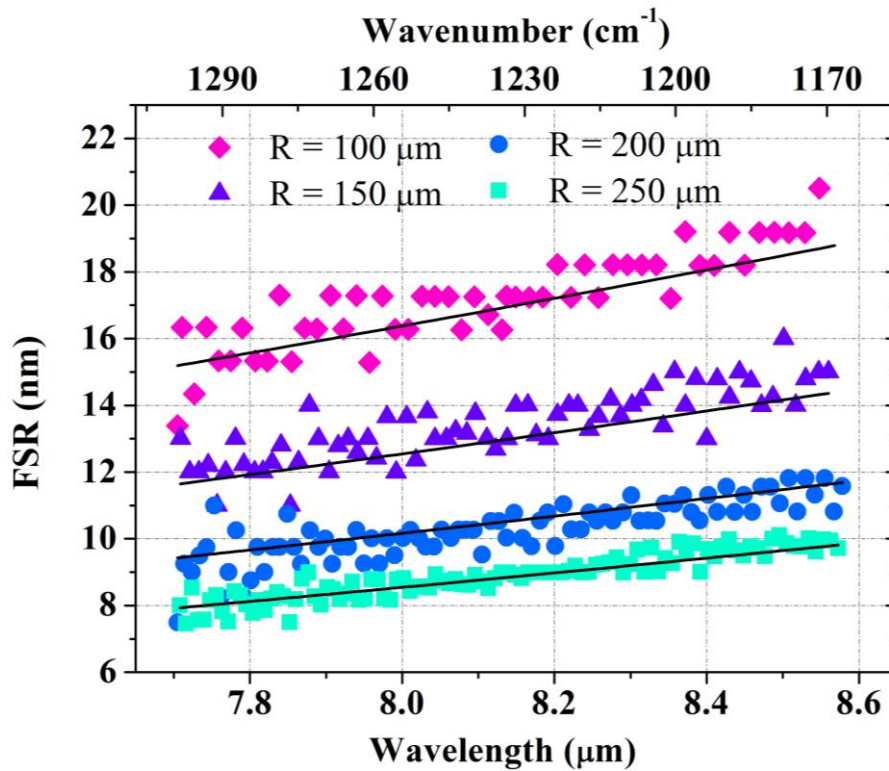


Fig.4.2.6. Measured FSR values as a function of wavelength for resonators with various bending radius (colored dots), and the calculated FSR (black lines) according to Eq. (23).

After the first experimental results of broadband MIR racetrack resonators, a second sample has been fabricated, varying the gap distance in order to achieve the ultimate performances of the resonators (narrow gap and deep-etching depth are targeted, in order to reduce the total resonator length, to increase the resonator FSR). The SEM images of this new sample are shown in [Fig.4.2.7](#). A minimum gap distance of about 300 nm has been successfully obtained, as shown in the SEM images in [Fig 4.2.7\(a\)](#). The etching depth of the gap is reduced in the same time due to a locally lower etching speed . This second racetrack resonators sample will be characterized soon.

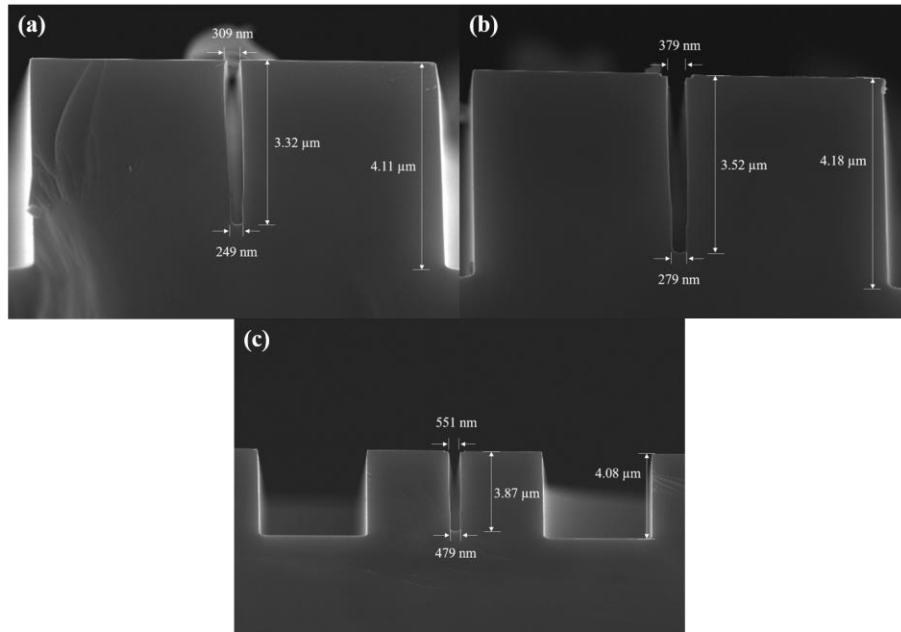


Fig.4.2.7 SEM images of fabricated racetrack resonator of a test sample with different gaps.

### 4.3. Conclusion

In this chapter, two types of integrated resonators, Fabry-Perot cavities and racetrack resonators have been demonstrated in the mid-infrared wavelength range. Firstly, Fabry-Perot cavities have been demonstrated by integrating two identical waveguide Bragg gratings as reflecting mirrors. Cavities with both top-corrugated and lateral-corrugated Bragg gratings have been successfully fabricated based on the  $\text{Si}_{1-x}\text{Ge}_x$  platform. The resonance has been observed for top-corrugated cavities at different wavelength, with a maximum Q-factor of 2200. Further study on the lateral-corrugated cavities needs to be done.

Secondly, the racetrack resonators operating in the LWIR wavelength range has been presented. Broadband operation over 900 nm at 8  $\mu\text{m}$  has been measured for resonators with bending radius larger than 50  $\mu\text{m}$ . A maximum Q-factor of 3600 is obtained at 8  $\mu\text{m}$ , with a device FSR of 9 nm. A second sample has been fabricated, and its characterization will allow us to systematically evaluate the influence of the gap distance and the coupling length on the resonator performances.

This first demonstration of MIR resonant structures on  $\text{Si}_{1-x}\text{Ge}_x$  opens the path for further development of MIR integrated photonic circuits, such as light source using non-linear effects, i.e. frequency comb generation. Moreover, as an example, applying the plasma dispersion effect to introduce phase modulation, resonators can be implemented as a building block for the modulation applications. Considering the atmospheric transparency window in the MIR wavelength range, the demonstration of MIR modulators shows high potential for the application of free-space telecommunication. Concerning the enhancement of light-matter interaction, MIR resonant structures present also good impact on the development of new generation multitarget molecular spectroscopic sensing systems.

## 5. Integrated mid-infrared Fourier-Transform Spectrometer

In terms of developing an on-chip IO sensor to achieve real-time and in-situ sensing, the integration of sensing circuits and on-chip spectrometer is particularly interesting. In the silicon photonics society, it exists already many demonstrations of on-chip integrated spectrometer based on the different approaches such as arrayed waveguide gratings [58,59,134–136], echelle gratings [126,137,138] or Fourier-transform-based spectrometers (FTS) [139,140]. In general, comparing to the AWG and echelle gratings, FTS or specifically the spatial heterodyne Fourier-transform spectrometer (SHFTS) provides high-resolution spectral retrieval, exploiting seamless phase and amplitude corrections to substantially relax the fabrication tolerances. Moreover, with a multi-aperture configuration, the SHFTS shows the beneficial of high-throughput. In this chapter, on-chip integrated SHFTS is demonstrated based on the  $\text{Si}_{1-x}\text{Ge}_x$  platform, showing an unprecedented broadband dual polarization operation for one single chip from 5 ( $2000\text{ cm}^{-1}$ ) to  $8.5\text{ }\mu\text{m}$  ( $\sim 1170\text{ cm}^{-1}$ ). An experimental resolution of better than  $15\text{ cm}^{-1}$  is obtained for both orthogonal polarizations. The on-chip FTS demonstration concerning theoretical modeling, device design, fabrication and characterization will be presented.

### 5.1. Introduction of Fourier-Transform infrared Spectroscopy

Since the first study of infrared spectra by Sir William Herschel in 1800 [141], the infrared spectroscopy, more precisely the Fourier-Transform infrared (FTIR) spectroscopy becomes nowadays one of the most versatile and widely useful analytical tool for the application of molecular structure identification and many others. It is unique in its range of applicability to samples of every phases (gas, liquid or solid) because molecular vibration-rotation frequencies are little affected by inter-molecular interactions. In a simplest configuration, as the schematic shown in [Fig.5.1.1](#), a FTIR is in principle a combination of

the Michelson interferometer and Fourier-transform (FT) mathematical analysis, where the interferogram is generated by the optical path difference between two coherent beams by scanning one of the two mirrors. Then, the signal at each wavelength can be recovered through the Fourier Transformation of the measured interferogram.

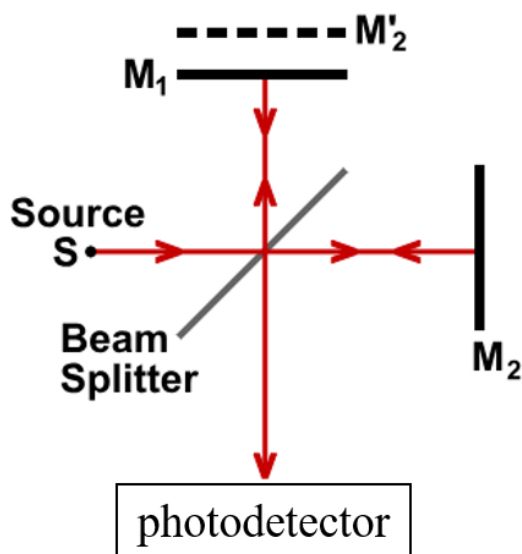


Fig.5.1.1. Schematic of Michelson interferometer

Among many infrared spectroscopy techniques, the major advantages of FTIR are: i) Fellgett multiplex advantage – it refers to the principle of simultaneously collecting information in all wavelengths; ii) high energy-throughput over dispersion spectrometers known as Jacquinot advantage [142]; iii) Conne advantage – it indicates the intrinsic wavelength calibration of the FT spectrometer [143]. Thus, it is widely used for a large number of applications, including food safety, remote sensing for pollution detection or industry process control, medical diagnosis [144,145], astronomy or security and many others.

However, for some applications the FTS suffers also several disadvantages. For example, in the case of high-resolution FTS, it requires long scanning time to obtain large sampling points for which the two mirrors in the interferometer must remain accurately parallel for a long mirror travel. To do so, it requires an extremely precisely control of the moving element. For the astronomic application, more precisely the satellite instrumentation, the moving element in a non-gravity space is very challenging.

To avoid using any moving element, a spatial heterodyne approach has been proposed and demonstrated [146]. The two mirrors in the interferometer are then replaced by tilted diffraction gratings as schematically shown in [Fig.5.1.2](#). In this approach, two wave-fronts reflected from the two gratings, exit the interferometer with a wavenumber-dependent crossing angle between them for each wavenumber in the wavefront. When the two wave-fronts recombine at a photodetector, the interference fringes known as Fizeau fringes are created, which represent the FT of the spectrum of the light source. The heterodyne wavenumber is known as the Littrow wavenumber, where two wave-fronts are parallel with zero spatial frequency in which the output transmission produces a constant interference fringe pattern. The interference for various optical path differences is thus obtained simultaneously and the interferogram is recorded without any moving element. Thus, in addition to the advantage of conventional FTS, the spatial heterodyne Fourier-Transform spectroscopy (SHFTS) benefits also from inherent mechanical stability.

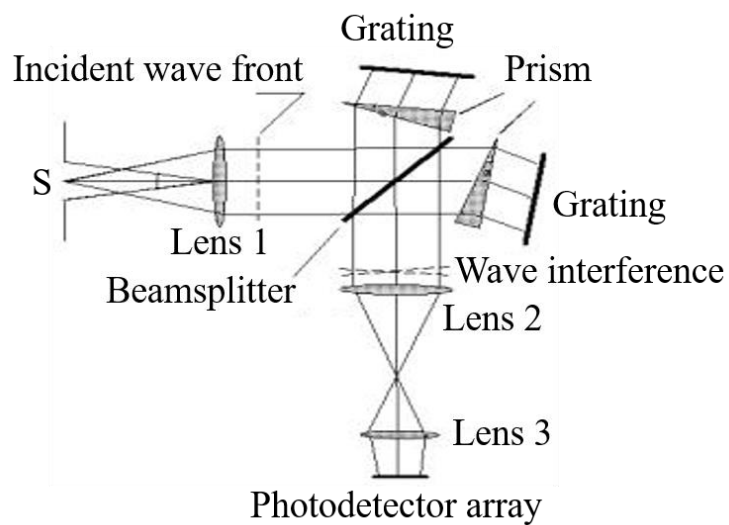


Fig.5.1.2. Schematic of spatial heterodyne spectrometer, readapted from [147].

## 5.2. Integrated broadband $\text{Si}_{1-x}\text{Ge}_x$ Fourier Transform Spectrometer

Although, the SHFTS shows good performance comparing to conventional FTS, the large size and weight of the device limit its application on, for example the space instrumentation. In this context, an on-chip integrated spectrometer using silicon photonics present definitive advantages, as it provides much smaller device size, light weight and low power consumption ([Fig.5.1.3](#)).



Fig.5.1.3. Comparison of conventional bulky Fourier-Transform spectroscopic system and on-chip integrated system.

In terms of on-chip integration, the interference fringe patterns can be generated using the asymmetric Mach-Zehnder interferometers (MZI) where the phase difference is introduced by the optical path difference between two arms. Up to now, there are already many demonstration of integrated FTS based on the SOI platform, benefiting the mature fabrication technology compatible with near-infrared and short-wave infrared (SWIR) spectral range. Therefore, state-of-the-art integrated FTS have shown operation mainly in the telecom wavelength at  $1.55 \mu\text{m}$  and SWIR region below  $4 \mu\text{m}$  wavelength. [Fig.5.1.4](#) presents the recent demonstrations of on-chip integrated FTS. A. V. Velasco et al. demonstrated FTS using MZIs with long spiral wavelength introducing large optical path difference (OPD) to realize high resolution up to  $42 \text{ pm}$  at  $1.55 \mu\text{m}$  [139]. D. M. Kita et al. investigated digital FTS by utilizing reconfigurable MZI, and collaborating with machine

learning regularization techniques to overcome the limitation of spectral channel count [148].

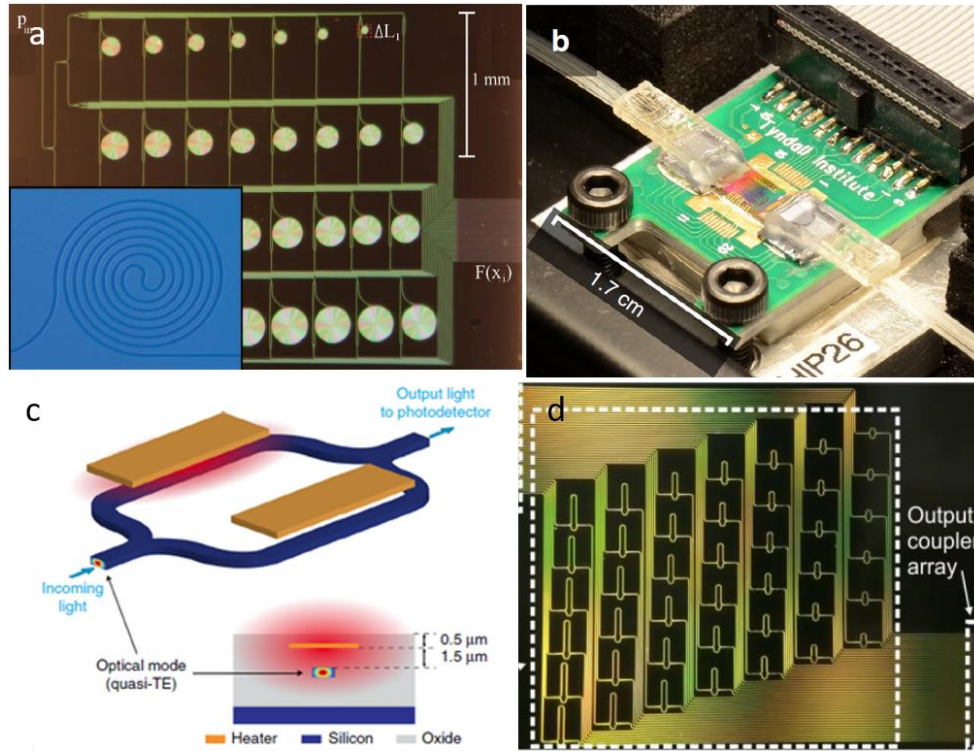


Fig.5.1.4. On-chip integrated Fourier-Transform Spectrometer (a) with 32 channels operating at 1.55  $\mu\text{m}$ ; (b) digital approach; (c) with wavenumber-temperature-dependent interferogram; (d) with 42 channels operating at 3.75  $\mu\text{m}$ .

As another approach, instead of generating different optical paths spatially by an asymmetric MZI array, and benefiting from the thermal-optic property of silicon, M. C.M.M. Souza et al. demonstrated FTS generating the different optical paths by thermo-optic switching in a single MZI [149]. However, all mentioned on-chip FTS present operation in the NIR at 1.55  $\mu\text{m}$ . Interestingly, M. Nedeljkovic demonstrated a 42 channels FTS operating at 3.75  $\mu\text{m}$  wavelength [35], however there is not yet on-chip FTS operating in the LWIR fingerprint region. Moreover, in the different reported works, operation is limited to single polarization due to the polarization dependence of the MZIs. However it is challenging to control the polarization of collected light from an environment for applications like sensing in space satellites or unmanned aerial vehicles [150], thus dual-polarization operation is highly desirable.

During this PhD thesis, I develop the first LWIR FTS based on the Ge-rich  $\text{Si}_{1-x}\text{Ge}_x$  platform [151]. The device design, fabrication and characterization of the  $\text{Si}_{1-x}\text{Ge}_x$ -based FTS will be discussed in the next sections.

### 5.2.1. Modal analysis and design

The MIR  $\text{Si}_{1-x}\text{Ge}_x$  integrated SHSFT spectrometer, is based on an array of MZI with different phase delay as schematically shown in Fig.5.2.1. The FTS is composed of  $N$  MZIs with a path delay linearly increasing from 0 (balanced MZI with  $\Delta L_0 = 0$ ) to a maximum physical path delay of  $\Delta L_{max}$  by an interval of  $\Delta L$ . A multiaperture configuration is used as it benefits the advantage of  $N$  times higher energy throughput compared to a single-aperture configuration.

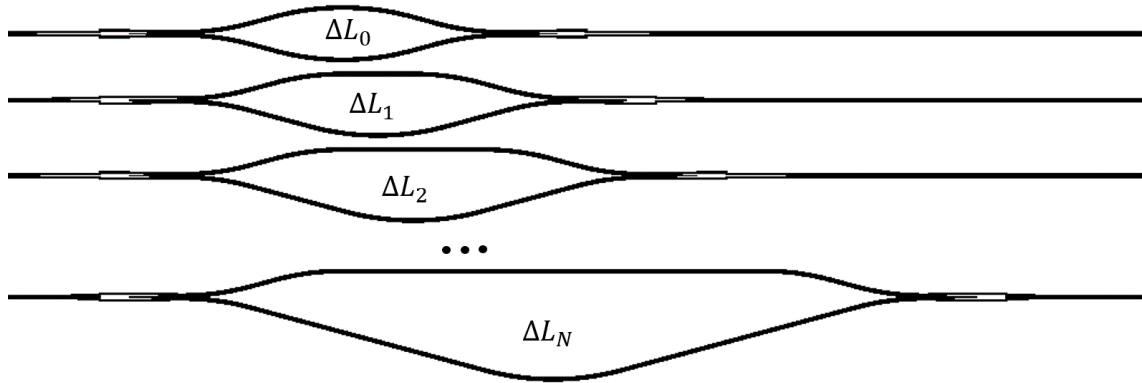


Fig.5.2.1. Schematic view of the on-chip spectrometer based on arrayed MZIs.

In principle, for a given monochromatic signal, the light is coupled into each individual MZI. The different characteristics of each MZI with different optical path differences result in different powers at the output of each MZI. Like the bulk SHFTS with diffraction gratings, the MZI array can be designed for a particular Littrow wavenumber  $\sigma_L$ . At the Littrow wavenumber, the OPD in different MZIs are integer multiple of  $2\pi$ , thus yielding a constant transmission output for all MZIs. Then wavenumber equally spaced above and below Littrow wavenumber produce the same fringe pattern which results in a symmetry centered at Littrow wavenumber. Thus, the arrayed MZIs provides unique fringe patterns within a limited spectral range which can be denoted as the free spectral range (FSR) of the spectrometer. Therefore, this spectral range can be calculated as half of the spectral spacing

between two adjacent Littrow wavenumbers corresponding to two adjacent diffraction orders in the case of bulk diffraction-grating-based SHFTS.

In a general configuration of Fourier Transform spectrometry, for the case of infinite path delay, when a continues source is used, the relation between output interferogram  $I(x)$  for a given wavenumber and the density spectrum of light source  $s$  can be given by the cosine Fourier transform [143]:

$$\begin{cases} I(x) = \int_{-\infty}^{+\infty} s(\bar{\sigma}) \cos(2\pi\bar{\sigma}x) d\bar{\sigma} = \int_0^{+\infty} s(\bar{\sigma}) \cos(2\pi\bar{\sigma}x) d\bar{\sigma} \\ s(\bar{\sigma}) = \int_{-\infty}^{+\infty} I(x) \cos(2\pi\bar{\sigma}x) dx = 2 \int_0^{+\infty} I(x) \cos(2\pi\bar{\sigma}x) dx \end{cases} \quad (24)$$

where  $x$  is the optical path delay of the interferometer and  $\bar{\sigma} = \sigma - \sigma_L$  is the shifted wavenumber.

In practical implementation of on-chip spectrometers, the spatial interferogram is discretized at  $N$  equally spaced delay corresponding to each MZI as shown in [Fig.5.2.1](#). Thus the optical phase delay for  $i^{\text{th}}$  MZI can be calculated as:

$$x_i = n_g(\sigma) i \Delta L \quad (25)$$

where  $n_g$  is the group index at each wavenumber and  $\Delta L$  is the path difference between two adjacent MZIs ( $\Delta L_n - \Delta L_{n-1} = \Delta L$ ). Then, by analogy to the integral formula Eq. (24), the input source spectrum can be calculated by the discrete cosine Fourier transform:

$$s(x_i) = \Delta L \cdot S + 2 \sum_{i=1}^N I(x_i) \cos(2\pi\bar{\sigma}x_i) \Delta L \quad (26)$$

where  $S$  is the input source power. For a uniform illumination of multiaperture input, the input power is constant for all input waveguides  $S(x_i) = S$ . In general, due to the different coupling coefficient of each input waveguide, the illumination is non-uniform. The error on power value of input source can be eliminated by normalization of the interference over the measured signal of a reference straight waveguide. Alternatively, people also use the complementary output powers to calculate the exact value of input power (instead of using a  $2 \times 1$  beamsplitter at the MZI output, a  $2 \times 2$  beamsplitter is used to be able to measure complimentary output powers at two output ports) [152]. To simplify the data processing, the first method is chosen for the demonstration of MIR  $\text{Si}_{1-x}\text{Ge}_x$  SHFTS.

The essential properties of FTS dominating the design of integrated spectrometer is the spectral resolution ( $\delta\nu$ ) and the spectral range of the device (FSR). The spectral resolution describes the ability of FTS to resolve two monochromatic input signals. The most popular criterion of spectral resolution is the full width at half maximum (FWHM) of the reconstructed monochromatic signal. The FSR denotes the device bandwidth in which the FTS is able to resolve the input signal. For an on-chip FTS composed of  $N$  MZIs with the optical path difference linearly increasing with equally intervals, the resolution and spectral range are determined by the maximum and minimum phase delay, respectively [35].

$$\delta\nu = \frac{1}{\Delta L_{\max} n_g} \quad (27)$$

$$FSR = \frac{\delta\nu N}{2} = \frac{1}{2n_g \Delta L_1} \quad (28)$$

As can be seen from Eq. (26), an unknown input spectrum can be obtained by the discrete cosine Fourier transform of the measured interferogram. However, in practice, environment such as temperature would introduce phase errors to the measured interferogram which affects the reliability of the Fourier transform. It yields thus a non-correct input spectrum retrieval. In the conventional approach, additional active compensation technique is applied to correct the phase errors. To ease the spectrum retrieval process, different reconstruction algorithms have been proposed such as Moore-Penrose method, basis pursuit denoising (BPDN), least absolute shrinkage and selection operator (LASSO), and many others [148]. Among them, Moore-Penrose method which does not require any hyperparameters determination is applied for the demonstration of our MIR Fourier transform spectrometer. Based on a system of linear equations, within the device FSR, the interferogram of arrayed MZIs can be described by:

$$I(x_i) = S \times T \quad (29)$$

where  $T$  is the transformation matrix which is determined by the device. Then, the input source spectrum  $S$  can be obtained by the multiplication of the measured interference  $I(x_i)$  and the pseudoinverse of the transformation matrix  $T^+$ .

For the first demonstration of SiGe MIR Fourier transform spectrometer, an array of 20 MZIs is used (1 balanced + 19 unbalanced MZI), corresponding to a total footprint of

1.5 cm<sup>2</sup>. A maximum path-length difference of  $\Delta L_{max} = 178.6 \mu\text{m}$  is used, given a theoretical resolution of 13.8 cm<sup>-1</sup> and an FSR of 132 cm<sup>-1</sup>. It is worth to note that this FSR and resolution calculation is done at  $\lambda = 7.5 \mu\text{m}$  wavelength with a simulated group index of  $n_g = 4.04$  based on the platform A (waveguide cross-section in [Fig.2.1.1](#)).

## 5.2.2. Fabrication

The MIR spectrometer is designed based on the waveguide of platform A which consists of a 11- $\mu\text{m}$ -thick graded buffer and a 2- $\mu\text{m}$ -thick Si<sub>0.2</sub>Ge<sub>0.8</sub> constant layer. To properly fabricate the multimode interferometer (MMI), the key component of the designed FTS, ebeam lithography has been used to pattern the structures. Detail on fabrication process can be found in the previous chapter in [section 3.2.2](#) as the process for definition of waveguide. [Fig.5.2.2](#) presents a global view of the optical microscope image of the fabricated FTS captured using digital VHX microscope with high resolution. The inset shows a representative SEM image of the MMI. The bending radius is chosen as large as 1.2 mm to strictly avoid bending losses. It can be noted that with a systematically study of the bending losses, the bending radius can be further decreased to reduce the total footprint of the device. Moreover, like in the case of other devices discussed in the previous chapters, a bent waveguide is used at the output of the chip to avoid the detection of scattering light due to direct coupling at the waveguide input.

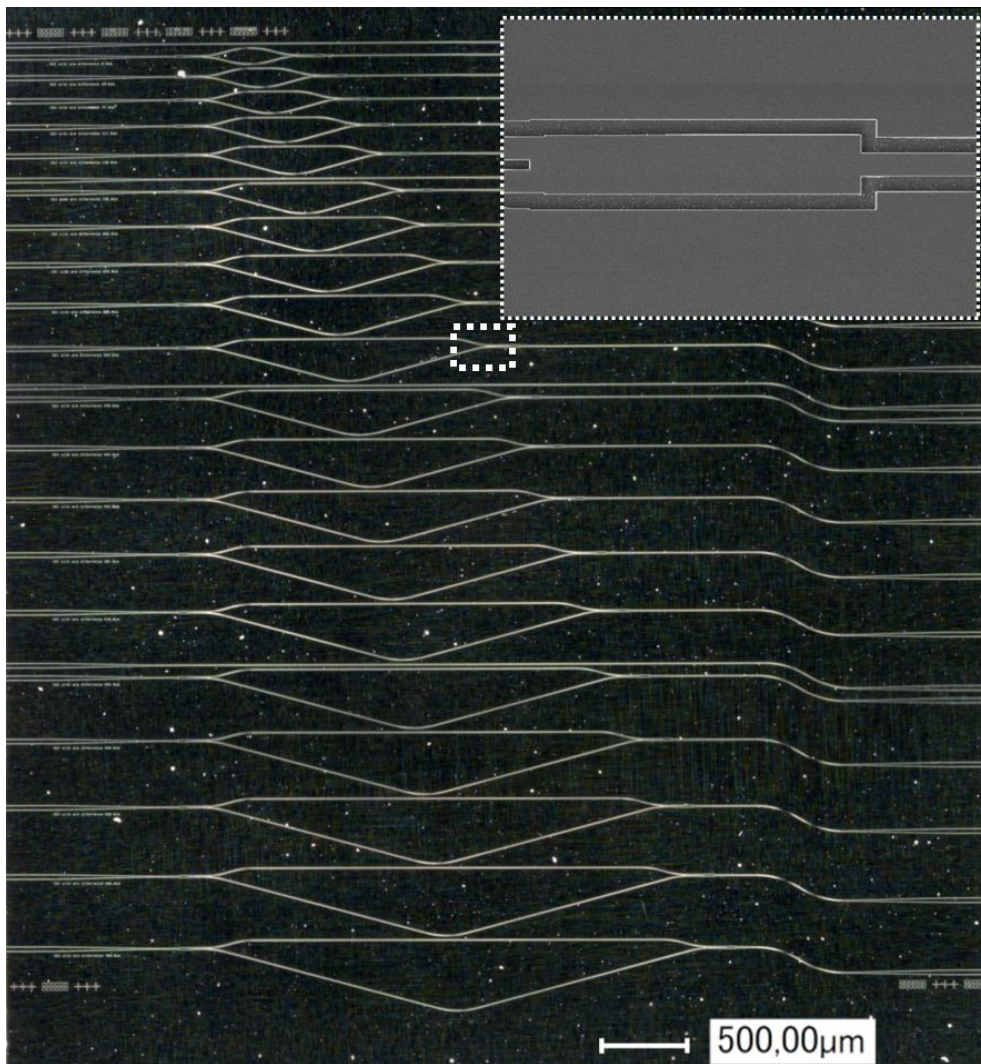


Fig.5.2.2. Optical microscope image of the fabricated MIR  $\text{Si}_{1-x}\text{Ge}_x$  Fourier transform spectrometer; (inset) Scanning electron microscope (SEM) image of a multimode interferometer as the beamsplitter. The fabricated sample is composed of 20 MZIs with optical path difference linearly increasing from 0 to 178.6  $\mu\text{m}$ , and reference straight waveguides.

### 5.2.3. Characterization

The fabricated sample has been measured using the free-space configuration set-up described in [section 2.3.1](#). To validate the performance of the fabricated mid-infrared SHFTS, transmission measurement has been done for each MZI at different wavelengths in a range from 5  $\mu\text{m}$  ( $2000\text{ cm}^{-1}$ ) to 8.5  $\mu\text{m}$  ( $\sim 1176\text{ cm}^{-1}$ ) to construct the transformation matrix of the device. Data processing is performed to remove imperfections from the raw

measurements, like the frequency dependence of the laser power and the atmospheric absorption lines detected by the free-space measurement. From the raw measurement, the data processing comprises mainly three steps as an example illustrated in Fig.5.2.3. The black curve in Fig.5.2.3(a) is obtained by normalization of the measured raw spectrum over the reference straight waveguide transmission. Then a subtraction of its mean value (red curve) is applied to obtain the zero-baseline curve (blue curve in Fig.5.2.3(b)). Finally, the quasi-ideal cosine-like interference is obtained by dividing the zero-baseline curve over its envelop function. It is worth to note that the insertion loss of the MZI is measured to be less than 1 dB for the full range of the characterization for both TE and TM polarizations.

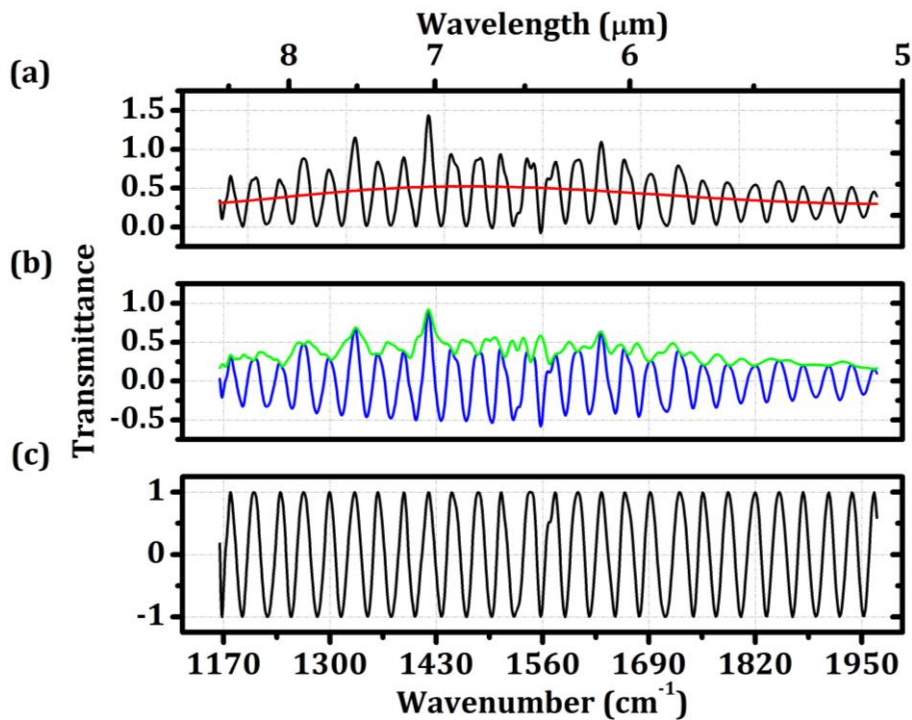


Fig.5.2.3. Example of an interferogram pattern from the MZI with  $\Delta L_0 = 84.6 \mu\text{m}$  for TE polarization. The mean value [red curve in (a)] and the envelop wavefunction [green curve in (b)] are subtracted to obtain the curve shown in (c).

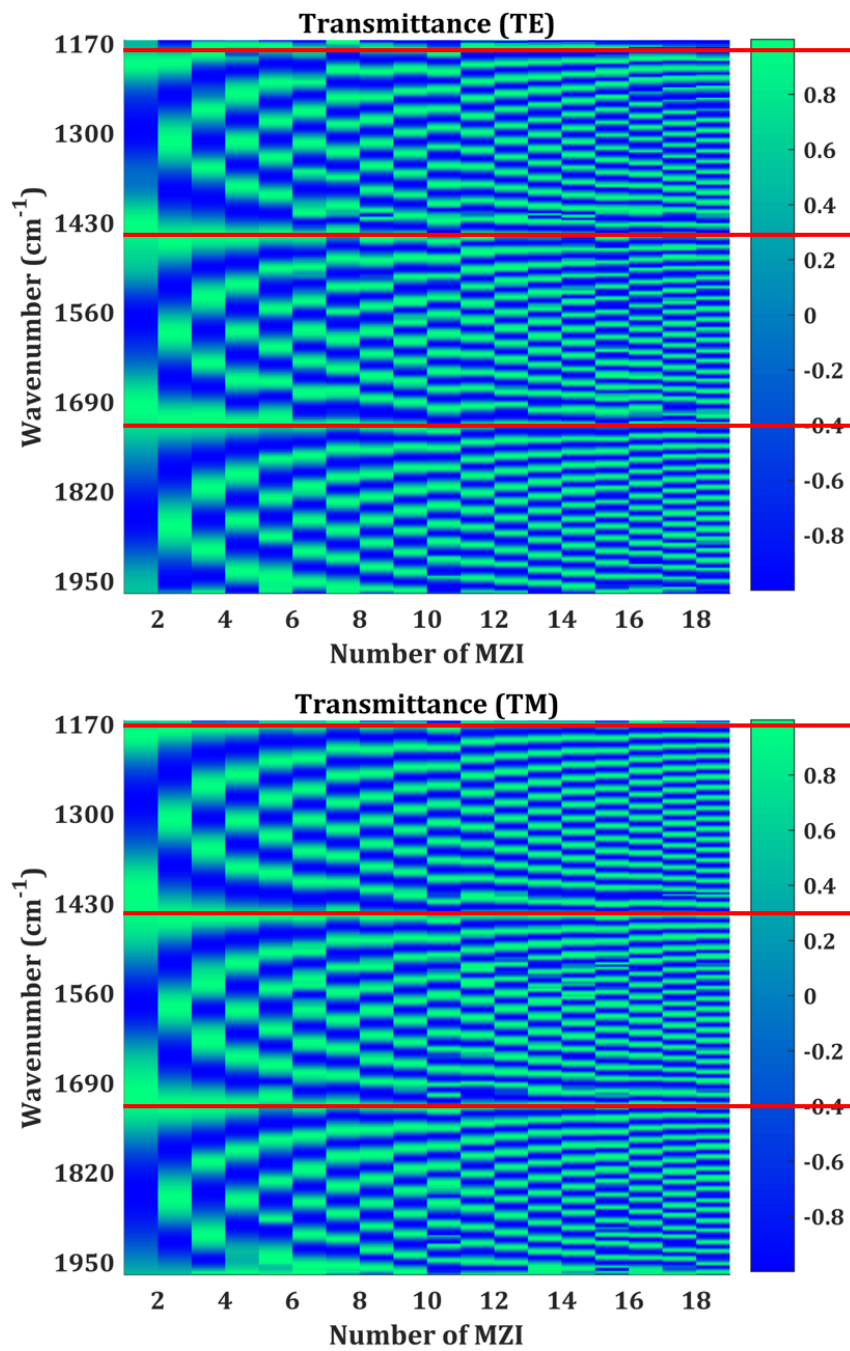


Fig.5.2.4. Calibrated interferogram of the measured arrayed MZIs for (top) TE and (bottom) TM polarizations; red lines present the measured Littrow wavenumbers where all MZIs achieve a maximum transmittance.

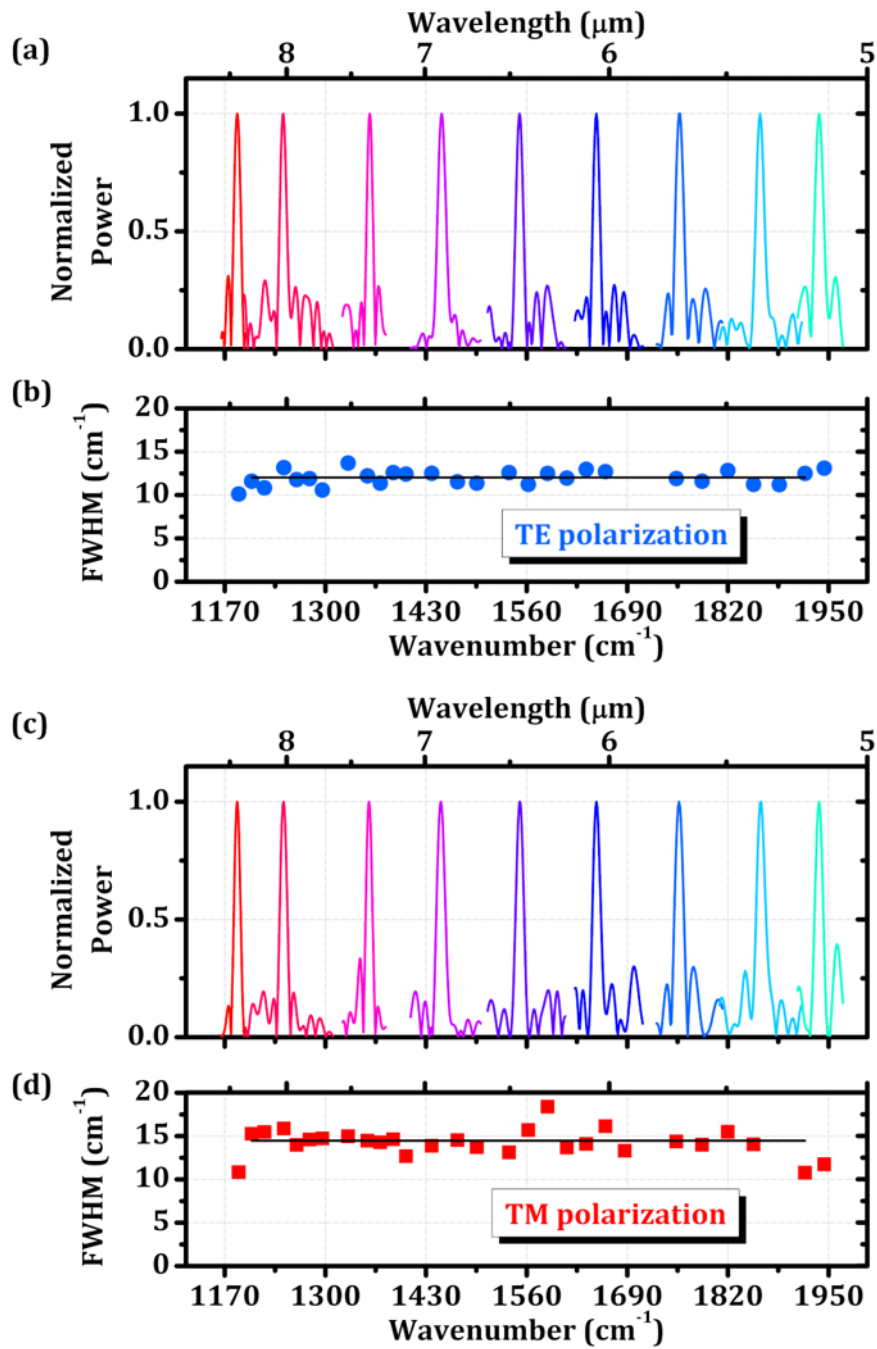


Fig.5.2.5. Experimentally retrieved spectra for a monochromatic input scanned between 1170 and 1950  $\text{cm}^{-1}$  for TE (a) and TM (c) polarizations; (b) and (d) report the FWHM of the retrieved signals in TE and TM polarization, respectively [153].

Applying this data treatment to all MZIs in both TE and TM polarizations, it is possible to construct the final calibrated transformation matrix as shown in [Fig.5.2.4](#) for both orthogonal polarizations. It can be observed that the MZIs show operation in a very large wavelength range over  $800 \text{ cm}^{-3}$  (from 5.6 to 8.5  $\mu\text{m}$ ). The spectral width is only limited by the operational range of used QCL. This large operation of the device is due to the low dispersion of the material [154] and of the waveguide in this wavelength range. As it can be observed in [Fig.2.1.3](#), the guided mode effective index variation is very low. Furthermore, benefiting from the large operation range of the waveguide, with a proper designed MMI, such large operational interferometer is achieved. It is worth to note that the device shows large operation over  $800 \text{ cm}^{-1}$ , but the spectroscopic bandwidth which is defined by the device FSR is less than this operation range.

Generally, the measured interferogram may be distorted by unintentional phase shifts, caused by fabrication errors. This typically results in a misalignment of the output spectrum of the MZIs. Interestingly, the reported interferogram of the SHFTS shows good alignment without any additional phase error correction in the data processing. In the interferogram, the Littrow wavenumber dedicated in red lines in [Fig.5.2.4](#), where all MZIs reach maximum transmittance can be clearly observed for wavenumbers of 1185, 1450 and 1715  $\text{cm}^{-1}$  in TE polarization (with only a few  $\text{cm}^{-1}$  difference in TM polarization). This is a clear evidence of low phase distortion, proving the robustness of the Ge-rich  $\text{Si}_{1-x}\text{Ge}_x$  FTS to fabrication imperfections. Then, the device FSR can be calculated as it is the half of the spectral interval between two Littrow wavenumbers. A value of  $132.5 \text{ cm}^{-1}$  is obtained. It shows very good agreement with the theoretical calculation by Eq. (28).

To confirm the performance of the fabricated SHFTS, the experiment of signal retrieval has been done along the full operational wavelength range. [Fig.5.2.5](#) presents experimentally retrieved spectra for different input signals scanned inside the operating wavelength range, and for both TE and TM polarizations. Note that at each input wavelength, a retrieval spectral window narrower than FSR has been considered. A Gaussian apodization function is applied in the spectral domain to reduce truncation ripples [143]. The spectral resolution of the spectrometer, which is then measured as the full width at half maximum of the retrieved signals, is equal to  $12 \text{ cm}^{-1}$  and  $14.5 \text{ cm}^{-1}$  for TE and TM polarizations,

respectively ([Fig.5.2.5\(b,d\)](#)). The retrieval experiment validates that our SHFTS can be performed either in TE or TM polarization. Furthermore, considering the low birefringence of the  $\text{Si}_{1-x}\text{Ge}_x$  MIR waveguide it can be potentially extended to polarization independent operation which is highly desirable for applications such as satellite instrumentation and unmanned aerial vehicles.

### 5.3. Conclusion

In this chapter, a spatial heterodyne Fourier Transform spectrometer working both in TE and TM polarization based on the Ge-rich graded-index  $\text{Si}_{1-x}\text{Ge}_x$  waveguide has been presented. An unprecedented broadband operation over  $800\text{ cm}^{-1}$  range has been demonstrated for a wavelength from 5 to  $8.5\ \mu\text{m}$  covering part of the molecular fingerprint region. The reported spectrometer shows an experimentally spectral bandwidth of  $132.5\text{ cm}^{-1}$  and a spectral resolution of less than  $15\text{ cm}^{-1}$  for both polarizations. Interestingly, low phase errors have been demonstrated, indicating a good robustness of the device design and fabrication against fluctuations of the waveguide effective index and optical path. It is also possible to further increase the spectral resolution by applying compressive-sensing technique [155] or the combination with digital FTS approach [148]. In another hand, the device spectral bandwidth can be enlarged by either integrating more MZIs at the expense of large footprint, or with a combination of temperature-introduced interference variation [156].

## 6. Conclusions and Future Directions

### 6.1.1. Conclusions

The work presented in this manuscript aims to study the optical property of graded-index  $\text{Si}_{1-x}\text{Ge}_x$  waveguides in the MIR and to develop integrated devices with a perspective of demonstrating monolithically integrated spectroscopic system for mid-infrared sensing applications.

To achieve the objective, I studied different optical devices as building blocks for the final monolithically integrated circuits. To do so, I did extensive hands-on design, cleanroom fabrication and experimental investigations of several devices, such as MIR broadband waveguides, grating couplers, Bragg grating filters, Bragg grating reflector cavities, racetrack resonators and integrated Fourier-transform spectrometer. The graded-index  $\text{Si}_{1-x}\text{Ge}_x$  materials were grown using the LEPECVD on a 100 mm Si (001) substrate by our collaborator group at L-NESS laboratory, Politecnico di Milano, Italy. The device fabrication was developed and performed at the in-house 1000 m<sup>2</sup> cleanroom at C2N site Orsay, Université Paris-Sud. The fabrication flow is described in the [section 2.2](#). Then as introduced in the [section 3.2.2](#), by collaborating with the cleanroom engineer Xavier Leroux, I optimized the fabrication process which allow us to fabricate properly more complicate devices. For the devices characterization, a new free-space configuration experimental set-up, which is developed by the post-doctor Joan Manel Ramirez, is presented in the [section 2.3.1](#).

In the first part of this thesis, the optical property of graded-index  $\text{Si}_{1-x}\text{Ge}_x$  waveguides have been evaluated in a broadband MIR wavelength range. The propagation losses have been studied for waveguides based on three platforms with different index profiles obtained by varying the Ge concentration during material growth. Waveguide propagation loss of less than 3 dB/cm has been obtained for the whole tested wavelength range from 5.5  $\mu\text{m}$  to 8.5  $\mu\text{m}$  for the waveguide based on the platform A and B (as the index profile shown in [Fig.2.1.1](#)). A propagation loss as high as 10 dB/cm was obtained for waveguides based on the platform C in which the guided mode shows higher overlap factor with the bottom Si

substrate. Then, the MIR sensing capability using evanescent field absorption has been theoretically evaluated. A proof of concept experiment shows the feasibility of the graded-index  $\text{Si}_{1-x}\text{Ge}_x$  waveguides for MIR sensing applications as described in [section 2.4](#).

Then, starting from the low-loss broadband MIR waveguides, I designed firstly grating couplers at  $7.5\ \mu\text{m}$  for both TE and TM polarizations. As shown in the [section 3.1](#), the grating couplers show a very large operation bandwidth at the interested wavelength. Thanks to the low material dispersion and the self-mode-adaptation effect of the  $\text{Si}_{1-x}\text{Ge}_x$  waveguide, a -1-dB bandwidth as high as 300 nm is obtained for both polarizations. In a meanwhile, the periodic waveguides operating as Bragg grating filter are implemented on the  $\text{Si}_{1-x}\text{Ge}_x$  waveguides as shown in the [section 3.2](#). Based on the  $6\text{-}\mu\text{m}$ -thick platform, benefiting from the low-loss broadband waveguide, the Bragg gratings have been successfully demonstrated on the  $\text{Si}_{1-x}\text{Ge}_x$  waveguides in a wide wavelength range from  $5.4$  to  $8.4\ \mu\text{m}$ . As the experimental results shown in [section 3.2.3](#), the power rejection as high as 21.6 dB is obtained at  $6.4\ \mu\text{m}$ .

Moreover, in the purpose of enhancing the light-matter interaction in the MIR fingerprint region, MIR integrated resonant structures have been demonstrated at a wavelength of  $8\ \mu\text{m}$ . Two approaches have been studied, based on Fabry-Perot cavity using waveguide Bragg grating as reflecting mirror and on racetrack resonators. A loaded quality-factor as high as 2200 is measured for a cavity using waveguide Bragg grating with 500 grating periods on top corrugations. Then, in order to ease the device fabrication, the Fabry-Perot cavities using lateral-corrugated waveguide Bragg grating have been successfully fabricated. Although, the SEM images confirm the good quality of fabrication, however, the preliminary results for this lateral-corrugated device show not evident resonance at the interested wavelength. Later, the demonstration of racetrack resonators with a Q-factor as high as 3200 is presented in [section 4.2](#).

Finally, as one of the key components for the monolithically integrated spectroscopic system, the on-chip integrated Fourier-transform spectrometer has been experimentally investigated on the  $\text{Si}_{1-x}\text{Ge}_x$  platform, based on an array of asymmetric MZIs with different path delay linearly increasing from 0 to a maximum  $178.6\ \mu\text{m}$ . The FT spectrometer integrated on  $\text{Si}_{1-x}\text{Ge}_x$  waveguide shows an unprecedented broadband dual-polarization operation in an

800  $\text{cm}^{-1}$  range from 5 to 8.5  $\mu\text{m}$  which is limited by the bandwidth of the used tunable laser. Using the Moore-Penrose method, the input monochromatic signal has been reconstructed in the operational range, noting that the retrieval window is always narrower than the device FSR. The device FSR is measured as 132.5  $\text{cm}^{-1}$  with a spectral resolution of 12  $\text{cm}^{-1}$  (14.5  $\text{cm}^{-1}$ ) for TE (TM) polarization.

### 6.1.2. Future Directions

Regarding the future works, we can note that the QCL used in the experimental set-up was recently extended up to 11  $\mu\text{m}$ . New characterizations are planned to investigate propagation loss and device properties in the new accessible wavelength range from 8.5  $\mu\text{m}$  to 11  $\mu\text{m}$ .

Secondly, as the free-space configuration measurement requires notorious realignment, it is possible to update the set-up for surface light coupling using the grating couplers to ease the device characterization. In the meanwhile, the performance of designed grating couplers can be experimentally confirmed.

Then, as the linewidth of the used laser may limit the measurement of Q-factor of the resonators as described in chapter 4, further experiments using a continuous (DC) operation MIR source with narrower spectral width, or using different technique based on cavity-ring down spectroscopy for example should be performed to estimate the ultimate performance of the resonant structures. Although the sample of Fabry-Perot cavity using lateral-corrugated Bragg gratings has been properly fabricated, the preliminary measurements show not evident resonance at the interested wavelength. Further investigation of the Fabry-Perot cavity using lateral-corrugated Bragg gratings needs to be done to understand the structure and to confirm the performance of the cavity. Besides the Fabry-Perot cavity, the characterization of 2<sup>nd</sup> generation racetrack resonators allow us to study the influence of the gap distance on the resonator performances.

Finally, a systematically study of the bending losses of the waveguide can contribute in one hand to increase the FSR of the integrated MIR resonator. In another hand, with a reduced bending radius, the footprint of the integrated FT spectrometer can be reduced, or more MZIs can be integrated within a same device footprint providing a better spectral

resolution. Regarding the properties of on-chip FTS, the technique of digital FTS can further increase the spectral resolution in a limited device footprint [148]. Then, the device FSR can be increased by combining the spatial interferogram with temperature introduced phase change on the MZIs [156].

Furthermore, based on all the demonstrated devices, it is possible to integrate different building blocks together. As an example a sensing element using a ring resonator can be conceived, for example at 7.7  $\mu\text{m}$  for the detection of methane. With the variation of Q-factor and the spectral transmittance of the resonator at this wavelength, the concentration of methane in the environment can be detected. It should be interesting to experimentally evaluate the detection limit of such integrated system.

In terms of integrated light source, benefiting from the high 3<sup>rd</sup> order nonlinear coefficient of material and the previously reported study on the anomalous dispersion of  $\text{Si}_{1-x}\text{Ge}_x$  waveguides [157], supercontinuum based on  $\text{Si}_{1-x}\text{Ge}_x$  waveguides or frequency comb generation based on the MIR resonators in the LWIR wavelength range covering the wide fingerprint region have to be investigated in the near future.

## References

1. F. Namavar, E. Cortesi, R. A. Soref, and P. Sioshansi, "On the Formation of Thick and Multiple Layer Simox Structures and their Applications," *MRS Proc.* **147**, 241 (1989).
2. E. Cortesi, F. Namavar, and R. A. Soref, "Novel silicon-on-insulator structures for silicon waveguides," in *IEEE SOS/SOI Technology Conference* (IEEE, n.d.), p. 109.
3. R. A. Soref and B. R. Bennett, "Kramers-Kronig Analysis Of Electro-Optical Switching In Silicon," in M. A. Mentzer and S. Sriram, eds. (International Society for Optics and Photonics, 1987), **0704**, p. 32.
4. G. Proll, "R. Narayanaswamy, O.S. Wolfbeis (eds.): Optical Sensors: Industrial, Environmental and Diagnostic Applications," *Anal. Bioanal. Chem.* **381**(1), 18–19 (2005).
5. W. Zhang, S. Serna, X. Le Roux, L. Vivien, and E. Cassan, "Highly sensitive refractive index sensing by fast detuning the critical coupling condition of slot waveguide ring resonators," *Opt. Lett.* **41**(3), 532 (2016).
6. J. Villatoro and D. Monzón-Hernández, "Low-Cost Optical Fiber Refractive-Index Sensor Based on Core Diameter Mismatch," *J. Light. Technol.* Vol. 24, Issue 3, pp. 1409- **24**(3), 1409 (2006).
7. M. V. Hernandez-Arriaga, M. A. Bello-Jimenez, A. Rodriguez-Cobos, R. Lopez-Estopier, and M. V. Andres, "High Sensitivity Refractive Index Sensor Based on Highly Overcoupled Tapered Fiber-Optic Couplers," *IEEE Sens. J.* **17**(2), 333–339 (2017).
8. V. Singh, P. T. Lin, N. Patel, H. Lin, L. Li, Y. Zou, F. Deng, C. Ni, J. Hu, J. Giammarco, A. P. Soliani, B. Zdyrko, I. Luzinov, S. Novak, J. Novak, P. Wachtel, S. Danto, J. D. Musgraves, K. Richardson, L. C. Kimerling, and A. M. Agarwal, "Mid-infrared materials and devices on a Si platform for optical sensing," *Sci. Technol. Adv. Mater.* **15**(1), 014603 (2014).
9. T. Jin, L. Li, B. Zhang, H. Y. G. Lin, H. Wang, and P. T. Lin, "Real-Time and Label-Free Chemical Sensor-on-a-chip using Monolithic Si-on-BaTiO<sub>3</sub>Mid-Infrared waveguides," *Sci. Rep.* **7**(1), 1–8 (2017).
10. W. Li, P. Anantha, K. H. Lee, H. D. Qiu, X. Guo, S. C. K. Goh, L. Zhang, H. Wang, R. A. Soref, and C. S. Tan, "Spiral Waveguides on Germanium-on-Silicon Nitride Platform for Mid-IR Sensing Applications," *IEEE Photonics J.* **10**(3), 1–7 (2018).
11. A. Gutierrez-Arroyo, E. Baudet, L. Bodiou, V. Nazabal, E. Rinnert, K. Michel, B. Bureau, F. Colas, and J. Charrier, "Theoretical study of an evanescent optical integrated sensor for multipurpose detection of gases and liquids in the Mid-Infrared," *Sensors Actuators B Chem.* **242**, 842–848 (2017).
12. A. Gutierrez-Arroyo, E. Baudet, L. Bodiou, J. Lemaitre, I. Hardy, F. Faijan, B. Bureau, V. Nazabal, and J. Charrier, "Optical characterization at 77  $\mu\text{m}$  of an integrated platform based on chalcogenide waveguides for sensing applications in the mid-infrared," *Opt. Express* **24**(20), 23109 (2016).
13. S. Zheng, J. C.-H. Lin, H. L. Kasdan, and Y.-C. Tai, "Fluorescent labeling, sensing, and differentiation of leukocytes from undiluted whole blood samples," *Sensors*

- Actuators B Chem. **132**(2), 558–567 (2008).
14. Y.-T. Yan, J. Liu, G.-P. Yang, F. Zhang, Y.-K. Fan, W.-Y. Zhang, and Y.-Y. Wang, "Highly selective luminescence sensing for the detection of nitrobenzene and Fe<sup>3+</sup> by new Cd(II)-based MOFs," *CrystEngComm* **20**(4), 477–486 (2018).
  15. A. Douvali, A. C. Tsipis, S. V. Eliseeva, S. Petoud, G. S. Papaefstathiou, C. D. Malliakas, I. Papadas, G. S. Armatas, I. Margiolaki, M. G. Kanatzidis, T. Lazarides, and M. J. Manos, "Turn-On Luminescence Sensing and Real-Time Detection of Traces of Water in Organic Solvents by a Flexible Metal-Organic Framework," *Angew. Chemie Int. Ed.* **54**(5), 1651–1656 (2015).
  16. J. Tschmelak, G. Proll, and G. Gauglitz, "Optical biosensor for pharmaceuticals, antibiotics, hormones, endocrine disrupting chemicals and pesticides in water: Assay optimization process for estrone as example," *Talanta* **65**(2), 313–323 (2005).
  17. L. Zeng, E. W. Miller, A. Pralle, E. Y. Isacoff, and C. J. Chang, "A Selective Turn-On Fluorescent Sensor for Imaging Copper in Living Cells," *J. Am. Chem. Soc.* **128**(1), 10–11 (2006).
  18. R. A. Soref and J. P. Lorenzo, "Single-crystal silicon: a new material for 1.3 and 1.6  $\mu\text{m}$  integrated-optical components," *Electron. Lett.* **21**(21), 953 (1985).
  19. L. Jin, M. Li, and J.-J. He, "Optical waveguide double-ring sensor using intensity interrogation with a low-cost broadband source," *Opt. Lett.* **36**(7), 1128 (2011).
  20. A. S. Jugessur, J. Dou, J. S. Aitchison, R. M. De La Rue, and M. Gnan, "A photonic nano-Bragg grating device integrated with microfluidic channels for bio-sensing applications," *Microelectron. Eng.* **86**(4–6), 1488–1490 (2009).
  21. P. Prabhathan, V. M. Murukeshan, Z. Jing, and P. V. Ramana, "Compact SOI nanowire refractive index sensor using phase shifted Bragg grating," *Opt. Express* **17**(17), 15330 (2009).
  22. L. Huang, H. Yan, X. Xu, S. Chakravarty, N. Tang, H. Tian, and R. T. Chen, "Improving the detection limit for on-chip photonic sensors based on subwavelength grating racetrack resonators," *Opt. Express* **25**(9), 10527 (2017).
  23. "Quantum Cascade Laser Technology (QCLs)," <https://www.daylightsolutions.com/home/technology/about-mid-ir-quantum-cascade-lasers/>.
  24. R. Soref, "Mid-infrared photonics in silicon and germanium," *Nat. Photonics* **4**(8), 495–497 (2010).
  25. M. Nedeljkovic, A. Z. Khokhar, Y. Hu, X. Chen, J. S. Penades, S. Stankovic, H. M. H. Chong, D. J. Thomson, F. Y. Gardes, G. T. Reed, and G. Z. Mashanovich, "Silicon photonic devices and platforms for the mid-infrared," *Opt. Mater. Express* **3**(9), 1205 (2013).
  26. G. Z. Mashanovich, M. Nedeljkovic, J. Soler-Penades, Z. Qu, W. Cao, A. Osman, Y. Wu, C. J. Stirling, Y. Qi, Y. X. Cheng, L. Reid, C. G. Littlejohns, J. Kang, Z. Zhao, M. Takenaka, T. Li, Z. Zhou, F. Y. Gardes, D. J. Thomson, and G. T. Reed, "Group IV mid-infrared photonics [Invited]," *Opt. Mater. Express* **8**(8), 2276 (2018).
  27. H. Lin, Z. Luo, T. Gu, L. C. Kimerling, K. Wada, A. Agarwal, and J. Hu, "Mid-infrared integrated photonics on silicon: a perspective," *Nanophotonics* **7**(2), 393–420 (2017).
  28. L. Zhang, A. M. Agarwal, L. C. Kimerling, and J. Michel, "Nonlinear Group IV photonics based on silicon and germanium: From near-infrared to mid-infrared,"

- Nanophotonics **3**(4–5), 247–268 (2014).
29. Y. Zou, S. Chakravarty, C.-J. Chung, X. Xu, and R. T. Chen, "Mid-infrared silicon photonic waveguides and devices [Invited]," *Photonics Res.* **6**(4), 254 (2018).
  30. R. Shankar and M. Lončar, "Silicon photonic devices for mid-infrared applications," *Nanophotonics* **3**(4–5), 329–341 (2014).
  31. D. Marris-Morini, V. Vakarín, J. Manel Ramirez, Q. Liu, A. Ballabio, J. Frigerio, M. Montesinos, C. Alonso-Ramos, X. Le Roux, S. Serna, D. Benedikovic, D. Chrastina, L. Vivien, and G. Isella, "Germanium-based integrated photonics from near-to mid-infrared applications," *Nanophotonics* **7**(11), 1781–1793 (2018).
  32. H. Nguyen-Van, A. N. Baranov, Z. Loghmari, L. Cerutti, J.-B. Rodriguez, J. Tournet, G. Narcy, G. Boissier, G. Patriarche, M. Bahriz, E. Tournié and R. Teissier, "Quantum cascade lasers grown on silicon," *Sci. Rep.* **8**(1), 7206 (2018).
  33. G. Z. Mashanovich, M. M. Milošević, M. Nedeljkovic, N. Owens, B. Xiong, E. J. Teo, and Y. Hu, "Low loss silicon waveguides for the mid-infrared," *Opt. Express* **19**(8), 7112 (2011).
  34. N. Hattasan, B. Kuyken, F. Leo, E. M. P. Ryckeboer, D. Vermeulen, and G. Roelkens, "High-Efficiency SOI Fiber-to-Chip Grating Couplers and Low-Loss Waveguides for the Short-Wave Infrared," *IEEE Photonics Technol. Lett.* **24**(17), 1536–1538 (2012).
  35. M. Nedeljkovic, A. V. Velasco, A. Z. Khokhar, A. Delage, P. Cheben, and G. Z. Mashanovich, "Mid-Infrared Silicon-on-Insulator Fourier-Transform Spectrometer Chip," *IEEE Photonics Technol. Lett.* **28**(4), 528–531 (2016).
  36. S. A. Miller, M. Yu, X. Ji, A. G. Griffith, J. Cardenas, A. L. Gaeta, and M. Lipson, "Low-loss silicon platform for broadband mid-infrared photonics," *Optica* **4**(7), 707 (2017).
  37. J. S. Penadés, A. Sánchez-Postigo, M. Nedeljkovic, A. Ortega-Moñux, J. G. Wang, J. M. M. Pérez, Y. Xu, R. Halir, Z. Qu, A. Z. Khokhar, A. Osman, W. Cao, C. G. Littlejohns, P. Cheben, I. Molina-Fernández, and G. Z. Mashanovich, "Suspended silicon waveguides for long-wave infrared wavelengths," *Opt. Lett.* **43**(4), 795 (2018).
  38. Thomoas R. Harris, "Optical Properties of Si, Ge, GaAs, GaSb, InAs, and InP at Elevated Temperatures," Air University (2010).
  39. M. Sieger, F. Balluff, X. Wang, S.-S. Kim, L. Leidner, G. Gauglitz, and B. Mizaikoff, "On-Chip Integrated Mid-Infrared GaAs/AlGaAs Mach–Zehnder Interferometer," *Anal. Chem.* **85**(6), 3050–3052 (2013).
  40. H. Lin, L. Li, Y. Zou, S. Danto, J. D. Musgraves, K. Richardson, S. Kozacik, M. Murakowski, D. Prather, P. T. Lin, V. Singh, A. Agarwal, L. C. Kimerling, and J. Hu, "Demonstration of high-Q mid-infrared chalcogenide glass-on-silicon resonators," *Opt. Lett.* **38**(9), 1470 (2013).
  41. Y. Yu, X. Gai, P. Ma, K. Vu, Z. Yang, R. Wang, D.-Y. Choi, S. Madden, and B. Luther-Davies, "Experimental demonstration of linearly polarized 2–10  $\mu\text{m}$  supercontinuum generation in a chalcogenide rib waveguide," *Opt. Lett.* **41**(5), 958 (2016).
  42. F. Li, S. D. Jackson, C. Grillet, E. Magi, D. Hudson, S. J. Madden, Y. Moghe, C. O'Brien, A. Read, S. G. Duvall, P. Atanackovic, B. J. Eggleton, and D. J. Moss, "Low propagation loss silicon-on-sapphire waveguides for the mid-infrared," *Opt. Express* **19**(16), 15212 (2011).
  43. Y. Zou, H. Subbaraman, S. Chakravarty, X. Xu, A. Hosseini, W.-C. Lai, P. Wray, and R. T. Chen, "Grating-coupled silicon-on-sapphire integrated slot waveguides

- operating at mid-infrared wavelengths," *Opt. Lett.* **39**(10), 3070 (2014).
44. N. Singh, D. D. Hudson, and B. J. Eggleton, "Silicon-on-sapphire pillar waveguides for Mid-IR supercontinuum generation," *Opt. Express* **23**(13), 17345 (2015).
  45. R. Shankar, I. Bulu, and M. Lončar, "Integrated high-quality factor silicon-on-sapphire ring resonators for the mid-infrared," *Appl. Phys. Lett.* **102**(5), 051108 (2013).
  46. S. Khan, J. Chiles, J. Ma, and S. Fathpour, "Silicon-on-nitride waveguides for mid- and near-infrared integrated photonics," *Appl. Phys. Lett.* **102**(12), 121104 (2013).
  47. A. Spott, J. Peters, M. L. Davenport, E. J. Stanton, C. D. Merritt, W. W. Bewley, I. Vurgaftman, C. S. Kim, J. R. Meyer, J. Kirch, L. J. Mawst, D. Botez, and J. E. Bowers, "Quantum cascade laser on silicon," *Optica* **3**(5), 545 (2016).
  48. A. Spott, J. Peters, M. Davenport, E. Stanton, C. Zhang, C. Merritt, W. Bewley, I. Vurgaftman, C. Kim, J. Meyer, J. Kirch, L. Mawst, D. Botez, J. Bowers, A. Spott, J. Peters, M. L. Davenport, E. J. Stanton, C. Zhang, C. D. Merritt, W. W. Bewley, I. Vurgaftman, C. S. Kim, J. R. Meyer, J. Kirch, L. J. Mawst, D. Botez, and J. E. Bowers, "Heterogeneously Integrated Distributed Feedback Quantum Cascade Lasers on Silicon," *Photonics* **3**(2), 35 (2016).
  49. K. Luke, Y. Okawachi, M. R. E. Lamont, A. L. Gaeta, and M. Lipson, "Broadband mid-infrared frequency comb generation in a Si<sub>3</sub>N<sub>4</sub> microresonator," *Opt. Lett.* **40**(21), 4823 (2015).
  50. N. K. Hon, R. Soref, and B. Jalali, "The third-order nonlinear optical coefficients of Si, Ge, and Si<sub>1-x</sub>Ge<sub>x</sub> in the midwave and longwave infrared," *J. Appl. Phys.* **110**(1), 011301 (2011).
  51. Y.-C. Chang, V. Paeder, L. Hvozdar, J.-M. Hartmann, and H. P. Herzig, "Low-loss germanium strip waveguides on silicon for the mid-infrared," *Opt. Lett.* **37**(14), 2883 (2012).
  52. A. Malik, S. Dwivedi, L. Van Landschoot, M. Muneeb, Y. Shimura, G. Lepage, J. Van Campenhout, W. Vanherle, T. Van Opstal, R. Loo, and G. Roelkens, "Ge-on-Si and Ge-on-SOI thermo-optic phase shifters for the mid-infrared," *Opt. Express* **22**(23), 28479 (2014).
  53. S. Radosavljevic, N. T. Beneitez, A. Katumba, M. Muneeb, M. Vanslebrouck, B. Kuyken, and G. Roelkens, "Mid-infrared Vernier racetrack resonator tunable filter implemented on a germanium on SOI waveguide platform [Invited]," *Opt. Mater. Express* **8**(4), 824 (2018).
  54. T.-H. Xiao, Z. Zhao, W. Zhou, M. Takenaka, H. K. Tsang, Z. Cheng, and K. Goda, "High-Q germanium optical nanocavity," *Photonics Res.* **6**(9), 925 (2018).
  55. T.-H. Xiao, Z. Zhao, W. Zhou, C.-Y. Chang, S. Y. Set, M. Takenaka, H. K. Tsang, Z. Cheng, and K. Goda, "Mid-infrared high-Q germanium microring resonator," *Opt. Lett.* **43**(12), 2885 (2018).
  56. C. Grillet, P. Ma, B. Luther-Davies, D. Hudson, C. Monat, S. Madden, D. J. Moss, M. Brun, P. Labeye, S. Ortiz, and S. Nicoletti, "Low loss SiGe waveguides in the MID-IR," in *2013 Conference on Lasers & Electro-Optics Europe & International Quantum Electronics Conference CLEO EUROPE/IQEC* (IEEE, 2013), pp. 1–1.
  57. M. Brun, P. Labeye, G. Grand, J.-M. Hartmann, F. Boulila, M. Carras, and S. Nicoletti, "Low loss SiGe graded index waveguides for mid-IR applications," *Opt. Express* **22**(1), 508 (2014).

58. P. Barritault, M. Brun, P. Labeye, J.-M. Hartmann, F. Boulila, M. Carras, and S. Nicoletti, "Design, fabrication and characterization of an AWG at 45  $\mu\text{m}$ ," *Opt. Express* **23**(20), 26168 (2015).
59. A. Koshkinbayeva, P. Barritault, S. Ortiz, S. Boutami, M. Brun, J.-M. Hartmann, P. Brianceau, O. Lartigue, F. Boulila, R. Orobtschouk, and P. Labeye, "Impact of Non-Central Input in  $N \times M$  Mid-IR Arrayed Waveguide Gratings Integrated on Si," *IEEE Photonics Technol. Lett.* **28**(20), 2191–2194 (2016).
60. V. Vakarin, P. Chaisakul, J. Frigerio, A. Ballabio, X. Le Roux, J.-R. Coudeville, D. Bouville, D. Perez-Galacho, L. Vivien, G. Isella, and D. Marris-Morini, "Sharp bends and Mach-Zehnder interferometer based on Ge-rich-SiGe waveguides on SiGe graded buffer," *Opt. Express* **23**(24), 30821 (2015).
61. P. Chaisakul, D. Marris-Morini, J. Frigerio, D. Chrastina, M.-S. Rouified, S. Cecchi, P. Crozat, G. Isella, and L. Vivien, "Integrated germanium optical interconnects on silicon substrates," *Nat. Photonics* **8**(6), 482–488 (2014).
62. P. Chaisakul, D. Marris-Morini, G. Isella, D. Chrastina, X. Le Roux, E. Gatti, S. Edmond, J. Osmond, E. Cassan, and L. Vivien, "Quantum-confined Stark effect measurements in Ge/SiGe quantum-well structures," *Opt. Lett.* **35**(17), 2913 (2010).
63. P. Chaisakul, D. Marris-Morini, M.-S. Rouified, G. Isella, D. Chrastina, J. Frigerio, X. Le Roux, S. Edmond, J.-R. Coudeville, and L. Vivien, "23 GHz Ge/SiGe multiple quantum well electro-absorption modulator," *Opt. Express* **20**(3), 3219 (2012).
64. J. M. Ramirez, V. Vakarin, C. Gilles, J. Frigerio, A. Ballabio, P. Chaisakul, X. Le Roux, C. Alonso-Ramos, G. Maisons, L. Vivien, M. Carras, G. Isella, and D. Marris-Morini, "Low-loss Ge-rich Si<sub>0.2</sub>Ge<sub>0.8</sub> waveguides for mid-infrared photonics," *Opt. Lett.* **42**(1), 105 (2017).
65. Lumerical, "FDE," [https://kb.lumerical.com/solvers\\_finite\\_difference\\_eigenmode.html](https://kb.lumerical.com/solvers_finite_difference_eigenmode.html).
66. G. Isella, D. Chrastina, B. Rössner, T. Hackbarth, H. J. Herzog, U. König, and H. Von Känel, "Low-energy plasma-enhanced chemical vapor deposition for strained Si and Ge heterostructures and devices," *Solid. State. Electron.* **48**(8), 1317–1323 (2004).
67. "MIRcat-QT™ Mid-IR Laser: Tune 1000 cm<sup>-1</sup> at 1000s cm<sup>-1</sup>/s | High-Speed Tuning," <https://www.daylightsolutions.com/product/mircat/>.
68. J. M. Ramirez, Q. Liu, V. Vakarin, J. Frigerio, A. Ballabio, X. Le Roux, D. Bouville, L. Vivien, G. Isella, and D. Marris-Morini, "Graded SiGe waveguides with broadband low-loss propagation in the mid infrared," *Opt. Express* **26**(2), 870 (2018).
69. L. Tombez, E. J. Zhang, J. S. Orcutt, S. Kamlapurkar, and W. M. J. Green, "Methane absorption spectroscopy on a silicon photonic chip," *Optica* **4**(11), 1322 (2017).
70. S. Prasad, L. Zhao, and J. Gomes, "Methane and Natural Gas Exposure Limits," *Epidemiology* **22**, S251 (2011).
71. "MICROPOSITM S1818TM POSITIVE PHOTORESIST," [http://microchem.com/products/images/uploads/S1800\\_Photoresist.pdf](http://microchem.com/products/images/uploads/S1800_Photoresist.pdf).
72. "The Spectra of Molecules: Infrared - Chemistry LibreTexts," [https://chem.libretexts.org/Bookshelves/General\\_Chemistry/Book%3A\\_ChemPRIME\\_\(Moore\\_et\\_al.\)/21Spectra\\_and\\_Structure\\_of\\_Atoms\\_and\\_Molecules/21.04%3A\\_The\\_Spectra\\_of\\_Molecules%3A\\_Infrared](https://chem.libretexts.org/Bookshelves/General_Chemistry/Book%3A_ChemPRIME_(Moore_et_al.)/21Spectra_and_Structure_of_Atoms_and_Molecules/21.04%3A_The_Spectra_of_Molecules%3A_Infrared).
73. M. J. Jafari, "Application of Vibrational Spectroscopy in Organic Electronics," Linköping University (2017).

74. Q. Liu, J. M. Ramirez, V. Vakarin, X. Le Roux, A. Ballabio, J. Frigerio, D. Chrastina, G. Isella, D. Bouville, L. Vivien, C. A. Ramos, and D. Marris-Morini, "Mid-infrared sensing between 52 and 66  $\mu\text{m}$  wavelengths using Ge-rich SiGe waveguides [Invited]," *Opt. Mater. Express* **8**(5), 1305 (2018).
75. D. Taillaert, F. Van Laere, M. Ayre, W. Bogaerts, D. Van Thourhout, P. Bienstman, and R. Baets, "Grating Couplers for Coupling between Optical Fibers and Nanophotonic Waveguides," *Jpn. J. Appl. Phys.* **45**(8A), 6071–6077 (2006).
76. R. Bruck and R. Hainberger, "Efficiency enhancement of grating couplers for single mode polymer waveguides through high index coatings," 201–204 (2008).
77. Xia Chen and H. K. Tsang, "Nanoholes Grating Couplers for Coupling Between Silicon-on-Insulator Waveguides and Optical Fibers," *IEEE Photonics J.* **1**(3), 184–190 (2009).
78. P. Cheben, J. H. Schmid, and D. Xu, "Fiber-chip grating coupler based on interleaved trenches with directionality exceeding 95 %," **39**(18), 5351–5354 (2014).
79. S. Radosavljevic, B. Kuyken, and G. Roelkens, "Efficient 52  $\mu\text{m}$  wavelength fiber-to-chip grating couplers for the Ge-on-Si and Ge-on-SOI mid-infrared waveguide platform," *Opt. Express* **25**(16), 19034 (2017).
80. X. Wang, J. Flueckiger, S. Schmidt, S. Grist, S. T. Fard, J. Kirk, M. Doerfler, K. C. Cheung, D. M. Ratner, and L. Chrostowski, "A silicon photonic biosensor using phase-shifted Bragg gratings in slot waveguide," *J. Biophotonics* **6**(10), n/a-n/a (2013).
81. W. Zhang and J. Yao, "A fully reconfigurable waveguide Bragg grating for programmable photonic signal processing," *Nat. Commun.* **9**(1), 1396 (2018).
82. E. H. Bernhardt, Q. Lu, H. A. G. M. van Wolferen, K. Wörhoff, R. M. de Ridder, and M. Pollnau, "Monolithic distributed Bragg reflector cavities in Al<sub>2</sub>O<sub>3</sub> with quality factors exceeding 10<sup>6</sup>," *Photonics Nanostructures - Fundam. Appl.* **9**(3), 225–234 (2011).
83. R. Halir, P. J. Bock, P. Cheben, A. Ortega-Moñux, C. Alonso-Ramos, J. H. Schmid, J. Lapointe, D.-X. Xu, J. G. Wang üemert-P érez, Í Molina-Fern ández, and S. Janz, "Waveguide sub-wavelength structures: a review of principles and applications," *Laser Photon. Rev.* **9**(1), 25–49 (2015).
84. R. K. Nubling and J. A. Harrington, "Single-Crystal Laser-Heated Pedestal-Growth Sapphire Fibers for Er:YAG Laser Power Delivery.," *Appl. Opt.* **37**(21), 4777–81 (1998).
85. H. Ebendorff-Heidepriem, T.-C. Foo, R. C. Moore, W. Zhang, Y. Li, T. M. Monroe, A. Hemming, and D. G. Lancaster, "Fluoride glass microstructured optical fiber with large mode area and mid-infrared transmission," *Opt. Lett.* **33**(23), 2861 (2008).
86. I. Savelli, O. Mouawad, J. Fatome, B. Kibler, F. D é s é v é lavy, G. Gadret, J.-C. Jules, P.-Y. Bony, H. Kawashima, W. Gao, T. Kohoutek, T. Suzuki, Y. Ohishi, and F. Smektala, "Mid-infrared 2000-nm bandwidth supercontinuum generation in suspended-core microstructured Sulfide and Tellurite optical fibers," *Opt. Express* **20**(24), 27083 (2012).
87. M. Michalska, J. Mikolajczyk, J. Wojtas, and J. Swiderski, "Mid-infrared, super-flat, supercontinuum generation covering the 2–5  $\mu\text{m}$  spectral band using a fluoroindate fibre pumped with picosecond pulses," *Sci. Rep.* **6**(1), 39138 (2016).
88. C. Markos, J. C. Travers, A. Abdolvand, B. J. Eggleton, and O. Bang, "Hybrid

- photonic-crystal fiber," *Rev. Mod. Phys.* **89**(4), 045003 (2017).
89. Seleoptics, "Wide bandwidth single mode Mid Infraed Fibers," [https://docs.wixstatic.com/ugd/541e1d\\_7129c860dab6400cb1ea9b8ce0281687.pdf](https://docs.wixstatic.com/ugd/541e1d_7129c860dab6400cb1ea9b8ce0281687.pdf).
  90. C. Alonso-Ramos, A. O. Moñux, L. Zavargo-Peche, R. Halir, J. de Oliva-Rubio, I. Molina-Fernández, P. Cheben, D. X. Xu, S. Janz, N. Kim, and B. Lamontagne, "Single-etch grating coupler for micrometric silicon rib waveguides," **36**(14), 2647–2649 (2011).
  91. M. Fan, M. A. Popovi, and F. X. Kärtner, "High Directivity , Vertical Fiber-to-Chip Coupler with Anisotropically Radiating Grating Teeth," 9–10 (n.d.).
  92. R. Halir, P. Cheben, J. H. Schmid, R. Ma, D. Bedard, S. Janz, D.-X. Xu, A. Densmore, J. Lapointe, and Í Molina-Fernández, "Continuously apodized fiber-to-chip surface grating coupler with refractive index engineered subwavelength structure," *Opt. Lett.* **35**(19), 3243 (2010).
  93. H. Sohlström, K. B. Gylfason, and M. Antelius, "An apodized SOI waveguide-to-fiber surface grating coupler for single lithography silicon photonics," *Opt. Express*, Vol. 19, Issue 4, pp. 3592-3598 **19**(4), 3592–3598 (2011).
  94. X. Chen and H. K. Tsang, "Polarization-independent grating couplers for silicon-on-insulator nanophotonic waveguides," *Opt. Lett.* **36**(6), 796 (2011).
  95. H. Subbaraman, X. Xu, J. Covey, and R. T. Chen, "Efficient light coupling into in-plane semiconductor nanomembrane photonic devices utilizing a sub-wavelength grating coupler," *Opt. Express* **20**(18), 20659 (2012).
  96. Zhenzhou Cheng, Xia Chen, C. Y. Wong, Ke Xu, C. K. Y. Fung, Y. M. Chen, and Hon Ki Tsang, "Mid-Infrared Grating Couplers for Silicon-on-Sapphire Waveguides," *IEEE Photonics J.* **4**(1), 104–113 (2012).
  97. Z. Can, S. Jing-Hua, X. Xi, S. Wei-Min, Z. Xiao-Jun, C. Tao, Y. Jin-Zhong, and Y. Yu-De, "High Efficiency Grating Coupler for Coupling between Single-Mode Fiber and SOI Waveguides," *Chinese Phys. Lett.* **30**(1), 014207 (2013).
  98. Q. Zhong, V. Veerasubramanian, Y. Wang, W. Shi, D. Patel, S. Ghosh, A. Samani, L. Chrostowski, R. Bojko, and D. V. Plant, "Focusing-curved subwavelength grating couplers for ultra-broadband silicon photonics optical interfaces," *Opt. Express* **22**(15), 18224 (2014).
  99. D. Benedikovic, C. Alonso-Ramos, P. Cheben, J. H. Schmid, S. Wang, D.-X. Xu, J. Lapointe, S. Janz, R. Halir, A. Ortega-Moñux, J. G. Wang iemert-P érez, I. Molina-Fernández, J.-M. F éldi, L. Vivien, and M. Dado, "High-directionality fiber-chip grating coupler with interleaved trenches and subwavelength index-matching structure," **40**(18), 4190–4193 (2015).
  100. D. Benedikovic, P. Cheben, J. H. Schmid, B. Lamontagne, S. Wang, J. Lapointe, S. Janz, M. Dado, and A. Ortega-mo, "Subwavelength index engineered surface grating coupler with sub-decibel efficiency for 220-nm silicon-on-insulator waveguides," *Opt. Express* **23**(17), 22628–22635 (2015).
  101. C. Alonso-Ramos, M. Nedeljkovic, D. Benedikovic, J. S. Penadés, C. G. Littlejohns, A. Z. Khokhar, D. Pérez-Galacho, L. Vivien, P. Cheben, and G. Z. Mashanovich, "Germanium-on-silicon mid-infrared grating couplers with low-reflectivity inverse taper excitation," *Opt. Lett.* **41**(18), 4324 (2016).
  102. J. Favreau, C. Durantin, J.-M. F éldi, S. Boutami, and G.-H. Duan, "Suspended mid-infrared fiber-to-chip grating couplers for SiGe waveguides," in H. Schröder and R.

- T. Chen, eds. (International Society for Optics and Photonics, 2016), **9753**, p. 975319.
103. Z. Zhang, B. Huang, Z. Zhang, C. Cheng, H. Liu, H. Li, and H. Chen, "Highly efficient vertical fiber interfacing grating coupler with bilayer anti-reflection cladding and backside metal mirror," *Opt. Laser Technol.* **90**, 136–143 (2017).
  104. Q. Liu, J. M. Ramírez, V. Vakarín, D. Benedikovic, C. Alonso-Ramos, J. Frigerio, A. Ballabio, G. Isella, L. Vivien, and D. Marris-Morini, "7.5  $\mu\text{m}$  wavelength fiber-chip grating couplers for Ge-rich SiGe photonics integrated circuits," in *Silicon Photonics: From Fundamental Research to Manufacturing*, R. G. Baets, P. O'Brien, and L. Vivien, eds. (SPIE, 2018), p. 23.
  105. W. H. Bragg and W. L. Bragg, "The Reflection of X-rays by Crystals," *Proc. R. Soc. A Math. Phys. Eng. Sci.* **88**(605), 428–438 (1913).
  106. S. E. Miller, "Integrated Optics: An Introduction," *Bell Syst. Tech. J.* **48**(7), 2059–2069 (1969).
  107. K. O. Hill, Y. Fujii, D. C. Johnson, and B. S. Kawasaki, "Photosensitivity in optical fiber waveguides: Application to reflection filter fabrication," *Appl. Phys. Lett.* **32**(10), 647–649 (1978).
  108. D. T. H. Tan, K. Ikeda, and Y. Fainman, "Cladding-modulated Bragg gratings in silicon waveguides," *Opt. Lett.* **34**(9), 1357 (2009).
  109. G. Jiang, R. Chen, Q. Zhou, J. Yang, M. Wang, and X. Jiang, "Slab-Modulated Sidewall Bragg Gratings in Silicon-on-Insulator Ridge Waveguides," *IEEE Photonics Technol. Lett.* (2010).
  110. X. Wang, S. Grist, J. Flueckiger, N. A. F. Jaeger, and L. Chrostowski, "Silicon photonic slot waveguide Bragg gratings and resonators," *Opt. Express* **21**(16), 19029 (2013).
  111. N. N. Klimov, S. Mittal, M. Berger, and Z. Ahmed, "On-chip silicon waveguide Bragg grating photonic temperature sensor," *Opt. Lett.* **40**(17), 3934 (2015).
  112. K. Bédard, A. D. Simard, B. Filion, Y. Painchaud, L. A. Rusch, and S. LaRochelle, "Dual phase-shift Bragg grating silicon photonic modulator operating up to 60 Gb/s," *Opt. Express* **24**(3), 2413 (2016).
  113. C. Klitis, G. Cantarella, M. J. Strain, and M. Sorel, "High-extinction-ratio TE/TM selective Bragg grating filters on silicon-on-insulator," *Opt. Lett.* **42**(15), 3040 (2017).
  114. D. Pérez-Galacho, C. Alonso-Ramos, F. Mazeas, X. Le Roux, D. Oser, W. Zhang, D. Marris-Morini, L. Labonté S. Tanzilli, É. Cassan, and L. Vivien, "Optical pump-rejection filter based on silicon sub-wavelength engineered photonic structures," *Opt. Lett.* **42**(8), 1468 (2017).
  115. D. Oser, D. Pérez-Galacho, C. Alonso-Ramos, X. Le Roux, S. Tanzilli, L. Vivien, L. Labonté and É. Cassan, "Subwavelength engineering and asymmetry: two efficient tools for sub-nanometer-bandwidth silicon Bragg filters," *Opt. Lett.* **43**(14), 3208 (2018).
  116. Q. Liu, J. M. Ramirez, V. Vakarín, X. Le Roux, J. Frigerio, A. Ballabio, E. T. Simola, C. Alonso-Ramos, D. Benedikovic, D. Bouville, L. Vivien, G. Isella, and D. Marris-Morini, "On-chip Bragg grating waveguides and Fabry-Perot resonators for long-wave infrared operation up to 84  $\mu\text{m}$ ," *Opt. Express* **26**(26), 34366 (2018).
  117. D. T. H. Tan, K. Ikeda, S. Zamek, A. Mizrahi, M. P. Nezhad, A. V. Krishnamoorthy, K. Raj, J. E. Cunningham, X. Zheng, I. Shubin, Y. Luo, and Y. Fainman, "Wide bandwidth, low loss 1 by 4 wavelength division multiplexer on silicon for optical

- interconnects," *Opt. Express* **19**(3), 2401 (2011).
118. D. Oser, F. Mazeas, X. Le Roux, D. Perez-Galacho, O. Alibart, S. Tanzilli, L. Labonte, D. Marris-Morini, L. Vivien, E. Cassan, and C. Alonso-Ramos, "Coherency-broken Bragg filters: surpassing on-chip rejection limitations," (2018).
  119. X. Nie, N. Turk, Y. Li, Z. Liu, and R. Baets, "High extinction ratio on-chip pump-rejection filter based on cascaded grating-assisted contra-directional couplers in silicon nitride rib waveguides," *Opt. Lett.* **44**(9), 2310 (2019).
  120. H. Kogelnik and C. V. Shank, "Coupled-Wave Theory of Distributed Feedback Lasers," *J. Appl. Phys.* **43**(5), 2327–2335 (1972).
  121. W.-P. Huang, "Coupled-mode theory for optical waveguides: an overview," *J. Opt. Soc. Am. A* **11**(3), 963 (1994).
  122. T. E. Murphy, "Design, fabrication and measurement of integrated Bragg grating optical filters," (2001).
  123. E. H. Bernhardt, *Bragg-Grating-Based Rare-Earth-Ion-Doped Channel Waveguide Lasers and Their Applications* (2012).
  124. B. Pressl, T. Günthner, K. Laiho, J. Geßler, M. Kamp, S. Höfling, C. Schneider, and G. Weihs, "Mode-resolved Fabry-Perot experiment in low-loss Bragg-reflection waveguides," *Opt. Express* **23**(26), 33608 (2015).
  125. D. K. Armani, T. J. Kippenberg, S. M. Spillane, and K. J. Vahala, "Ultra-high-Q toroid microcavity on a chip," *Nature* **421**(6926), 925–928 (2003).
  126. B. B. C. Kyotoku, L. Chen, and M. Lipson, "Sub-nm resolution cavity enhanced microspectrometer," *Opt. Express* **18**(1), 102 (2010).
  127. F. Y. Gardes, A. Brimont, P. Sanchis, G. Rasigade, D. Marris-Morini, L. O'Faolain, F. Dong, J. M. Fedeli, P. Dumon, L. Vivien, T. F. Krauss, G. T. Reed, and J. Mart í "High-speed modulation of a compact silicon ring resonator based on a reverse-biased pn diode," *Opt. Express* **17**(24), 21986 (2009).
  128. B. Yao, S.-W. Huang, Y. Liu, A. K. Vinod, C. Choi, M. Hoff, Y. Li, M. Yu, Z. Feng, D.-L. Kwong, Y. Huang, Y. Rao, X. Duan, and C. W. Wong, "Gate-tunable frequency combs in graphene–nitride microresonators," *Nature* **558**(7710), 410–414 (2018).
  129. A. Spott, Y. Liu, T. Baehr-Jones, R. Ilic, and M. Hochberg, "Silicon waveguides and ring resonators at 5.5  $\mu\text{m}$ ," *Appl. Phys. Lett.* **97**(21), 213501 (2010).
  130. Y. Chen, H. Lin, J. Hu, and M. Li, "Heterogeneously Integrated Silicon Photonics for the Mid-Infrared and Spectroscopic Sensing," *ACS Nano* **8**(7), 6955–6961 (2014).
  131. J. M. Ramirez, Q. Liu, V. Vakarin, X. Le Roux, J. Frigerio, A. Ballabio, C. Alonso-Ramos, E. T. Simola, L. Vivien, G. Isella, and D. Marris-Morini, "Broadband integrated racetrack ring resonators for long-wave infrared photonics," *Opt. Lett.* **44**(2), 407–410 (2019).
  132. L. Vivien and L. Pavesi, *Handbook of Silicon Photonics* (Taylor & Francis, 2013).
  133. A. Yariv, "Universal relations for coupling of optical power between microresonators and dielectric waveguides," **29**, 451460 (1997).
  134. A. Vasiliev, M. Muneeb, J. Allaert, J. Van Campenhout, R. Baets, and G. Roelkens, "Integrated Silicon-on-Insulator Spectrometer with Single Pixel Readout for Mid-Infrared Spectroscopy," *IEEE J. Sel. Top. Quantum Electron.* **24**(6), (2018).
  135. K. Shang, S. Pathak, C. Qin, and S. J. Ben Yoo, "Low-Loss Compact Silicon Nitride Arrayed Waveguide Gratings for Photonic Integrated Circuits," *IEEE Photonics J.* **9**(5), 1–5 (2017).

136. P. Cheben, J. H. Schmid, A. Del âge, A. Densmore, S. Janz, B. Lamontagne, J. Lapointe, E. Post, P. Waldron, and D.-X. Xu, "A high-resolution silicon-on-insulator arrayed waveguide grating microspectrometer with sub-micrometer aperture waveguides.," *Opt. Express* **15**(5), 2299–306 (2007).
137. X. Ma, M. Li, and J. J. He, "CMOS-compatible integrated spectrometer based on echelle diffraction grating and MSM photodetector array," *IEEE Photonics J.* **5**(2), (2013).
138. D. Melati, P. G. Verly, A. Del âge, P. Cheben, J. H. Schmid, S. Janz, and D.-X. Xu, "Athermal echelle grating filter in silicon-on-insulator using a temperature-synchronized input," *Opt. Express* **26**(22), 28651 (2018).
139. A. V. Velasco, P. Cheben, P. J. Bock, A. Del âge, J. H. Schmid, J. Lapointe, S. Janz, M. L. Calvo, D.-X. Xu, M. Florjańczyk, and M. Vachon, "High-resolution Fourier-transform spectrometer chip with microphotonic silicon spiral waveguides," *Opt. Lett.* **38**(5), 706 (2013).
140. E. Ryckeboer, G. Roelkens, R. Baets, and X. Nie, "CMOS-compatible broadband co-propagative stationary Fourier transform spectrometer integrated on a silicon nitride photonics platform," *Opt. Express*, Vol. 25, Issue 8, pp. A409-A418 **25**(8), A409–A418 (2017).
141. W. Herschel, "Experiments on the Refrangibility of the Invisible Rays of the Sun.," *Proc. R. Soc. London* **1**(0), 22–23 (1800).
142. P. Jacquinot, "Caractères communs aux nouvelles méthodes de spectroscopie interférentielle ; Facteur de mérite," *J. Phys. le Radium* **19**(3), 223–229 (1958).
143. P. R. Griffiths and J. A. de Haseth, *Fourier Transform Infrared Spectrometry* (John Wiley & Sons, Inc., 2007).
144. S. Rehman, Z. Movasaghi, J. A. Darr, and I. U. Rehman, "Fourier transform infrared spectroscopic analysis of breast cancer tissues; Identifying differences between normal breast, invasive ductal carcinoma, and ductal carcinoma in situ of the breast," *Appl. Spectrosc. Rev.* **45**(5), 355–368 (2010).
145. J. Depciuch, E. Kaznowska, I. Zawlik, R. Wojnarowska, M. Cholewa, P. Heraud, and J. Cebulski, "Application of Raman Spectroscopy and Infrared Spectroscopy in the Identification of Breast Cancer," *Appl. Spectrosc.* **70**(2), 251–263 (2016).
146. J. Harlander, R. J. Reynolds, and F. L. Roesler, "Spatial heterodyne spectroscopy for the exploration of diffuse interstellar emission lines at far-ultraviolet wavelengths," *Astrophys. J.* **396**, 730 (1992).
147. "Spatial Heterodyne Spectrometer (SHS) Interferometer [image] | EurekaAlert! Science News," <https://www.eurekaalert.org/multimedia/pub/15512.php>.
148. D. M. Kita, B. Miranda, D. Favela, D. Bono, J. Michon, H. Lin, T. Gu, and J. Hu, "High-performance and scalable on-chip digital Fourier transform spectroscopy," *Nat. Commun.* **9**(1), 1–7 (2018).
149. M. C. M. M. Souza, A. Grieco, N. C. Frateschi, and Y. Fainman, "Fourier transform spectrometer on silicon with thermo-optic non-linearity and dispersion correction," *Nat. Commun.* **9**(1), 1–8 (2018).
150. D. F. V. James, "Change of polarization of light beams on propagation in free space," *J. Opt. Soc. Am. A* **11**(5), 1641–1643 (1994).
151. V. Vakarin, J. M. Ram érez, J. Frigerio, A. Ballabio, X. Le Roux, Q. Liu, D. Bouville, L. Vivien, G. Isella, and D. Marris-Morini, "Ultra-wideband Ge-rich silicon

- germanium integrated Mach–Zehnder interferometer for mid-infrared spectroscopy," *Opt. Lett.* **42**(17), 3482 (2017).
152. M. Florjanczyk, P. Cheben, S. Janz, A. Scott, B. Solheim, and D.-X. Xu, "Multiaperture planar waveguide spectrometer formed by arrayed Mach-Zehnder interferometers," *Opt. Express* **15**(26), 18176 (2007).
  153. Q. Liu, J. M. Ramirez, V. Vakarin, X. Le Roux, C. Alonso-Ramos, J. Frigerio, A. Ballabio, E. Talamas Simola, D. Bouville, L. Vivien, G. Isella, and D. Marris-Morini, "Integrated broadband dual-polarization Ge-rich SiGe mid-infrared Fourier-transform spectrometer," *Opt. Lett.* **43**(20), 5021 (2018).
  154. H. H. Li, "Refractive index of silicon and germanium and its wavelength and temperature derivatives," *J. Phys. Chem. Ref. Data* **9**(3), 561–658 (1980).
  155. H. Podmore, A. Scott, P. Cheben, A. V. Velasco, J. H. Schmid, M. Vachon, and R. Lee, "Demonstration of a compressive-sensing Fourier-transform on-chip spectrometer," *Opt. Lett.* **42**(7), 1440–1443 (2017).
  156. M. Montesinos-ballester, Q. Liu, V. Vakarin, J. M. Ramirez, C. Alonso-ramos, X. Le Roux, J. Frigerio, A. Ballabio, E. Talamas, L. Vivien, G. Isella, and D. Marris-Morini, "On-chip Fourier-transform spectrometer based on spatial heterodyning tuned by thermo-optic effect," *Sci. Rep.* (2019).
  157. J. M. Ramirez, V. Vakarin, J. Frigerio, P. Chaisakul, D. Chrastina, X. Le Roux, A. Ballabio, L. Vivien, G. Isella, and D. Marris-Morini, "Ge-rich graded-index Si<sub>1-x</sub>Ge<sub>x</sub> waveguides with broadband tight mode confinement and flat anomalous dispersion for nonlinear mid-infrared photonics," *Opt. Express* **25**(6), 6561 (2017).

**Titre :** Circuits photoniques intégrés SiGe pour des applications capteurs dans le moyen-infrarouge

**Mots clés :** Photonique silicium, Moyen-infrarouge, SiGe, Capteurs optiques intégrés

**Résumé :** La spectroscopie dans le moyen-infrarouge est une méthode universelle pour identifier les substances chimiques et biologiques, car la plupart des molécules ont leurs résonances de vibration et de rotation dans cette plage de longueurs d'onde. Les systèmes moyen infrarouge disponibles dans le commerce reposent sur des équipements volumineux et coûteux, tandis que de nombreux efforts sont maintenant consacrés à la réduction de leur taille et leur intégration sur circuits intégrés. L'utilisation de la technologie silicium pour la réalisation de circuits photoniques dans le moyen-infrarouge présente de nombreux avantages: fabrication fiable, à grand volume, et réalisation de circuits photoniques à hautes performances, compacts, légers et à faible consommation énergétique. Ces avantages sont particulièrement intéressants pour les systèmes de détection spectroscopique moyen infrarouge, qui besoin d'être portable et à faible coût. Parmi les différents matériaux disponibles en photonique silicium, les alliages silicium-germanium (SiGe) à forte concentration en Ge sont particulièrement intéressants en raison de la grande fenêtre de transparence du Ge, pouvant atteindre 15  $\mu\text{m}$ .

Dans ce contexte, l'objectif de cette thèse est d'étudier une nouvelle plate-forme SiGe à forte concentration en Ge, pour la démonstration de circuits photoniques moyen infra rouge. Cette nouvelle plate-forme devrait bénéficier d'une large gamme de transparence en longueurs d'onde de transparence et de la possibilité d'ajuster les propriétés des guides optiques (indice effectif, dispersion,...).

Au cours de cette thèse, différentes plates-formes basées sur différents profils graduels du guide d'onde ont été étudiées. Tout d'abord, il a été démontré qu'il était possible d'obtenir des guides présentant de faibles pertes optiques inférieures à 3 dB/cm dans une large plage de longueurs d'onde, de 5,5 à 8,5  $\mu\text{m}$ . Une preuve de concept de détection de molécules, basée sur l'absorption de la partie évanescent du mode optique a ensuite été démontrée. Ensuite, les composants formant les briques de base classiques de la photonique intégrée ont été étudiés. Les premières cavités intégrées ont été réalisées à 8  $\mu\text{m}$ . Deux configurations ont été étudiées : des cavités Fabry-Perot utilisant des miroirs de Bragg intégrés dans les guides d'onde et des résonateurs en anneau. Un spectromètre à transformée de Fourier fonctionnant sur une large bande spectrale, et pour les deux polarisations de la lumière a également été démontré. Tous ces résultats reposent sur la conception des matériaux et des composants, la fabrication en salle blanche et la caractérisation expérimentale. Ce travail a été effectué dans le cadre du projet européen INSPIRE en collaboration avec le Pr. Giovanni Isella de Politecnico Di Milano.



**Title :** SiGe photonic integrated circuits for mid-infrared sensing applications

**Keywords:** Silicon Photonics, Mid-infrared, SiGe, integrated optical sensors

**Abstract:** Mid-infrared (mid-IR) spectroscopy is a nearly universal way to identify chemical and biological substances, as most of the molecules have their vibrational and rotational resonances in the mid-IR wavelength range. Commercially available mid-IR systems are based on bulky and expensive equipment, while lots of efforts are now devoted to the reduction of their size down to chip-scale dimensions. The use of silicon photonics for the demonstration of mid-IR photonic circuits will benefit from reliable and high-volume fabrication to offer high performance, low cost, compact, lightweight and power consumption photonic circuits, which is particularly interesting for mid-IR spectroscopic sensing systems that need to be portable and low cost. Among the different materials available in silicon photonics, Germanium (Ge) and Silicon-Germanium (SiGe) alloys with a high Ge concentration are particularly interesting because of the wide transparency window of Ge up to 15  $\mu\text{m}$ .

In this context, the objective of this thesis is to investigate a new Ge-rich graded SiGe platform for mid-IR photonic circuits. Such new platform was expected to benefit from a wide transparency wavelength range and a high versatility in terms of optical engineering (effective index, dispersion, ...).

During this thesis, different waveguides platforms based on different graded profiles have been investigated. First it has been shown that waveguides with low optical losses of less than 3 dB/cm can be obtained in a wide wavelength range, from 5.5 to 8.5  $\mu\text{m}$ . A proof of concept of sensing based on the absorption of the evanescent component of the optical mode has then been demonstrated. Finally, elementary building blocs have been investigated. The first Bragg mirror-based Fabry Perot cavities and racetrack resonators have been demonstrated around 8  $\mu\text{m}$  wavelength. A broadband dual-polarization MIR integrated spatial heterodyne Fourier-Transform spectrometer has also been obtained. All these results rely on material and device design, clean-room fabrication and experimental characterization. This work was done in the Framework of EU project INsPIRE in collaboration with Pr. Giovanni Isella from Politecnico Di Milano.